MOLECULAR DYNAMIC SIMULATIONS OF THE INTERGRANULAR FILMS BETWEEN ALUMINA AND SILICON NITRIDE CRYSTAL GRAINS

By SHENGHONG ZHANG

A Dissertation submitted to the
Graduate School-New Brunswick
Rutgers, The State University of New Jersey
in partial fulfillment of the requirements
for the degree of
Doctor of Philosophy
Graduate Program in Materials Science and Engineering
written under the direction of
Professor Stephen H. Garofalini
and approved by

____

____

____

____

New Brunswick, New Jersey
October, 2007

ABSTRACT OF THE DISSERTATION

MOLECULAR DYNAMIC SIMULATIONS OF THE INTERGRANULAR FILMS BETWEEN ALUMINA AND SILICON NITRIDE CRYSTAL GRAINS

By SHENGHONG ZHANG

Dissertation Director:
Professor STEPHEN H. GAROFALINI

The intergranular films (IGFs) between the ceramics grains have very important effects on the structure and mechanical properties on the whole ceramics and have been studied for many decades. In the thesis, molecular dynamic (MD) computer simulations were applied to study the IGFs between the alumina and silicon nitride ceramic grains.

Preferential adsorption of specific ions from the IGFs to the contacting surfaces of the alumina crystals was observed in the study of calcium-alumino-silicate glassy (CAS) IGFs formed between the combined basal and prism orientations of α-Al_2O_3 crystals. This segregation of specific ions to the interface enables formation of localized, ordered structures between the IGF and the crystals. However, the segregation behavior of the ions is anisotropic, depending on the orientation of the α-Al_2O_3 crystals.

Self-diffusion of calcium ions between these CAS IGFs was also carried out by MD simulations. The results show that the diffusion coefficients adjacent to the interfaces are smaller and the activation energies are much higher than those in the interior of the IGF and in bulk glasses. It was also suggested that Ca transport is mainly though the

interior of the IGF and implies that diffusion would be significantly inhibited by sufficiently thin IGFs.

The growth of the alumina ceramic grains was simulated in the contacting with IGFs containing high concentrations of aluminum ions. Five different compositions in the IGFs were studied. Results show preferential growth along the $[11\bar{2}0]$ of the $(11\bar{2}0)$ surface in comparison to growth along the [0001] direction on the (0001) surface for compositions near a Ca/Al ratio of 0.5. The simulations also show the mechanism by which Ca ions in the IGF inhibit growth on the basal surface. The simulations provide an atomistic view of attachment onto crystal surfaces, affecting grain growth in alumina.

The dissolution of the alumina crystal grains in the silicate melts is another important issue in the application of alumina ceramics. The simulations results showed that alumina grains dissolved into the melts homogeneously at very high temperatures. The orientation of the crystals and the compositions of the melts only take effect at some intermediate temperatures, to make the alumina grains dissolution anisotropic.

The fracture phenomena of the pure silica IGFs between the basal silicon nitride crystals were studied by applying the constant tensile strain on the simulated IGF system, as well as for the bulk silica glass for the comparison. The data indicated that the fracture was happened in the interior of the IGFs and the thickness of the IGFs has important effect on the fracture stress/strain relationships.

Acknowledgements

Many kind people have helped me during my Ph.D study and research. I am so pleased that I have this opportunity to express my gratitude to all of them.

I would especially like to thank Professor Stephen H. Garofalini, my thesis advisor, for his inspiration, insight, expertise advice, patience and support during my graduate years at Rutgers University. I learned a lot and was greatly benefited from his thorough understanding of the materials and abundant experience in the computer simulations.

I would like to thank the director of graduate students, Prof. Lisa Klein, also one of my thesis committee members, for her kind help in many aspects in my years in the department of Materials Science and Engineering. I thank Prof. George H. Sigel and Prof. Haym Benaroya for joining the committee to help me with the thesis and take effort in reading the whole thesis thoroughly.

I am also grateful to Professor Roger Cannon for his help at my beginning at Rutgers University, as well as in my coursework studies.

I owe many thanks to Ms Claudia Kuchinow, the administrative assistant in this department, for her continuous and generous help in preparing all the documents from my first day at Rutgers University.

I must express my gratitude to Dr. Weiqun Li and Dr. Ying Ma for the cooperation and discussions during my thesis research and the entertainment time we had together. I also thank another team worker in the lab, Mr. Thiruvilla Mahadevan. I would like to thank all my friends for all the happy time we had together.

Finally, I would like to thank my parents, sisters, their spouses for their love, warm support through the years. They should share every success I made in my life and I owe my deepest thanks to them. I am grateful to my loving girlfriend, Dr. Yingjie Li, for her kindness and great help in my life and my study, for the sharing of all my frustrations and successes.

Table of Contents

Abstract of the Dissertation………………………………………………………………ii

Acknowledgments…………………………………………………………………..iv

Table of Contents…………………………………..……………………..…………vi

List of Tables………………………………………………………………..…ix

List of Figures…………………………………………………………………………x

I Background………………………………………………………………………1

I.1. Computer Simulations …………………..………………………………1

I.2. The Molecular Dynamic (MD) Simulation Technique…..…………...……...2

I.3. The Intergranular Films Between Crystal Grain in Ceramics……...……10

I.4. The Computer Simulations in the Study of IGFs…………………..………16

II Computational Procedure ……………………………………………….……18

III Molecular Dynamics Computer Simulations of the Interface Structure of Calcium-Alumino-Silicate Intergranular Films between Combined Basal and Prism Planes of α-Al_2O_3……………………………………………………...21

III.1. Introduction…………………………...………………………………21

III.2. Computational Procedure ……………………...………………………24

III.3. Results and Discussion …………………………...…………………..28

III.3.2. Atom Number Density Analysis………………...………………30

III.3.3 Coordination Number Analysis…………………………………..36

III.4. Conclusions…………………………………………………...…………45

IV Molecular Dynamics Simulation of Calcium Diffusion in the Calcium Alumino-Silicate Intergranular Films Between Different Alumina Grains ….47

IV.1. Introduction……………………….……………………….………………47

IV.2. Computational Procedure …………….………………..………...............49

IV.3. Results and Discussion……………………..……..……………………..52

IV.3.1. Bulk Glass Diffusion ………………………………..…………..52

IV.3.2. Ca Diffusion at the Interfaces and in the Interior of the IGF Glasses …………………………………………………………………54

IV.3.2.1. Ca Diffusion With Frozen Crystals………………..…..54

IV.3.2.2. Ca Diffusion near the Basal and Prism Interfaces With Free Crystal Surfaces…………………………..……………58

IV.3.3. Discussion …………………………………….…………………60

IV.4 Conclusions………………………………………………………..……..65

V Molecular Dynamics Simulations of the Effect of the Composition of Calcium Alumino-Silicate Intergranular Films on Alumina Grain Growth ………………67

V.1. Introduction……………………………………………….…………...67

V.2. Computer Procedure.. …………………………………..………………..71

V.3. Results and Discussion………………………….……………………..73

V.3.1. Snapshots ……….……………………………..………………73

V.3.2. Density Profile Analysis ……………………….……………...75

V.3.3 Coordination Number Analysis…………………..……………..79

V.3.4. The Relationship Between the Crystal Growth and the Al Content in IGF…………………………………………………………………81

V.4. Conclusions…………………………………..………..………………..84

VI Molecular Dynamic Simulations of Dissolutions of (0001) Basal and $(11\bar{2}0)$ Prism Oriented α-Alumina Grains in Different Silicates ……………………………86

VI.1. Introduction……………………………………………………………...86

VI.2. Computer Procedure..………………………………….……………..88

VI.3. Results and Discussion…………………………………………………..89

VI.3.1. The Dissolution Temperature …….……………………………92

VI.3.2. The Dissolution in Al_2O_3.SiO_2 Melt……………………………...93

VI.3.3 The Dissolution in CaO.SiO_2 Melt ……………...………………..97

VI.4. Conclusions…………………………………………………..………99

VII Molecular Dynamic Simulations of the Fracture in the of SiO_2 IGF Between Basal Planes of Silicon Nitride Grains …………………………………..…………101

VII.1. Introduction…………………………………………………………...101

VII.2. Computer Procedure …………………………….………………..104

VII.3. Results and Discussion……………………………………….………..105

VII.3.1. The Structures of the IGF ……….……………….…………105

VII.3.2. The Stress/Strain Relationship in the IGFs and Bulk Glass…...106

VII.3.3 . The Voids and Cracks in the IGFs……………………………..108

VII.3.4. The SiO_4-tetrahedra Rings in the IGF and Bulk Glass………..109

VII.4. Conclusions……………………………………………………...…117

VIII Summary of Conclusions………………………… ………………………..118

References……………………………………………………………………………120

Vita…………………………………………………………………………………...130

Lists of Tables

II-.1 Parameters for Modified BMH Pair Potential …………………..…………....20

II-2 Assignment summary of peptide GAAGVM and GAAVM……………………..20

III-1 The Compositions of 4 different IGFs …………………………………………..25

IV-1 Calcium self-diffusion coefficients …………..…………..……………………..53

V-1 Composition and system sizes …………………………...…………………...72

V-2 Melt /quench process for making glassy IGF between crystals …….………….72

List of Figures

Fig. I-1 The schematic of a typical MD simulation……………………………………9

Fig. III-1 A simple illustration of the structure of simulation system…………………26

Fig. III-2 Snapshot of the side view of the local configuration of ions at the (0001)/IGF interface of 112 system. Dashed line separates atoms originally in the IGF from those in the crystal……………………………………………………………29

Fig. III-3 Snapshot of a side view of local configuration of the $(11\bar{2}0)$/IGF interface of 112 system. Dashed line separates atoms originally in the IGF from those in the crystal……………………………………………………………………30

Fig. III-4 Density profile of all atoms in the 112 CAS system. Basal oriented crystal on left, prism oriented crystal on right. Heavier lines indicate individual species from the IGF. 'Cation from IGF' is sum of all cations in the IGF…………………31

Fig.III-5 Higher resolution graphs of the density profiles of the specific interfaces and compositions. (a-d) Basal oriented crystal is on the left of images, compositions 112, 313, 216, and 14535, respectively. Arrows in 5a indicate first Al peak, overlapping O and Ca first peaks, and first Si and second Al peaks. (e-h) Prism oriented crystal is at the right of images, compositions 112, 313, 216, and 14535, respectively. Arrows in 5e indicate first O and Al peaks from the IGF adsorbed onto prism surface……………………………………………………………33

Fig.III-6 The relationship between the area of the first peak of Al from the IGF adsorbed onto the crystal and the Al concentration in the corresponding bulk glass that forms the IGF for the four systems. Both the basal and the prism sides are shown here…………..…………………………………………..………………36

Fig. III-7 Coordination number (CN) profile of Al atoms along z direction (showing only the IGF and near interface region). (a) 112, (b) 313, (c) 216, (d) 14535 compositions……………………………………………………………..38

Fig. III-8 Coordination number (CN) profile of O atoms along z direction (showing only the IGF and the near interface region). (a) 112, (b) 313, (c) 216, (d) 14525 compositions……………………..……………………………………42

Fig. III-9 Area of the first peak of 3 coordinated O adsorbed onto prism and basal planes as a function of the Al/Ca ratio in the IGF………………….……………..43

Fig. IV-1 Mean square displacement (MSD) of Ca in bulk calcium alumino-silicate 112 glass…………………………………..……………………………………52

Fig. IV-2 Ca diffusion for the 313 intergranular film (IGF) system at different temperatures: (a) Ca at the basal interface, (b) Ca in the interior of the IGF, (c) Ca near the prism interface…………………………………………………….55

Fig. IV-3 The number of Ca ions in the volume near the 112 basal interface as a function of time from each initial t_0……………………………………………………56

Fig. IV-4 The mean square displacement (MSD)versus time in the 313 intergranular film system for Ca ions in the volume adjacent to the basal interface………………58

Fig. IV-5 Ca MSD at the basal side(a, b) and prism side (c, d) with free crystal surface for the 313 (a, c) and 14535 (b, d) systems. Note the difference in the y-axis units in (a) in comparison to others……………………………..……………………60

Fig. IV-6 Radial distribution functions (RDFs) of the interior of the intergranular film (IGF) (exclude the interfaces) and the bulk glass for the (a) 112 and (b) 313 compositions. (a) shows the smallest structure differences and (b) shows the largest difference of the four compositions studied……………………………62

Fig. IV-7 Density profile of individual species at the interfaces of 313 system showing ordering near the interfaces caused by the presence of the crystals. Crystal on the left in the BASAL image and on the right PRISM image. Labels given in the inset on BASAL image…………………………………..……………………62

Fig. IV-8 Density profile of individual species at the interfaces of the 112 system showing no change in the first Al peak adsorbed onto the basal side in comparison to the 313 system in Fig. IV-7, but a significant increase in that on the prism side. Labels given in inset on BASAL image………………………………………..64

Fig. V-1 Snapshots of thin cross-sections of atoms into the plane of the page near the Basal and Prism interfaces of 2 compositions in the simulations. Atoms from the crystal are below the dark solid horizontal line in each image; atoms originally from the IGF are above the dark horizontal line. Atoms between the dashed line and the solid line in 141 Prism image indicates the degree of ordering of the atoms from the IGF that adsorbed onto the crystal surface, forming an extension of the prism oriented crystal. Al=red, O=grey, Si=blue, Ca=yellow. Ca-O bonds are not drawn…………………………………………………………………….74

Fig. V-2 Density profiles of individual species at the Basal and Prism sides of the IGF for the 5 compositions as a function of distance perpendicular to the IGF-crystal interface. Thicker lines are for ions in the IGF. Line color associated with atom type is shown at the bottom of the figure……….……………………………76

Fig. V-3 Coordination of Al and O species in the IGF and crystal surfaces for 2 compositions. Note the different scale of the concentrations in the Al profile in the 141 system. Al and O are predominantly 4- and 2-coordinated, respectively, in the IGF, as expected for the glass, with increasing coordination at the interfaces, consistent with the higher coordination of each in the crystal……….…………78

Fig. V-4 Normalized area under the first adsorbed Al peak from the IGF onto the different crystal surfaces as a function of the ratio of Al/all cations for the compositions presented here and the 4 compositions previously studied (see ref 24). Note the significantly faster growth along the prism surface normal than the basal surface normal for most compositions, except at the lowest and highest Al ratio……………………………………………………………………….. 81

Fig. V-5 Average normalized area under the first adsorbed Al peak from the IGF onto the different crystal surfaces as a function of the Ca/Al ratio (R) for the compositions presented here and the 4 compositions previously studied (see ref 24). The equivalence point, R_e, is at 0.5. Below R_e, excess Al in the IGF allows for more rapid adsorption of Al onto the basal surface than that above the equivalence point…………………………………………………….………………83

Fig. VI-1 Basal Alumina crystal dissolution in CaO.SiO2 melt at 3500K (a) and 4000K (b)………………………………………………………………………………90

Fig. VI-2 The density profile of crystal Al atoms in both melts at the interface region for both the temperatures simulated: (a) basal alumina crystal, (b) prism alumina crystal……………………………..……………………………………..91

Fig. VI-3 The Al (both in the crystal and melt) density profile of the basal alumina crystal dissolution…………..……...…………………………………………94

Fig. VI-4 The Al (both in the crystal and melt) density profile of the prism alumina crystal dissolution……………………………………………………………95

Fig. VI-6 The density profile of Al from Al2O3.SiO2 melt in the basal alumina crystal dissolution…………………………………..…………………………96

Fig. VI-7 The density profile of Ca at the interface region of the basal alumina crystal dissolution in CaO.SiO2 melt………………………………………………97

Fig. VI-8 The density profile of Ca at the interface region of the prism alumina crystal dissolution in CaO.SiO2 melt………………….…………………………98

Fig VII-1 The snapshot of the 1 nm IGF between the basal Si3N4 grains…………..106

Fig VII-2 The stress-strain relationship of the simulated Si_3N_4 ceramic systems…..…107

Fig VII-3 The stress-strain relationship of the bulk SiO_2 glass……………………..…108

Fig. VII-4 The snapshots of the voids forming and development in the 1 nm IGF in silicon nitride system……………………………………………………….109

Fig. VII-5 The histogram of the ring distribution in the IGFs and bulk glass of the starting configuration before the stain……………………………………………110

Fig. VII-6. The rings distribution evolution of the 1 nm Si_3N_4 IGF system during the strain: (a) the rings ratio, which was calculated as the ratio of the certain kind of ring to all the rings (the stress curve was scaled to plot out in the figure); (b) relative ring ratio, the vertical axis is the ratio of the current ring percentage to the original ring percentage (of the starting configuration)....................................112

Fig. VII-7 The rings ratio evolution of the 1 nm Si_3N_4 IGF system (a) and bulk glass (b) under the stress (the corresponding stress curve was scaled to plot out in the figures respectively for each system)..115

I. Background

I.1 Computer Simulations

Computer simulations play a very important role in science and engineering today. In the past, physical sciences were characterized by interplay between experiment and theory. The experimental results, normally in numeric forms, were provided to testify the theory models. However, due to the invariable complexities in real world, a considerable amount of the simplifications has to be made to satisfy the model. In addition, the physical model could only be easily tested in some really simple cases. But many of the interested physical problems are beyond the simple cases that could be tested easily and directly by the experimental methods, especially when the research system becomes very small without losing the complexities, which makes the detection in the experiments a really challenge.

The computer simulation in the science and engineering started and developed with the application of the high speed computers from the 50s in last century. The physical theories and the practical engineering modes now can be proved and tested by the computer simulations without expensive and time-costing experiments. In addition, the simulation of the system can be more realistic without too many simplifications taken in the experiments, then the better understanding of the system can be provided. Even more, computer simulation can be taken for the systems studies that can not be done in the real experiments[1].

General mathematical computation and computation simulations in the studies of the system are different[2]. The computer simulations are actually virtual experiments or a series of experiments, not just the simple calculations. The model of the systems is built in the simulation based on the physical theory or the understanding in the real world. The physical constricts can be reflected and applied correctly in the model. The results of the simulation may not be unique and sometimes entirely unexpected.

I.2 The Molecular Dynamic Simulation Technique

Based on the theory and the application area, there are several computer simulation techniques at the atomic structure level, such as Quantum Mechanic simulation, Monte Carlo (MC) and molecular dynamic (MD) simulations. In the quantum mechanic simulations, the complete descriptions of the atomic orbitals for all electrons around the nuclei are presented in the simulation. The interactions of such orbitals in a single atom or between different atoms are calculated explicitly. The bonds for the atom pairs are described as the overlaps of the atomic orbitals. The simulation techniques can solve many problems in the quantum mechanics, such as the electronic energy levels of the atoms, the jumping activities and the bond details in the small cluster of atoms. But the computational complexity of such techniques limits the number of the atoms involved in the simulation and the time evolution for the system is not applicable.

Both molecular dynamic and Monte Carlo simulation are classic mechanic techniques and there are no description of the interactions between the nuclei and the electrons in the simulations. The smallest unit in the simulations is the whole atom or ion that is considered as a hard ball. Based on the chemical properties of the system studied, the hard ball can be positive or negative charged to represent the electron jumping from one species to another, though in some simulations the charges are allowed to change depending on the method applied. The interactions between the atoms (hard balls) that govern the movement of the atoms are described by effective potentials, the combination of repulsive and attractive effects. The nature of the interactions is the same as those in the quantum mechanic simulations. There are no certain formulations of the potentials. They are either obtained by semi-empirical methods or from the theoretical calculations. Generally the formulation of the potential is much simpler compared to the complex and explicit nuclei-electron and electron-electron interaction in the quantum mechanics, it makes the simulation of large and complex system possible and applicable. Not only the short term (the local structure) but also the long-term phenomena can be studied at the same time in MD and MC simulations.

The basic Monte Carlo method starts with the importance sampling[3]. The macro thermal dynamic properties are the average results of every possible micro-state of the system. And the importance sampling of the states can represent the properties of the system based on the statistical mechanics. For a given system with fixed temperature T and number of particles N, the equilibrium average of some quantity G can be expressed in terms of phase-space integrals involving the potential energy $U(r_1, r_2, ..., r_N)$,

$$\langle G \rangle = \frac{\int G(r_1, r_2, ..., r_N) e^{-\beta U(r_1, r_2, ..., r_N)} dr_1 dr_2 ... dr_N}{\int e^{-\beta U(r_1, r_2, ..., r_N)} dr_1 dr_2 ... dr_N} \tag{I.1}$$

Where $\{r_i | i = 1,2,...,N\}$ are the coordinates of the particles, $\beta = 1/k_B T$ and k_B is the Boltzmann constant. $\langle G \rangle$ corresponds to a series of measurement over an ensemble of independent systems. The MC method considers only configurational space without the momentum part of phase space in most cases, it can be only used to study systems in a equilibrium.

In a typical MC simulation, the atoms are subjected to random moves or other random actions in the simulation ‘Box’, the energies of the system before and after the actions are calculated based on the inter-atomic potential functions, though the actions may not be physically existed. Then the judgment to accept or reject such action is based on the energy difference caused by the action. If the action resulted in the total energy reduction, the action is accepted, otherwise its acceptance is based on a statistical mechanical probability. The equilibrium of the system will be reached after a long time simulation with very large number of such trials. Then the thermodynamic and other properties could be obtained by a series correct measurement of the system ensembles. Though more complicated refinements and extensions were developed to make the MC applicable for the different simulation systems, the basic ideas remain the same. There are some good instructions and more studies about MC by Dann Frenkel[1].

MD is a computer simulating technique that allows one to predict the time evolution of the system interacting particles[3]. All the atoms in the simulation ‘Box’ are subjected to move according to classic equations of motion, the Newton’s second Law. It provides the time evolution of the system as well as the atoms themselves which can not be seen in the MC simulations. It was first introduced in the study of the interactions between hard spheres by Alder and Wainwright[4, 5]. Rahmna began to use the continue potentials in the MD simulation of liquid argon[6] and later other liquid, such as water[7]. After that, a lot of studies both in the interactions potentials and in the simulation methodologies make a large development in MD simulations[8-11]. Now MD simulation plays an important role in the theoretical studies of chemistry, biology and materials science.

MD simulation generates a series of time evolution configurations following the dynamic motions Law. Also this time dependent configurations created a trajectory of the atoms/ensemble from the starting point to the simulation end [2]. The macro thermodynamic properties can also be obtained by the converting the detailed information of the micro level ensembles based on statistical mechanics. But the calculation of the time averages by MD is not the same approach in conventional statistical mechanics like it in the MC simulations. For example, making a reasonable assumption that the final configuration of the system reaches the equilibrium, it is apparently that the probability density of such configuration is higher that others which are not at the equilibrium state. However, the ensemble average can be transferred into the time average, i.e., the trajectory average. Then we can calculate the macro thermodynamic properties of the simulated system from trajectory average in MD simulations.

Though the number of atoms used in the MC and MD simulation is much greater than it in the quantum mechanics simulations, the size of the simulation system in MC and MD is a finite value. The finite and infinite systems are very different because the boundaries of the finite system play an important role in the properties. The larger the size of the system is, the more likely it behavior like an infinite system [2]. However, the question arises that how larger a relatively small system should be to yield the results that resemble the behavior of the infinite system faithfully. Apparently the answer is not unique, it is dependent on what kind of the system is and in what conditions the system is being studied. In the case of MD and MC simulations, all the atoms are restricted in a limited size box, despite whatever the shape of the box is. The container's walls play as the boundaries of the simulation system, mostly they are rigid and collide with the atoms which are trying to escape from the box if no further steps are taken to eliminate such boundary conditions. These atoms take a relatively larger fraction in the MD and MC simulation compared to the real macro structures. The periodic boundary condtions (PBC) are introduced in the classic mechanic simulations in the effort to eliminate the undesirable boundary effects [1] [3]. The effect of the PBC is equivalent to build an infinite, space-filling array of identical copies of the simulation box. During the simulations, once the atoms near the boundaries leave the box through a particular boundary face, they immediately move back into the box through the opposite side. Also, the neighbors of the atoms near the boundaries in a particular range (cutoff range, r_c) are enabled to reach the opposite side of the box if the range is beyond the boundaries in the calculation of the atoms interactions.

The introduction of PBC in the classic mechanics enables the real system be simulated with relatively small number of atoms without significant deviations. However, even with PBC, finite size effects can not be totally eliminated. In the real application, the size of the simulation system depends on the kind of system and the properties of interest. For example, when the long range interactions are considered and important, the system size should exceeds the range that the long range significant correlations covers. Taken the advantages of current progress of the computation techniques, the simulations of large size involved effects, such as the study of fracture behaviors in bulk materials, are applicable.

In the system of the MD simulation, the initial position of each atoms is given, either by randomly placed in the simulation box or obtained from experimental structures, such as the x-ray crystal structures or from other simulation methods. The motion status of the atom is subject to change due to the force exerted on the atom. Newton's second Law governs the motion change in the MD simulations. The status of the atom i with mass m_i in the simulation box can be determined by the position r_t^i and velocity v_t^i at the simulation time t. When $t = 0$, the system is at the initial state and the atom i has initial value (r_0^i, v_0^i). At time t, the force f_t^i exerted on atom i can be obtained by the atoms interaction potentials,

$$f_t^i = -\nabla_{r_i} U\left(r_t^1, r_t^2, \ldots, r_t^N\right) \tag{I.2}$$

Where N is the total number of the atoms in the box. Then the acceleration of the atom i gained at time t is

$$a_t^i = \frac{f_t^i}{m_i} = \frac{d^2 r_t^i}{dt^2} \tag{I.3}$$

The velocity for the next time step $v_{t+\Delta t}^i$ of atom i can be calculated from the acceleration a_t^i, so does the position of the next time step $r_{t+\Delta t}^i$ by integrating the motion equations over time Δt. Δt is the time interval between two neighbor time steps in MD simulations. For example, when the time interval Δt is sufficient small, the acceleration can be considered constant without noticeable errors, then the velocity for the next step is

$$v_{t+\Delta t}^i = v_t^i + \Delta t \cdot a_t^i \, , \tag{I.4}$$

Again integrate the motion equation to get the atom i position after Δt

$$r_{t+\Delta t}^i = \int_t^{t+\Delta t} v^i dt + r_t^i \tag{I.5}$$

Therefore only the initial positions of the atoms and an initial distribution of velocities are needed to calculate a trajectory. The accelerations of the atoms can be determined by the gradient of the potential energy function. The equations of motion are deterministic, e.g., the positions and the velocities at time zero determine the positions and velocities at all other times. And equations of motion are reversible in time. If the signs of all the velocities and momenta are changed, the atoms can trace back their trajectories.

The potential energy is a function of the atomic positions ($3N$) of all the atoms in the system. Because of the complicated nature of the interatomic interactions, the equations of motion can only be solved numerically. Numerous numerical algorithms have been developed to integrate the equations of motion. A good algorithm should be able to conserve the energy and momentum of the system and permit a long time step for integration at the same time it can be proved to be computationally efficient. The typical MD simulation procedures are illustrated in figure I-1.

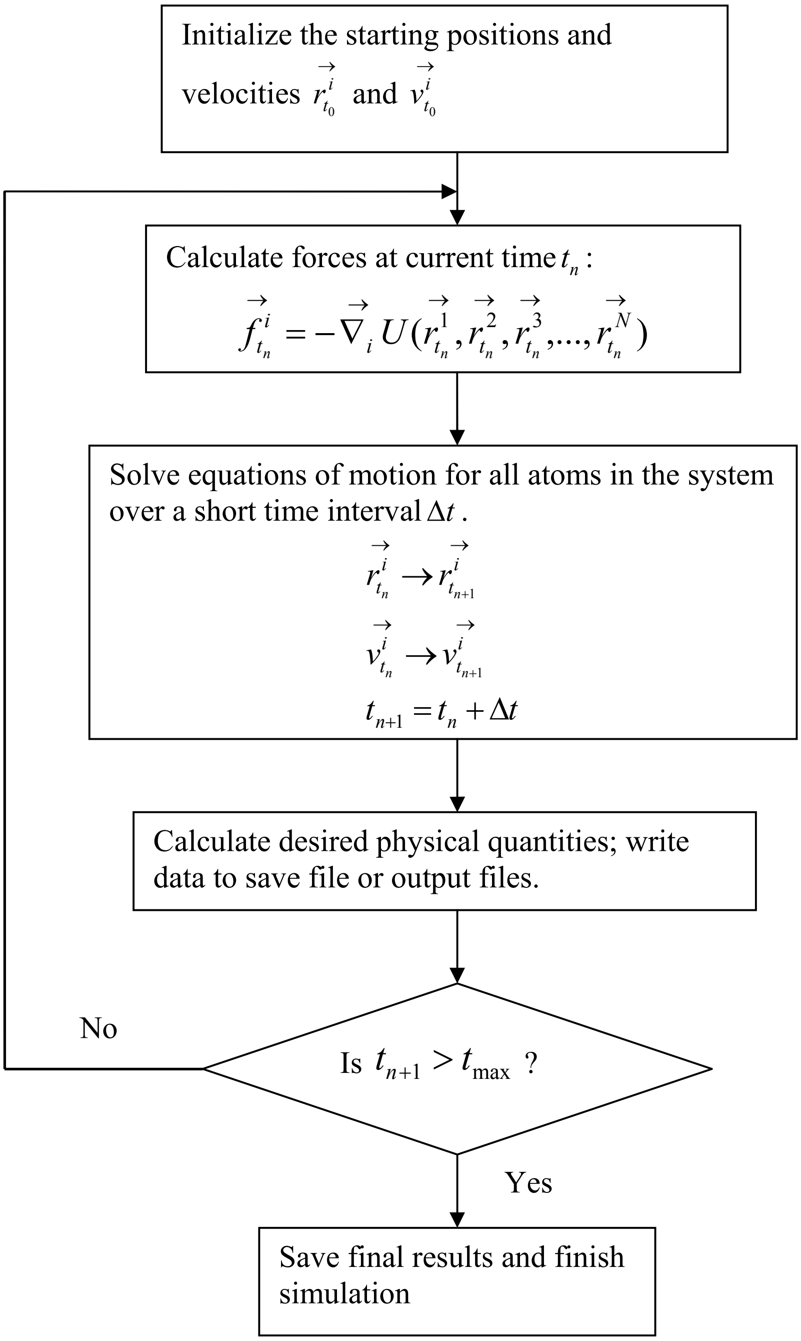
Initialize the starting positions and velocities $\vec{r}^{\,i}_{t_0}$ and $\vec{v}^{\,i}_{t_0}$
Calculate forces at current time t_n :
$\vec{f}^{\,i}_{t_n} = -\vec{\nabla}_i U(\vec{r}^{\,1}_{t_n}, \vec{r}^{\,2}_{t_n}, \vec{r}^{\,3}_{t_n}, ..., \vec{r}^{\,N}_{t_n})$
Solve equations of motion for all atoms in the system over a short time interval Δt .
$\vec{r}^{\,i}_{t_n} \to \vec{r}^{\,i}_{t_{n+1}}$
$\vec{v}^{\,i}_{t_n} \to \vec{v}^{\,i}_{t_{n+1}}$
$t_{n+1} = t_n + \Delta t$
Calculate desired physical quantities; write data to save file or output files.
No
Is $t_{n+1} > t_{\max}$?
Yes
Save final results and finish simulation

Fig. I-1 The schematic of a typical MD simulation

Molecular Dynamics simulation has gained numerous successes in the theoretical and practical applications. In the studies of liquid and amorphous phase materials, MD is a very important tool even from the first day when it was introduced. The amorphous phase, the lack of long-range orders distinguishes it from the crystal phase though the short-range orders are similar in both phases. MD simulation elucidates the system from the starting point to provide the atomistic structures of the materials whether it is crystalline or amorphous. In the studies of intergranular films between crystal grains, the amorphous nature of the thin film makes the MD simulations unparalleled among all the techniques being used.

I.3 The Intergranular Films Between Crystal Grain in Ceramics

In certain ceramics like Al_2O_3, Si_3N_4, SiC, $SrTiO_3$, etc., the grain boundary (GB) region can have an amorphous film of about several nanometers thickness[12-20]. The presence of intergranular films (IGFs), along with its structure, plays an important role in determining the properties of the whole ceramic. Beyond the profound effects on the normal physical and chemical properties of the ceramics, like the density, oxidation and the electrical behaviors, the IGFs even have a key role in the mechanical properties of the ceramics, as well as in the fracture mechanism. It is well established that many of the high-temperature properties (creep deformation, creep fracture, oxidation and corrosion resistance) of the silicon nitride based ceramics are decided by the properties of the intergranular phase at these temperatures[21-23].

The IGFs in the ceramics can be produced by a number of different sintering processes. In many ceramics sintered from the liquid-phase process, the IGFs are present naturally in the finally products[24-27]. Examples of these include silicon nitride and alumina substrate materials. In these materials, particularly the covalent ceramics, particular short-range, the repulsive force between grains is larger than the Van der Waals dispersion force. But in the large separation distance, the net force between the grains will be attractive. An equilibrium stable thickness of IGF is the results of the interplay between the two forces. Moreover, the stable thickness is found to be strongly dependent on the dielectric properties of the adjacent grains.

Though the extremely small dimensions of the thin films make the precise detection in the experiments very difficult, the TEM and HRTEM combined the analytical electron microscope (AEM) revealed some initial interesting aspects of the IGFs, including the facets of the crystal grains and the chemistry properties[19, 34-37]. The grain boundaries in polycrystalline ceramic oxides are faceted at the submicrometer level and the low-index facetings are favorable. In alumina ceramics, faceting of low-index planes has been observed at the structured grain boundaries, such as basal twin boundaries and rhombohedral twin boundaries[38]. However, this faceting could exist without the presence of the IGFs, although the IGFs may enhance this effect by accommodating some special species to fill the open sites at the crystal surface. The low energy of the low-indexed grain boundary provides a possible reason for the faceting.

In alumina ceramics, the thin amorphous phase contains silicon and calcium species typically[31, 39]. They are the most common contaminants in the commercial alumina powders. At typical sintering high temperatures, alumina crystals have very limited solubility for most of the impurities[40-42]. The impurities then were expected to move out to the triple junctions and the grain boundaries from the interior of the crystal grains during the sintering. So IGFs were not only observed in the liquid phase sintering in which the amorphous phases were introduced initially in the sintering procedures. The open site of the grain boundaries may trap some particular species either from the bulk grains or from the amorphous phase itself and such impurities will accumulate at the grain boundaries when the sintering continues, i.e., the segregation of the impurities[43]. The strain misfit caused by the calcium substitution in the aluminum sites in the lattice was concluded as the driving force for the segregation. The phenomenon of the Ca substituting the Al at the grain surfaces to occupy the open sites was detected by Auger Electron Spectroscopy (AES) from the as-fractured and sputtered surface of alumina ceramics[40]. It was also observed that the concentration of Ca at grain boundaries changes slightly with change of the CaO concentration in the raw sintering powders[41]. The segregation of the Ca and Si atoms at the grain boundaries may reduce the interface energies. For example, Handwerker[38], et al., observed a widening of the dihedral angle between grains, which in turn of the decreasing of the interface energies, as the local concentrations of Si and Ca impurities increased.

The anisotropic segregation of Ca to the surface of the alumina grain boundaries was observed in some studies. The preferential segregation to the basal (0001) plane and other low index planes, like (1010) plane, in contacting with the CAS glassy phase was reported[44-47]. After investigating the interfaces between basal (0001) Al2O3 and Al in melt-infiltrated polycrystalline alumina composites by HRTEM and AES, Kaplan[41] found the preferential segregation of Ca at the basal surface of alumina as well as the basal twin boundaries. The excess of Ca was determined to be 2.5±0.5 Ca atoms/nm^2 in the former and 1.0 ±0.5 Ca atoms/nm^2 in the latter respectively.

Another important phenomenon in the ceramics with the IGFs is the anisotropic grain growth. The growth rate of some special facets of the grains, generally the basal and some other low index facets, will gain excess growth rate than other ones with the presence of IGFs. The final structures of the ceramic are characterized by the elongated grains. In particular, the abnormal grain growth (AGG) happens in ceramics when one of the facets grows extraordinarily fast and has a large ratio as opposed to equiaxed grain facets, which has a negative effect on the strength of the products sometimes. Higher grain growth rates for certain plains can be due to relatively low interfacial energies for those planes[48], which providing a higher driving force for growth or low activation energies for growth. Also AGG is strongly related to the species segregated to the grain boundaries. Ca and Si atoms in the IGFs are believed to enhance the AGG while Mg can prevent the AGG above certain concentration[29, 49, 50]. In the sintering of 99.999 wt% pure alumina in the clean environment at 1900^0C, the absence of the elongated grains in the sintered structures suggests that the AGG is suppressed effectively[29]. Beside the well established facts that certain species like Ca and Si trigger the AGG at high temperatures, Bae and Baik[16] determined the relationship between the amount of Ca/Si and the AGG quantitatively. At 1900^0C, the critical concentration of Si in alumina ceramic to create AGG alone was 300 *ppm*, while for Ca alone it is only 20 *ppm*. However, the co-doping of Si and Ca in the alumina grains can reduce the critical concentration significantly. In their experiments, AGG was observed with only 200 *ppm* Si and 10 *ppm* Ca together. Based on the results of ultra-pure alumina sintering and the Ca/Si doping alumina sintering, another conclusion was obtained that the appearance of glassy phase between the grain boundaries is necessary for the onset of AGG.

It was observed that the interfacial microstructure is strongly related to relative CaO-SiO_2 doping level at the starting point[51]. The high concentration of impurities in the starting powders can substantially modify the features of CAS liquids at the interface region, thereby strongly influencing the Al_2O_3 grain growth across the interface. It was proposed that the structure of the interfaces and the grains growth could be controlled by the different combination of CAS glassy phase presented in the ceramics. Song and Coble[30] observed the formation of plate like abnormal grains in alumina containing a large amount of liquid-phase, including SiO_2. The fast grain growth rate of the plate like grains was explained by an increased interfacial reaction rate due to the impurities. At the same time the impurities made the basal place, which appeared as the flat boundaries, the lowest energy plane. In another study, the microstructure changes based on the Ca doping level was examined by SEM[52]. The critical excess concentration of Ca at the grain boundaries to create elongated grain was determined as C_{Ca} =3-3.5 atom/nm^2 at 1500^{0}C and above. The reason for the elongated grains was explained by the preferential segregation of the Ca to the (0001) basal plane. AGG was observed with a critical C_{Ca} = 4.5 atoms/nm^2 at same high temperatures. However, even with C_{Ca}= 11 atoms/nm^2, only few grains grew abnormally without significant affecting the average grains size at 1400^{0}C. The results were consistent with Bae and Baik's observations. Moreover, the temperature dependence of the AGG and the cooperation between different species like Ca and Si suggested that some complicated physical/chemical procedures were involved in AGG.

As mentioned above, AGG can also happen in non-liquid phase sintered ceramics but with the impurities contained in the starting powders. In such ceramics, AGG does happen generally at some certain sintering stage. The reason was found to rely on the segregation of impurities to the grain boundaries due to their solubility limit in the grains.

additives were deliberately introduced into the green powders so as to promote or facilitate densification during firing. In the second, the IGFs existed because the materials are prepared by the controlled but incomplete crystallization of a glass phase. In other ceramics, though no amorphous or liquid phases existed in the starting powders or added in the materials during sintering, the IGFs were found in the final structures because of the impurities in the starting powders or from the environment. Studies on these ceramics are particularly important because most commercial ceramics can’t be made free of impurities and the completely clean environments are not applicable in practice[28, 29]. The existence of the IGFs is the result of the solute limit of the impurities in the crystalline phases and the inability of the impurities species crystallization into some distinct phases.

In the liquid phase sintering procedures, the liquid phase existed between grains and the crystalline grains grew out of the liquid phase[30-32]. As the grains grow, the dimension of the liquid or amorphous phase between the grains will decrease as a consequence, until an equilibrium thickness of IGF is obtained. Though there were some structure changes in the IGF confined in the small region, the nature of the IGF is considered as amorphous and it would behave like liquids at high temperatures.

The equilibrium thickness of the IGFs can be up to 2 nm in silicon nitride and zirconia ceramics and up to 5 nm in some alumina based materials[33]. Two approaches, one based on the interfacial energies and the other on force balance were explored to explain the equilibrium thickness of the IGF between the grains. The experimental results of the CAS liquids penetrated into the crystal grains in the alumina ceramic showed that there is a net repulsive force acted on the grain which separated them. It indicated that in

A glass phase was formed at the interface and the concentration of the impurities in the glass phase increases as the grain growth. The microstructures changes of the grain surfaces and the widening distribution of the interfacial energy because of the impurities segregation resulted in AGG, which is consistent with the observations that the critical concentration of AGG exists. A similar mechanism was applied to explain the chemical imhomogeneties effects in ceramics.

Beside the impurities like Ca and Si which will trigger the AGG in the ceramics, Mg can prevent the AGG or suppress the effect of Ca and Si if the concentration of Mg is high enough[53-55]. The effect of MgO in the IGFs was observed to reduce the mobility of grain boundaries, change the viscosity of the glassy phase and modify the grain/glass interface.

I.4 The Computer Simulations in the Study of IGFs

The application of first-principles simulations in IGFs is limited due to the large number of atoms, which are required to construct the amorphous phase and the confining boundary conditions correctly. However, it can be useful to calculate some certain atomic configurations in the IGFs, such as favorable segregation sites of rare-earth atoms, stable crystalline phases formed by IGF constituents[56]. Also it can be used to relax the amorphous phase structure obtained by MD simulations to get some additional information like the electronic band structures of the system[57], which can be used to simulate the electron energy related spectra as they could be observed in the experiment.

Grand Canonical MC simulation was introduced in the studies of the IGFs[58]. In such a model, the atoms from a large pool of atoms presented in the triple pockets, which was assumed as an open system with infinite atom reservoirs, were selected to fill the IGFs with some certain limitations. The atoms in the IGF can not only change their positions by the displacements, but also the compositions, i.e., the type of atoms can also be changed by the exchanges between the IGFs and the atom reservoir. Therefore the compositions of IGFs may not be determined from the amount of additives in ceramics, rather they are related to the amount of species left in the reservoir. Therefore the limitation of the actual finite pocket size and the amount of the certain species in the reservoir does have an influence on the IGF systems in GCMC simulations.

MD calculations provide a way to build atomic IGF models just from an accurate knowledge of the forces between the atoms and the thermodynamic boundary conditions of the finite sized system. It will not have the limitations as in GCMC. Since the atom trajectory can be obtained in MD, not only the structure properties, but also the dynamic properties, like the diffusion and viscosity can be calculated in MD simulations.

II. Computational Procedure

Molecular-dynamic simulations were made using a multibody potential that includes both a pairwise modified Born-Mayer-Huggins potential and a three-body potential, given as

$$V = \sum_{i \neq j} V_{ij}^{BMH} + \sum_{i \neq j \neq k} V_{jik}^{3-body} \tag{II.1}$$

where V_{ij}^{BMH} is the pairwise modified BMH potential term and V_{jik}^{3-body} is the three body potential term. The modified BMH potential is defined as

$$V_{ij}^{BMH} = A_{ij} \exp\left(\frac{-r_{ij}}{\rho_{ij}}\right) + \frac{z_i z_j e^2}{r_{ij}} erfc\left(\frac{r_{ij}}{\beta_{ij}}\right) \tag{II.2}$$

The first term is the repulsion term in the modified BMH pair potential and represents the core electron overlap when the two atoms get too close; the second term is a screened Coulombic interaction with the cutoff distance as 5.5 angstroms. r_{ij} is the separation distance between the ions i and j, z_i and z_j are the formal charge of the ions and β_{ij} is a species dependent term that reduces the formal charges as a function of distance between the ij pair. The value of the parameters A_{ij} , β_{ij} and ρ_{ij} for each pair type were determined in this lab previously and are listed in Table II-1. Atomic charges for silicon, oxygen, aluminum, calcium and nitrogen ions are +4, -2, +3, +2 and -3, respectively.

The partial covalent bonding of the species has preferred bonding angles at which the bonded species have the lowest energy. When the bonding angle deviates from the preferred one, the energy will increase. The 3-body potential accounts for this effect by raising the energy on a central ion within a triplet as the angle deviates from an ideal angle. The 3-body potentials applied to all Si, O, and Al ions as central ions i are given as:

$$V_{jik}^{3-body} = \lambda_{jik} \exp\left(\frac{\gamma_{ij}}{r_{ij} - r_{ij}^0} + \frac{\gamma_{ik}}{r_{ik} - r_{ik}^0} \right) \Omega_{jik} \qquad \text{(II.3)}$$

when $r_{ij} < r_{ij}^0$ and $r_{ik} < r_{ik}^0$.

Otherwise,

$V_{jik}^{3-body} = 0$ when $r_{ij} > r_{ij}^0$ and $r_{ik} > r_{ik}^0$,

The angular part, Ω_{jik}, is given as

$$\Omega_{jik} = \left(\cos\theta_{jik} - \cos\theta_{jik}^0\right)^2 \qquad \text{(II.4)}$$

for the Si/Al-O-Si/Al and O-Si-O structure, while for the O-Al-O triplet, it is defined as

$$\Omega_{jik} = \left[\left(\cos\theta_{jik} - \cos\theta_{jik}^0\right)\sin\theta_{jik}\cos\theta_{jik}\right]^2 \qquad \text{(II.5)}$$

where the three atoms form angle θ_{jik} with the central atom as the vertex i in these triplets for both conditions. For the ionic species, like Ca, no 3-body potential centered on such ion as i in the jik triplet is used. The 3-body potential has been previously discussed [59, 60] and has been shown to give good results in comparison to experimental data or ab-initio calculations for sodium silicate glasses [61], sodium alumino-silicate glasses[62] and polymerization of silicic acid molecules [63, 64]. The equilibrium tetrahedral angle is 109.4^0, but it has a large range for different triplet combinations in the composites/crystal, such as Si/Al-O-Si/Al and O-Si/Al-O, to form appropriately coordinated structures. The parameters are listed in Table II-2.

Table II-1. Parameters for Modified BMH Pair Potential

Atom Pair	A_{ij} (fJ)	β_{ij} (pm)	ρ_{ij} (pm)
O-O	0.0725	234	29
Si-Si	0.1877	230	29
Al-Al	0.0500	235	29
Ca-Ca	0.7000	230	29
Si-Al	0.2523	233	29
Si-Ca	0.2215	230	29
Al-Ca	0.2178	230	29
Si-O	0.2962	234	29
Al-O	0.2490	234	29
Ca-O	0.5700	234	29
Si-N	0.7800	241.3	25.89
N-O	0.1350	230	29
N-N	0.07241	261	29

Table II-2. Parameters for 3-body Potential

Atom triplet	λ_{ij} (fJ)	γ_{ij} (pm)	r_{ij}^{0} (pm)	θ_{jik}^{0}
Si-O-Si	0.001	200	260	109.5
Al-O-Al	0.001	200	260	109.5
Al-O-Si	0.001	200	260	109.5
O-Si-O	0.024	280	300	109.5
O-Al-O	0.024	280	300	109.5
Si-N-Si	0.0035	260	280	120
N-Si-N	0.024	280	300	109.5
O-Si-N	0.024	280	300	109.5

III. Molecular Dynamics Computer Simulations of the Interface Structure of Calcium-Alumino-Silicate Intergranular Films between Combined Basal and Prism Planes of α-Al_2O_3

III.1 Introduction

Intergranular glassy phases play an important role in the sintering of alumina. The final sintered structure of the crystals is not only affected by the liquid sintering process, but also by the impurities contained in IGF. Bae and Baik showed the effect of small concentrations of silica or calcia in the IGF on abnormal grain growth in alumina [16]. Grain size, distribution, and grain shapes are considerably altered with impurity calcium silicate phases present as compared to the pure alumina (>99.999%) sintered ceramics [53]. In sintering, densification and grain growth occur simultaneously as intergranular pores are removed through grain boundary diffusion. However, further densification was prevented when a few excessively large grains appeared after abnormal grain growth (AGG)[53]. Sintering of alumina powder containing impurities resulted in platelike planes and a wide range of grain sizes[47]. Numerous experimental and theoretical studies have been attempted to understand the origin of AGG in alumina and it is clear that AGG occurs when the intergranular films (IGF) containing SiO_2, Al_2O_3 and CaO are present between different facets of the alumina grains during sintering. These impurities may either come from the starting powders or be added particularly during sintering. Bae and Baik showed that pure alumina can be sintered with no AGG in certain conditions [49].

Small amounts of impurities like CaO and SiO_2 segregate strongly to the surfaces and grain boundaries of Al_2O_3, even if the concentration of such impurities was under the solubility limits[40]. For example, a few ppm Ca present in the Al_2O_3 powder showed very high concentrations of Ca in the grain boundaries of sintered alumina [40]. Baik[40] investigated Ca segregation behavior at several planes of alumina grains of commercial Al_2O_3 powder. Results showed that Ca accumulation is anisotropic. For the (0001) plane, no obvious Ca segregation was observed or the Ca concentration was under the Auger Electron Spectroscopy (AES) detection limit, but strong enrichment of Ca on the $(10\bar{1}0)$ plane occurred. Results were affected by the sintering conditions and segregation was limited to the first monolayer at the interface. In each condition, a 2-D surface phase transition and reconstruction was observed. Ca was found in all of the grain boundaries analyzed in Ca doped alumina[65]. However, its concentration at the grain boundaries varies from boundary to boundary. McCune and Ku[66] also found that massive enrichment of Ca occurs in the rhombohedral planes as well as in the polished surfaces of dense polycrystalline alumina. On the other hand, the dihedral angles in alumina containing Ca and Si impurities have a wide distribution, apparently due to the wide distribution of grain boundary energies or change in energy with grain boundary plane for a given misorientation [38]. The grain boundary energy difference may be a possible reason to explain Ca segregation at different Al_2O_3 grain boundaries [67], although the relationships between them still need further study. Moreover, the atomistic structure in the IGF and at the interface and its relationship to the AGG is not so clear because of the experimental difficulties imposed by the extremely thin IGF region.

MD computer simulations describe atomistic level interactions of different species and have been used extensively and successfully to provide atomistic interpretations of structures and properties in glass and crystals. We have previously performed studies of silica and silicate glass structures and impurities at the interface between the alumina and the IGF. Some results have been obtained regarding the structure and behavior of the α- and γ-alumina surfaces[68], silica-alumina interfaces[69], and calcium silicate-alumina interfaces[70]. We showed that the alumina basal (0001) plane has lower surface energy than the $(11\bar{2}0)$ and (1100) surfaces; moreover, the data show that single layer Al terminated (0001) plane and oxygen terminated $(11\bar{2}0)$ plane are energetically favorable. The surface energy of the (0001) termination was in agreement with previous molecular statics calculations[71] and subsequent density functional theory (DFT) calculations[72] ($2.03 J/m^2$ MD result vs $1.95 J/m^2$ DFT result). The simulations also showed significant relaxation of the terminal Al plane in the Al terminated (0001) surface, which is consistent with DFT calculations[72]. Simulations of the formation of the interface between a silica IGF derived from *in-situ* polymerization of silicic acid molecules and α-alumina basal planes showed the formation of an ordered cage-like structure at the interface region[69]. The Al atoms from the surface of the Al_2O_3 crystal became tetrahedrally coordinated and formed the base cations of the 'cages'. Hydrogen, which is present in the IGF after the simulated polymerization reactions, segregated preferentially to the cages[69]. In the simulation of calcium silicate IGF formed from a melt/quench process between the (0001) planes of α-alumina, this ordered cage-like structure was also observed[70]. Ca ions preferentially segregated to the cages. Si ions occupied cage sites only with zero or low Ca content in the IGF, although the presence of Si within the cage site was highly strained and was probably a kinetically restricted result that required longer simulation times for removal. Similar behavior occurred in sodium silicate IGFs[73].

Since, in real liquid phase sintering of alumina, Al ions transport through the IGF to the destination sites and the alumina grain grows, it is reasonable to account for the Al_2O_3 species in IGF to get a better understanding of the impurity atom segregation and the interface reactions during sintering. Actually, a high concentration of Al_2O_3 is found in the intergranuar films [54, 55, 74], with calcium alumino-silicate compositions similar to anorthite. Al_2O_3 additions to the IGF in previous simulations showed that Ca atoms still segregated to the cages[75].

In this study, different compositions of CAS IGFs between the alumina (0001) plane and the $(11\bar{2}0)$ plane were studied by MD simulation. MD simulation techniques used previously by our group were applied here. The structure of the IGF/crystal interfaces, and the similarities or differences, were studied using atom distribution and coordination number of all species at the two different interfaces and in the IGF.

III.2 Computational Procedure

Four different calcium-alumino-silicate IGF compositions were chosen as listed in Table III-1. In the four compositions listed from top to bottom in the table, the mole concentration of Al_2O_3 is in the decreasing order of 40%, 25%, 20% and 17% respectively. The labels used here (column 1 of Table III-1) are indicative of the calcia-alumina-silica mole ratios, as listed in column 2. The compositions were chosen because of data on the crystalline analogs. The glassy IGFs were made between two dissimilar α-alumina orientations, the (0001) and $(11\bar{2}0)$, creating a ((0001) oriented crystal)/(IGF)/(($11\bar{2}0$) oriented crystal) system, and is shown schematically in figure III-1.

Table III-1. The compositions of 4 different IGFs

Sample No.	Mole ratio CaO : Al_2O_3 : SiO_2	Specific Number of Atoms				TOTAL
		Ca	Al	Si	O	
112	1:1:2	665	1330	1330	5320	8645
313	3:1:3	1296	864	1296	5184	8640
216	2:1:6	640	640	1920	5440	8640
14535	14:5:35	770	550	1925	5445	8690

The crystal/IGF/crystal systems were made according the following procedures. First, the two differently oriented crystals were generated, one with the single Al layer terminated (0001) plane exposed at the surface and another with the single O layer terminated $(11\bar{2}0)$ plane (these terminations are the lowest surface energy configurations of their respective orientations[68]). System sizes were 7920 and 8640 atoms, respectively. Each crystal was continuous in 2-dimensions by applying periodic-boundary conditions in x and y directions. Second, for each IGF composition, a stoichiometric mixture of ions was created by placing each type of atom randomly in a 'box' with the same x and y dimensions as the crystals (and a starting z dimension of ~5 nm). The third step, the random mixture of IGF ions was placed between the crystals with (0001) Al-terminated plane at the bottom of the IGF and the $(11\bar{2}0)$ O terminated plane at the top (in the z-direction) of the IGF. The final configuration is like a 'sandwich' structure. The last part of the process was a high temperature melting of the atoms in the IGF and quenching through intermediate temperatures to room temperature in order to create the glassy IGF between the differently oriented alumina crystals. The x and y dimensions of this structure are about 5.2 nm and 5 nm, the z dimensions of the component parts, (0001) alumina crystal, IGF, and $(11\bar{2}0)$ alumina crystal, are about 2.5 nm, 5 nm and 2.5

nm respectively. Again, the configuration of the simulation system is illustrated in Figure III-1.

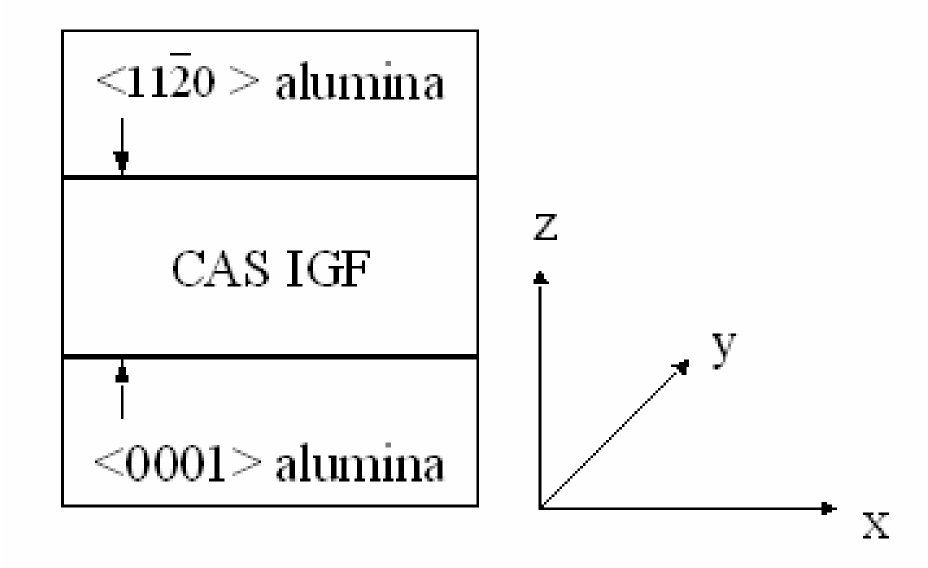

Fig. III-1 A simple illustration of the structure of simulation system

A melt/quench procedure was used to produce the glassy IGF. Similar to simulations of bulk glasses, the simulated quench is much more rapid than normal experimental procedures. However, simulated bulk glass structures are very similar to experimental data based on radial and pair distribution functions, static structure function, NMR, and EXAFS data, and have been documented in the past[62, 76-82].

In the melt/quench procedure to form the glassy phase IGF and the resultant interfaces between the IGF and the alumina crystals, the ‘sandwich’ structure system was heated to 10000K for 10 ps under constant energy and constant volume ensemble (NVE) conditions, with all alumina atoms immobilized to prevent the melting of crystals. At lower temperatures in the quench, a constant pressure was applied in the *z* direction (perpendicular to the IGF/crystal interfaces) to overcome the internal pressure of the melt in order to allow the IGF to reach an appropriate density under modified constant pressure and temperature (NpT) conditions. In the quench from the melt to 300K, the system was run for 20ps at 8000K, 40ps at 6000K, and 40ps at 4000K. In order to minimize mixing between IGF ions and those in the crystals, the atoms in the crystals did not respond to the interatomic forces at these higher temperatures, although they did move en masse in response to the applied pressure of 5GPa in the z direction. This enabled the IGF to reach an appropriate thickness for the composition and number of atoms in the IGF. The desire to minimize intermixing between IGF and crystal atoms at the higher temperatures was done to enable formation of a more ideal, flat, interface so that subsequent data analysis would be facilitated. Clearly, some degree intermixing and interface roughness might be expected in real systems. At 3000K and below, atoms in both the crystals and the IGF responded to both the interatomic forces and the external pressure. Although the atoms in the bottommost 0.63nm of the (0001) oriented (bottom) crystal and the topmost 0.47nm of the upper crystal were kept frozen (but still moved to the external pressure, all other atoms in the system moved according to the interatomic forces and pressure. These remaining frozen atoms are sufficiently far from the IGF/crystal interfaces and do not affect interface behavior. Since the frozen atoms never act as atoms *i* in the equations above, these frozen atom regions enable periodic boundary conditions to be used in the z dimension without the moving atoms in each crystal seeing the atoms in the other crystal across the z-dimension periodic boundary. The simulation time for 3000K was 50ps and 100ps for both 2000K and 1000K to insure atoms sufficiently relaxed in the IGF and at the interfaces. Finally, the whole system was relaxed at room temperature (300K) for 20ps. The applied pressure was decreased with the system cooling and atmospheric pressure was applied at 300K. Though the crystals are frozen at high temperatures, the whole structure is relaxed according to the crystal thermal expansion and the glass relaxes initially at the interfaces with the frozen crystals. At lower temperatures, the x and y dimensions of the crystal are again governed by the thermal expansion coefficient, minimizing elastic effects, while the pressure in z governed the z dimension. Again, this latter feature allowed the atoms in the IGF to relax to the appropriate thickness for the given number of IGF atoms and the structural effects induced by the crystals.

III.3 Results and Discussion

The ordered cage structure previously observed[70, 73] at the interfaces between the calcium and sodium silicate glassy IGFs and alumina basal planes (with or without the presence of Al atoms) was observed again in this study at the calcium-alumino-silicate and Al_2O_3 (0001) plane. Figure III-2 shows a snapshot of the side view of a thin section (into the plane of the image) of the local configuration of ions at the (0001)/IGF interface of 112 system (similar structure appeared at this interface for all four systems). In this figure, and the following figure, the atoms originally from the IGF and from the crystals are separated by a dashed line; the atoms above the line are from the IGF and below the line are from the crystal, as shown in the figures. Also different sizes are assigned to each type of atom. For a better view of this structure, the sizes of the atoms in the figures are not based on the actual ion sizes used in the simulations. Only the strong network forming bonds are drawn to first neighbors in the figure, consistent with the first peak in the pair distribution functions. No Ca-O bonds are drawn, although, of course, bonding between Ca and O exists. This ordered interface structure has been discussed previously[75]. In such a structure, oxygen atoms from the IGF adsorb onto the surface of the crystal onto the Al sites that make up the terminal layer in the basal plane of the crystal. These oxygen atoms form the side wall of the "cages" which hold the Ca atoms that segregated from the IGF. The upper portion of the cage is composed of Si and Al atoms from IGF. These structural features were discussed in previous simulations[68-70, 73, 75]. The fact that the cage structure is observed in the current and previous simulations that differ significantly in composition (sol-gel prepared IGF, calcium silicate IGF, calcium alumino-silicate IGFs, and sodium silicate IGFs), quench rates, and system sizes attests to the fact that the initial conditions do not bias the final interface structures.

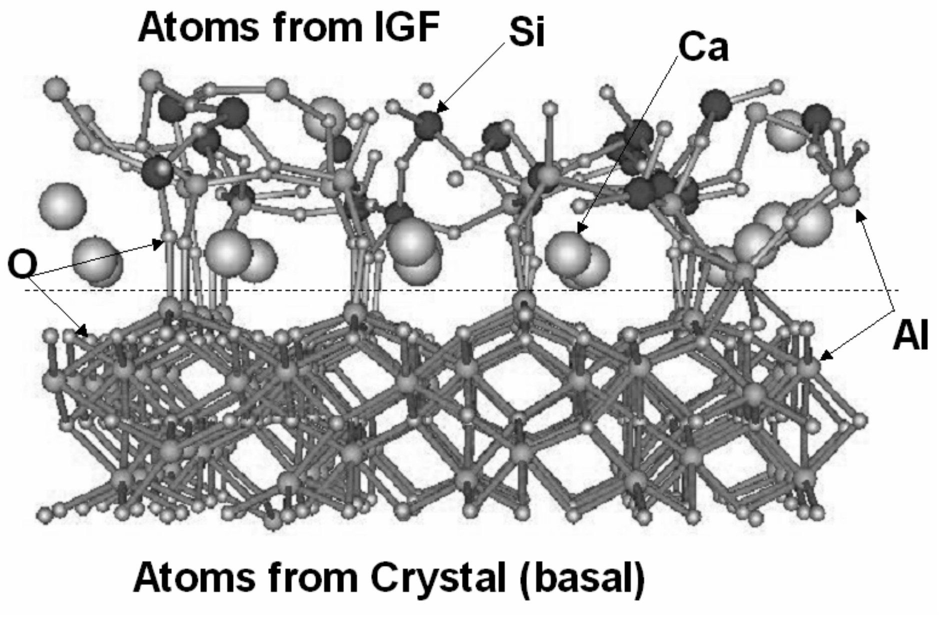

Fig. III-2 Snapshot of the side view of the local configuration of ions at the (0001)/IGF interface of 112 system. Dashed line separates atoms originally in the IGF from those in the crystal.

Figure III-3 shows the snapshot of a side view of the $(11\bar{2}0)$/IGF interface of the 112 system. Although the $(11\bar{2}0)$ surface is O-terminated, O from the IGF adsorb epitaxially onto the surface at the undercoordinated Al ions present on the crystal surface. Interestingly, among the cations in the IGF, the Al atoms preferentially segregate to the crystal surface prior to Ca and do so epitaxially. However, some Si atoms also enter this ordered surface structure as defects. This will be discussed more fully below.

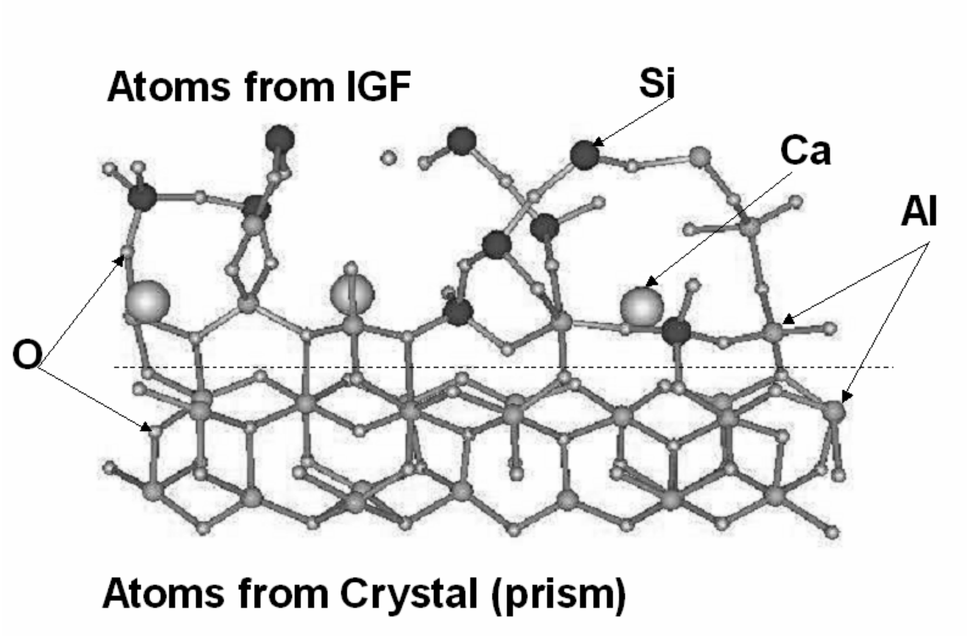

Fig. III-3 Snapshot of a side view of local configuration of the $(11\bar{2}0)$/IGF interface of 112 system. Dashed line separates atoms originally in the IGF from those in the crystal.

III.3.1 Atom Number Density Analysis

Figure III- 4 shows the density profile of all atoms in the 112 CAS system as an example of the general features shown in all four compositions studied here. Detailed differences will be presented below. In figure III-4, the alumina crystal with the basal plane oriented parallel to the crystal/IGF interface is at the left while the crystal with the prism plane oriented parallel to the interface is at the right. The density profiles of the atoms in the crystals are shown as the thinner lines. The difference in the density distributions of the Al and O atoms in the crystals at the left and right is due to the different crystal orientations. The atoms from the IGF are shown as thicker lines between the two crystals.

Fig. III-4 Density profile of all atoms in the 112 CAS system. Basal oriented crystal on left, prism oriented crystal on right. Heavier lines indicate individual species from the IGF. 'Cation from IGF' is sum of all cations in the IGF.

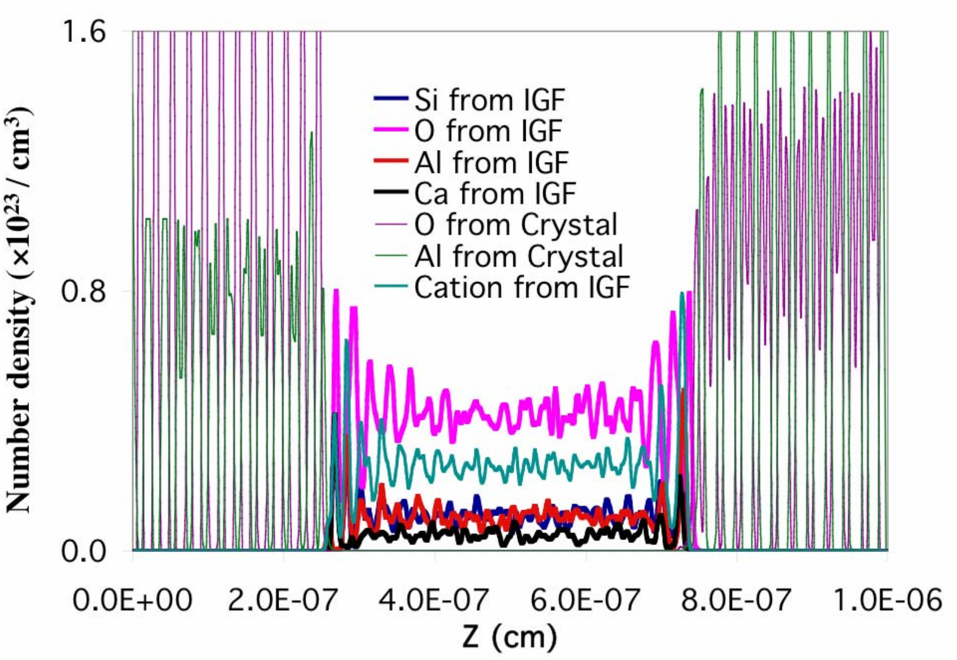

An ordering of the atoms in the IGF occurs at both interfaces, as seen in the peaks of the IGF species formed at each interface. These peaks decay into the IGF, where the center of the IGF reaches the appropriate glass density. The decay length of this ordering that is induced by the crystal is ~1.0-1.5nm into the IGF and is present in all IGF compositions studied here. Again, because of this similarity, the complete density profiles of the other three IGF systems, 313, 216 and 14535, are not shown. However, higher resolution density profiles of all 4 systems at each interface are shown in subsequent figures because of the important differences in the height of some specific peaks at the ordered interface due to the compositional difference in the IGFs and the different crystal surfaces.

Figure III-5 shows the higher resolution density profile of the specific interfaces: (a), (b), (c) and (d) are the interfaces at the alumina basal plane with the 112, 313, 216 and 14535 IGF systems, respectively; (e), (f), (g) and (h) are the alumina prism plane interfaces with the 112, 313, 216 and 14535 IGF systems, respectively.

In Figure III-5(a-d), the first peak to form closest to the crystal is a small peak from Al originating from the IGF and adsorbing onto the (0001) plane. This peak, and the next two peaks, are delineated in III-5a by the arrows. The second set of peaks away from the interface comes from O and Ca from the IGF that occur at the same location and are consistent with the location of these ions in figure III-2. The third set of peaks contains Si and Al ions that form the top of the cage structure shown in figure III-2. The heights of the second and third sets of peaks change slightly with composition.

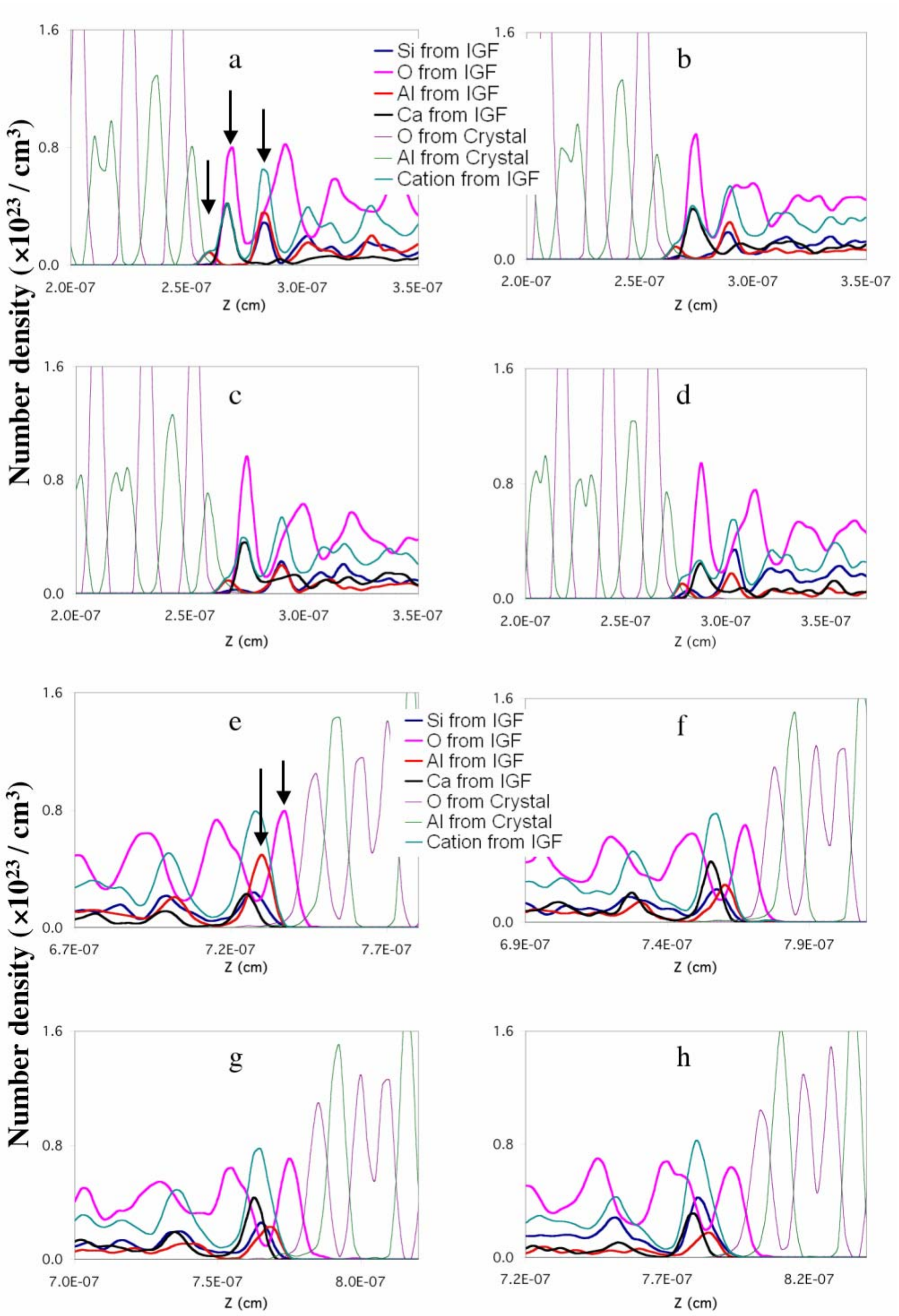

Fig.III-5 Higher resolution graphs of the density profiles of the specific interfaces and compositions. (a-d) Basal oriented crystal is on the left of images, compositions 112, 313, 216, and 14535, respectively. Arrows in 5a indicate first Al peak, overlapping O and Ca first peaks, and first Si and second Al peaks. (e-h) Prism oriented crystal is at the right of images, compositions 112, 313, 216, and 14535, respectively. Arrows in 5e indicate first O and Al peaks from the IGF adsorbed onto prism surface.

The most important feature observed in these density profiles at the (0001) interface is the presence of the small peak caused by adsorption of Al from the IGF onto the crystal. This peak location is appropriate for the layer of missing Al ions in the single Al termination of the (0001) plane of the crystal. Adsorption of such a second Al layer onto the (0001) surface would extend the crystal in the $<0001>$ direction. However, while this small Al peak indicated that there is some epitaxial adsorption of Al onto the crystal surface, there is no change in the height of this adsorbed Al peak, even with increasing concentrations of Al ions in the IGF (in the order 5d<5c<5b<5a). This indicates that growth of the basal plane in the direction of the surface normal is inhibited. This is consistent with experimental evidence that the growth of the basal plane in the <0001> direction is inhibited in the presence of calcia and silica in the IGF [16].

On the prism side of the IGF, figures III-5(e), (f), (g) and (h), the density profiles show that atoms in this interface are also ordered. The first peak from the atoms in the IGF is the O peak (marked by the arrow in 5e), creating the double layer O atom structure that is consistent with this orientation of the crystal since only one O layer from the crystal is present at the surface for the O-terminated $(11\bar{2}0)$ plane. Contrary to the first Al peak at the basal side, this O adsorption at the prism interface is very high. The next peak is Al adsorbed from the IGF onto the crystal (marked by the large arrow in 5e). Adsorption of these O and Al from the IGF is consistent with the growth of the crystal in this direction. Though this Al atom peak is less that it in the crystal, it obviously shows a much higher intensity than the average Al density in the IGF and the first IGF Al peak at the basal plane interface. It is also clear that at the $(11\bar{2}0)$/IGF interface, the first Al peak height is affected by the composition, increasing with increasing Al concentration in the

IGF (5e>5f>5g>5h). The relationships between the area of the first peak of Al adsorbed onto the crystal from the IGF and the Al concentration in the corresponding bulk glass are presented in Fig 6. Both the basal side and the prism side are shown in this figure. The area of the first peak of Al adsorbed onto the crystal from the IGF increases with increasing Al concentration in IGF at the prism side; however, it is nearly constant on the basal side regardless of Al concentration in the IGF (up to the maximum Al concentration in the 112 anorthite composition used here). This means the adsorption behavior of Al at the basal side is almost the same for all compositions. In addition, the location of the adsorbed Al peak on the prism side is slightly closer to the crystal than either the Si or Ca peaks. The density profile of the sum of the cations from the IGF adsorbed onto the prism surface in figure III-5(e-h) shows a fairly constant peak maximum ($\sim 8.0\times10^{22}$) for all compositions.

The most important feature of these simulations at the two interfaces is the different adsorption behavior and the implications with respect to crystal growth. The simulations show that growth of the (0001) plane in the <0001> direction is inhibited in the presence of the calcium alumino-silicate IGF. At the compositions studied here, the concentration of Al adsorbed onto the crystal from the IGF does not increase with increasing Al concentration in the IGF. However, growth of the $(11\bar{2}0)$ in the $<11\bar{2}0>$ direction appears possible with increasing concentrations of Al in the IGF. Anisotropic grain growth is observed experimentally, with growth in the <0001> direction being much slower than growth in the $<11\bar{2}0>$ direction in the presence of calcium alumino-silicate IGFs[16].

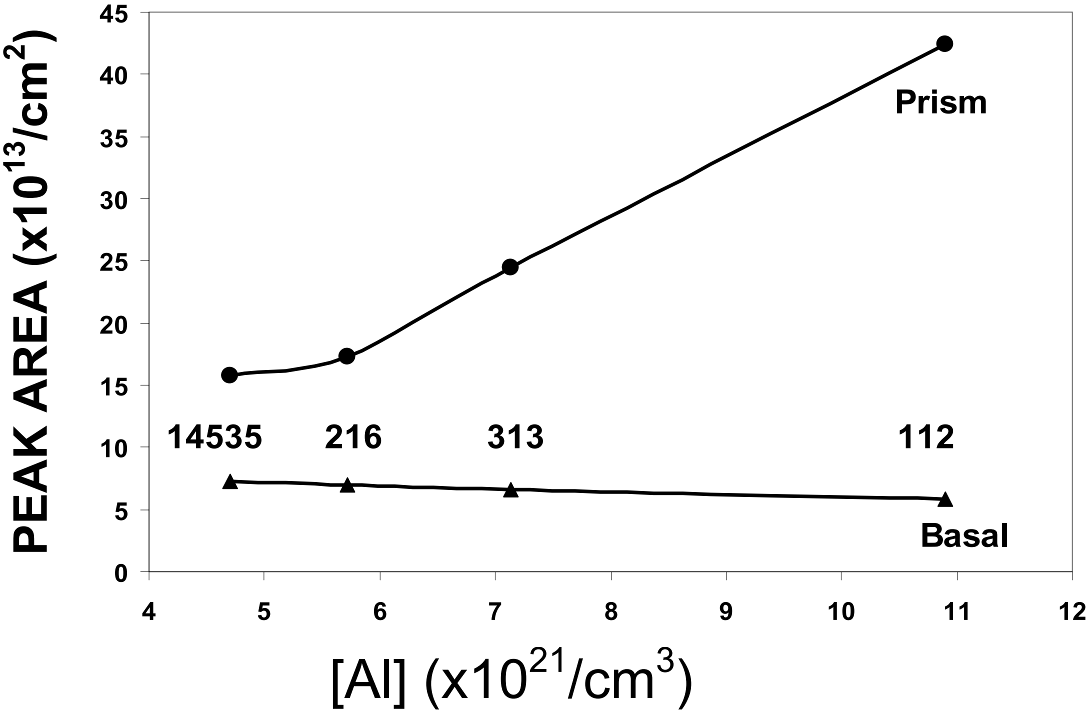

Fig.III-6 The relationship between the area of the first peak of Al from the IGF adsorbed onto the crystal and the Al concentration in the corresponding bulk glass that forms the IGF for the four systems. Both the basal and the prism sides are shown here.

III.3.2 Coordination Number Analysis

Because of the distinct coordination number (CN) in the crystal and the glass for both Al and O atoms, the CN change and the evolution at the interface regions can give some insights about the interface structures. In the crystal, the CN of Al is 6 and the CN of O is 4. For the glass compositions used in our study, the Al would enter the network with a CN of 4, consistent with experimental results of bulk glasses, as discussed previously[62]. In general, the O atom in glass would be either bridging oxygen (BO) whose CN is 2 to network-forming species, or non-bridging oxygen (NBO) whose CN is

1 (with a second bond to network modifiers such as alkali or alkaline earths). The CN of Si atoms is 4 in most bulk crystals and glasses.

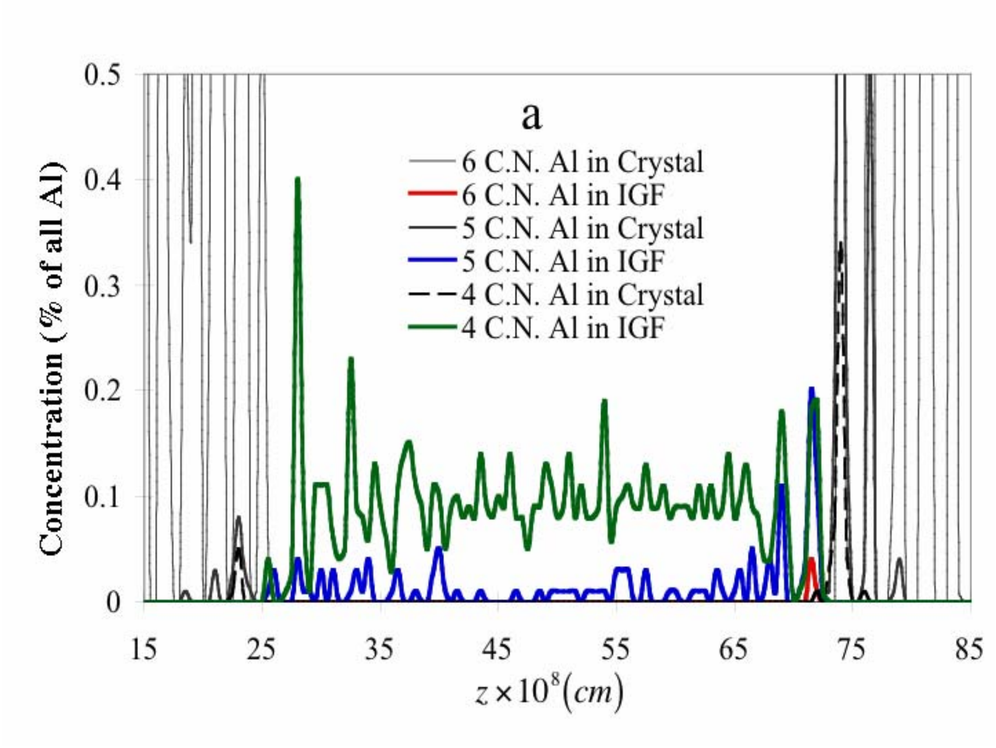

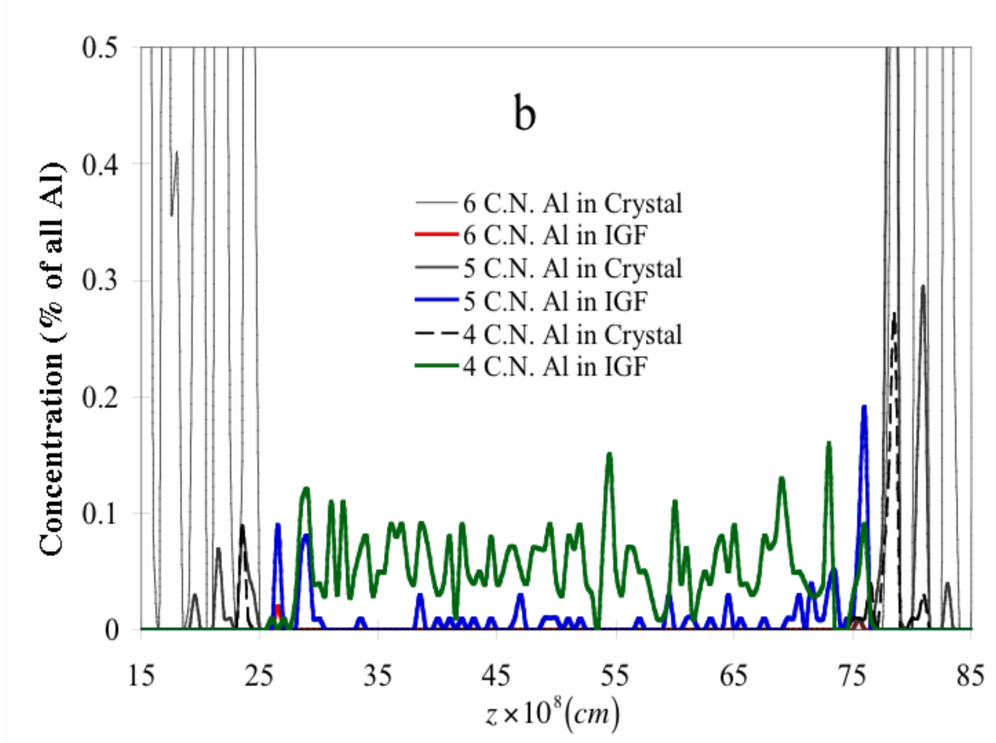

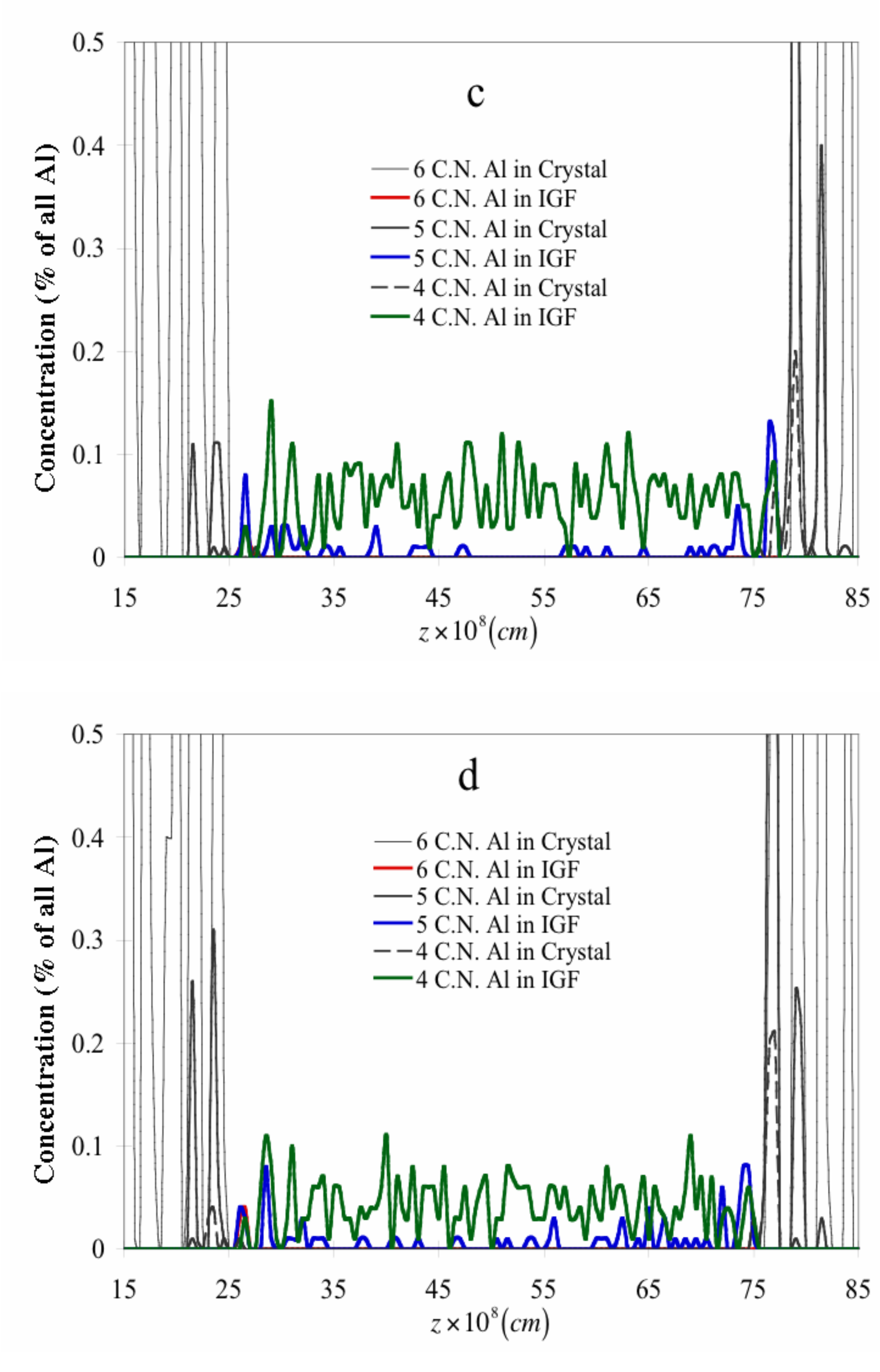

Fig. III-7 Coordination number (CN) profile of Al atoms along z direction (showing only the IGF and near interface region). (a) 112, (b) 313, (c) 216, (d) 14535 compositions.

Because of the unit cell periodicity of crystals, the structure parallel to the IGF/crystal interfaces (*x*, *y* plane) would be similar from unit cell to unit cell (as evidenced by the lateral similarity in each of figures III-2 and III-3 in one direction). However, structure parallel to the interface would be quite important in the case where we introduce point or ledge defects in the crystal surfaces. Since this is not the case here, only the CN profiles in the *z* direction perpendicular to the IGF/crystal interfaces are presented. Figure III-7 shows the CN profile of Al atoms along the *z* direction near the interfaces surrounding the IGF, again with the basal orientation at the left and the prism orientation at the right; (a) for the 112 system, (b) for 313 system, (c) for 216 system and (d) for 14535 system. The fraction of Al with a particular CN and the distribution along the z direction are shown in the figure. Al is predominantly 6-coordinated in the crystals, except near the interfaces. The 6-coordinated peaks of Al from the IGF are not the same in contact with the two crystals, as seen in the density profiles. There are 5-coordinated Al near and at the crystal surfaces because of the surface termination of the crystals. The 5-coordinated Al peak from the crystal at the prism side is especially high because of the loss of one layer of O on this crystal surface. Some Al atoms at the surface leave the crystal and enter the IGF, though the number is very small. Dissolution of the different crystal surfaces in the presence of the IGF would be influenced by the quench procedure used here. Nearly all Al in the interior of the IGF are 4-coordinated and only a very small number are 5-coordinated.

However, behavior is different at the two interface regions. Four and five CN Al predominate at the interfaces, with an increase in 5-CN Al with increasing Al in the IGF.

At the highest concentration of Al in the IGF (the 112 IGF), 6-CN Al form at the IGF/prism interface (figure III-7a). Because of the increasing adsorption of Al onto the prism surface with increasing Al concentration ion the IGF, this formation of 6-CN Al is indicative of Al from the IGF adsorbing on the prism surface in a crystalline structure consistent with growth of that crystal along the surface normal. In addition, there are more peaks of 5-CN Al in the IGF on the prism side extending into the IGF than on the basal side, again indicating a greater influence of crystal order consistent with the prism surface as compared to the basal surface.

The coordination number profiles for O atoms attached to Al or Si are shown in figure III-8, (a), (b), (c) and (d) for 112, 313, 216 and 14535 systems, respectively. Appropriately, 4-coordinated O atoms appeared in the crystals, though the peak shape is different due to the two orientations, and 3-coordinated O atoms are present at the crystal surfaces caused by the termination of the crystals.

Within the interior of the glassy IGF, the coordination of the O is predominantly 2-coordinated, indicating bridging oxygen (BO), as expected for these glasses. The concentration of non-bridging oxygen (NBO) varies, increasing with increased calcia concentration, also as expected. NBOs are present in the 112 CAS IGF, which is at the charge equivalence point of one Ca for two Al where it used to be assumed that no NBOs should be present based on stoichiometry. However, experimental data show that NBOs do exist at the equivalence point[83], so the simulation results are consistent with experiment. The other compositions have much larger NBO concentrations, as shown in figure III-8(b-d). There are, however, 3-CN O throughout the glassy IGF interior in the 112 IGF, with very few present in the other compositions. The presence of 3-CN O in the

112 glass is similar to the behavior observed in simulations of sodium alumino-silicate glasses[62]. In that previous work, a small percent (~3%) of O were 3 CN at the equivalence point of one Na per Al.

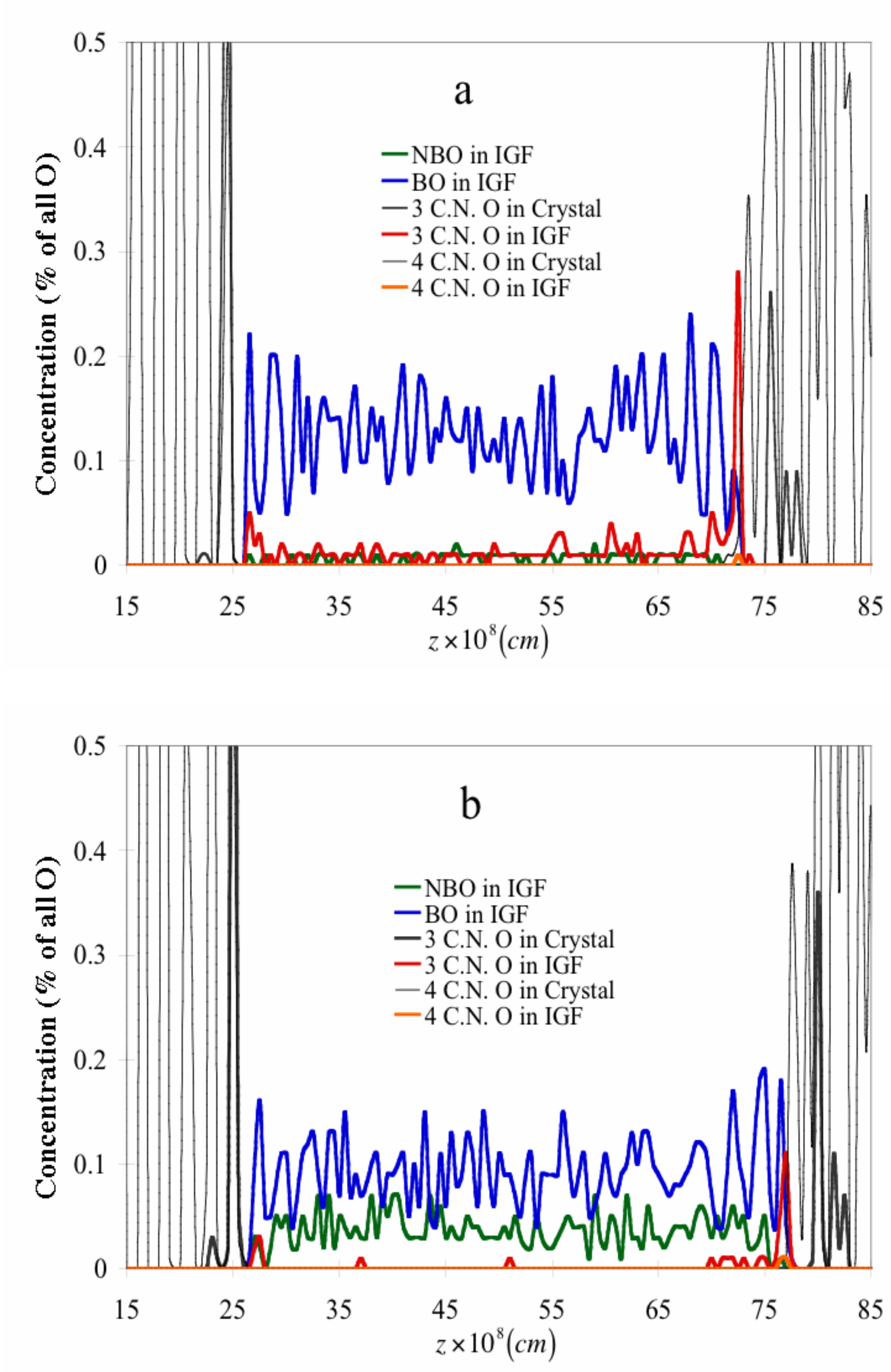

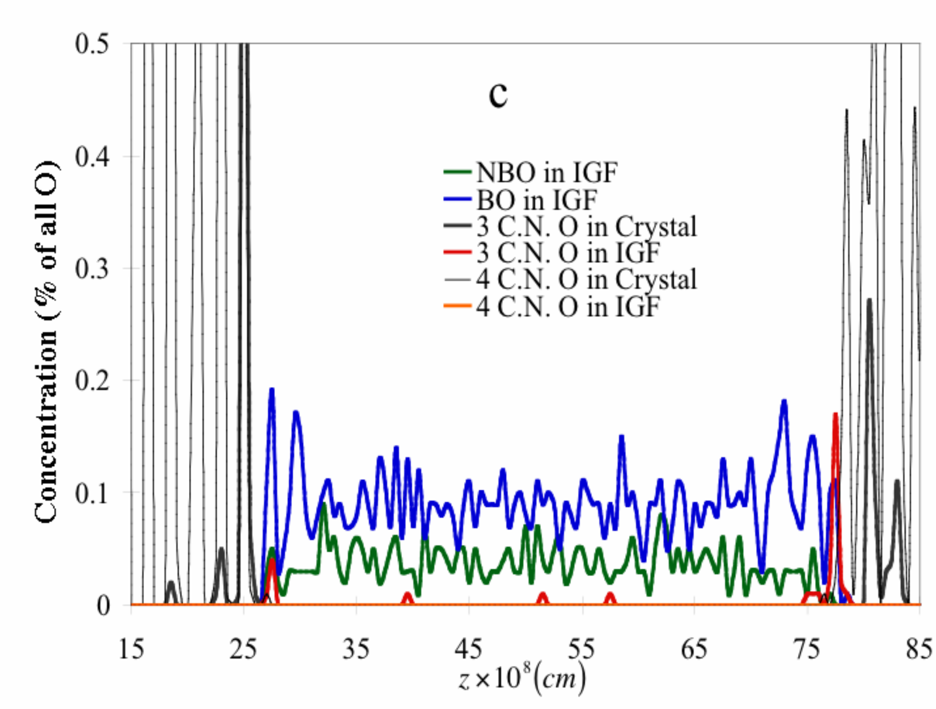

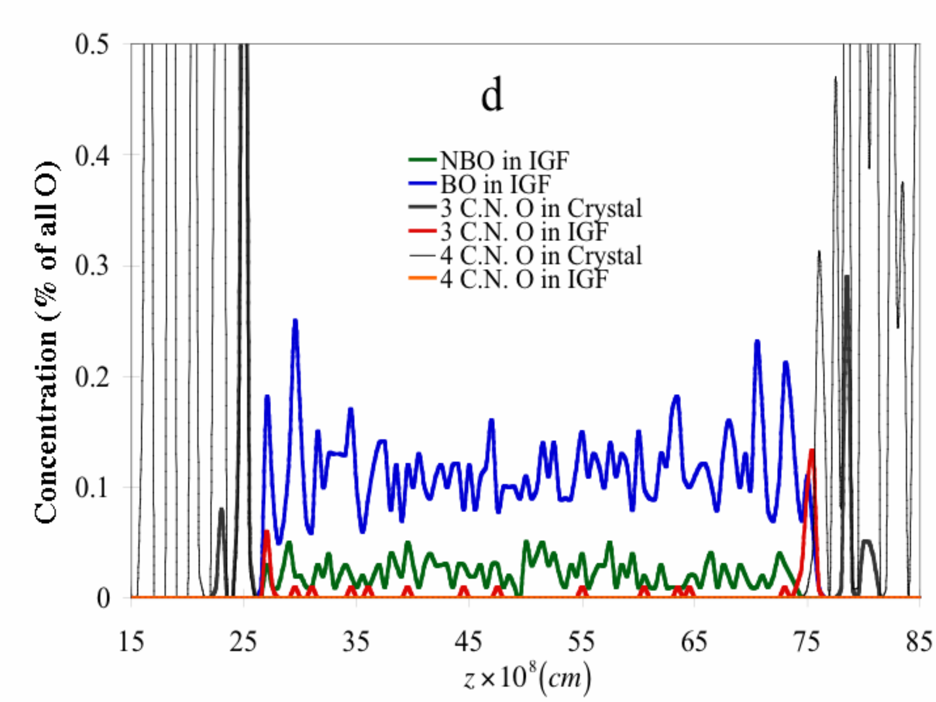

Fig. III-8 Coordination number (CN) profile of O atoms along z direction (showing only the IGF and the near interface region). (a) 112, (b) 313, (c) 216, (d) 14525 compositions.

Behavior at the interfaces is different than that within the glassy central portions of the IGFs and the coordination of O from the IGF (O_{IGF}) is different between the two interfaces. There is a slightly higher concentration of 3-CN O_{IGF} at the basal interface in comparison to the interior of the IGF at all compositions. However, the concentration of 3-CN O_{IGF} is much higher at the prism interface that the basal interface or the interior of the IGF. Figure III-9 shows the area of the first peak for 3-CN O_{IGF} adsorbed onto the prism and basal surfaces as a function of Al/Ca ratio, showing the significant difference between these interfaces. Even at the lower Al concentrations, 3CN O are more than 3 times more likely to form on the prism versus the basal interfaces.

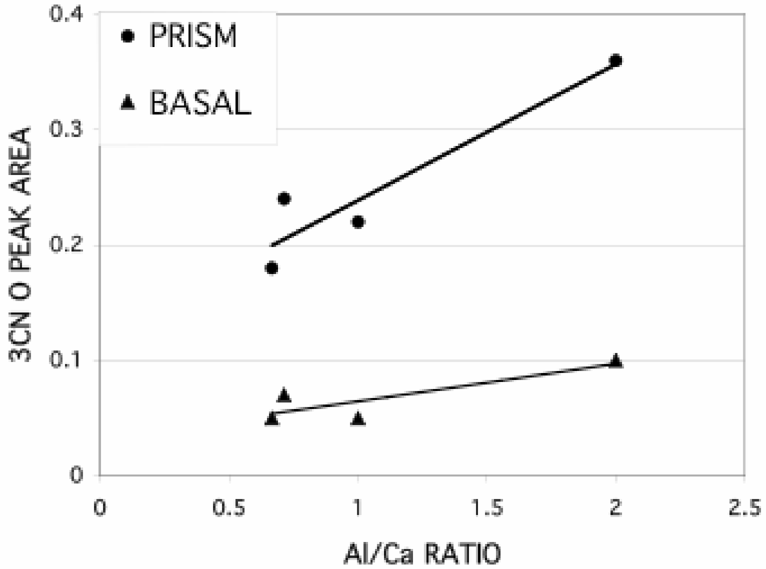

Fig. III-9. Area of the first peak of 3 coordinated O adsorbed onto prism and basal planes as a function of the Al/Ca ratio in the IGF.

In the 112 IGF, there are even 4-CN O_{IGF} forming at the prism interface, consistent with extension of the crystal in this direction. Thus, both the Al and the O adsorbed onto the prism surface show the higher coordination numbers consistent with that of the crystals.

In summary, the simulations show preferential adsorption of Al and O on the prism plane (and implied growth) with increasing Al concentration in the IGF, with no such behavior on the basal plane. The role of Ca and Si on Al adsorption on the basal plane has been previously discussed[75]. The new information presented here implies potential growth on the prism plane with increasing alumina concentration in the silicate IGF. The competition of the cations for adsorption sites onto the crystal surfaces is affected differently by the different surface terminations on the basal and prism surfaces. The apparently rapid adsorption of O onto the Al terminated basal surface initiates a ‘cage’ structure that inhibits Al (and Si) adsorption into the resultant cages because of the induced strain around these cations (octahedral and tetrahedral coordinations of the Al and Si become too strained within the center of the ‘cage’ and are less stable, hence Ca adsorbs there). The O adsorbed onto the O terminated prism plane (completing the double O layer in this orientation) bond to 2 Al atoms in the crystal surface. Such an adsorbed O can bond to a third cation that would come from the IGF cations, Si, Al, or Ca. Si is less likely to attach to this O because 3 coordinated O attached to 2 Al and 1 Si is less stable than a 3 coordinated O attached to 3 Al at high alumina concentrations[62]. The O adsorbed onto the crystal are locally in a region of very high Al concentration, with all Al on one side from the crystal and additional Al from the IGF. The left side of figure III-3 shows a couple of adsorbed Al attached to adsorbed O (on the IGF side of the dashed line) that are 3 coordinated to 3 Al atoms. The adsorbed Si are attached mainly to 2 coordinated O (although there is a Si attached onto a 3 coordinated O). While Ca adsorption is possible on the adsorbed 3 coordinated O, its binding energy is less than either the Si or the Al at this site and therefore is also less likely to occur.

III.4 Conclusions

The structure of crystal/IGF/crystal systems using the α-alumina (0001) basal plane and $(11\bar{2}0)$ prism plane in contact with several different calcium alumino-silicate (CAS) glassy IGFs was studied using molecular dynamics simulations. The density profiles of the atoms showed ordering at the IGF/crystal interfaces induced by the crystals and extending ~1-1.5nm into the glassy IGFs. Details of the specific species adsorbed at the interfaces and the coordination number of Al and O atoms at the interfaces indicate a significant difference in adsorption behavior at (0001)/IGF versus the $(11\bar{2}0)$/IGF interfaces. At the compositions in the IGF used here, the presence of Ca and Si in the IGF inhibits epitaxial adsorption of Al onto the (0001) surface, thus inhibiting growth of the basal plane along the surface normal (<0001> direction). The current concentration change of Al in the IGFs does not affect the segregation of Al from the IGF to the surface of the (0001) basal plane. On the $(11\bar{2}0)$ surface, preferential adsorption of O and Al atoms from the IGF onto this plane occurs in the simulations, with more Al adsorption occurring with increased Al concentration in the IGF. Such behavior is consistent with the growth of this crystal in the $<11\bar{2}0>$ direction. The presence of Ca in the IGF affects behavior at the basal plane, but does not do so at the prism plane. The different adsorption behavior is caused by the formation of specific bonds between IGF species and surface species that limit further adsorption. These simulation results are indicative of preferential growth that is consistent with the anisotropic growth of alumina crystals containing calcium alumino-silicate IGFs that has been observed experimentally.

IV. Molecular Dynamics Simulation of Calcium Diffusion in the Calcium Alumino-Silicate Intergranular Films Between Different Alumina Grains

IV.1 Introduction

IGFs form in many commercial ceramics, either because of impurities or because of the addition of sintering aids. IGFs play an important role in the properties of the material[84-88]. IGFs also affect morphology of the material, such as abnormal grain growth (AGG)[16, 28, 89], although the precise details are still being determined because of the experimental difficulties of understanding the structure of the amorphous thin (~nm) IGFs. Calcia and silica are well known impurities that form IGFs and significantly affect AGG, even in the ppm range[16, 43, 90]. The role of the distribution of impurities at the grain boundaries can have an effect on IGF formation as well as AGG[40]. While thermodynamics governs the resultant compositions of the silicate IGFs, a question arises as to whether bulk thermodynamics dominate in such thin films. In addition, understanding the kinetic properties that govern the migration of ions between the pockets or triple points (TPs) present in the ceramics to the two-grain junctions, forming the IGFs, as well as the dissolution and precipitation of alumina from different crystalline surface planes into and out of the IGF is important. These kinetic features are even more difficult to determine experimentally at IGFs and TPs than are the structural data, but may nonetheless be extremely important with respect to the details of grain growth and AGG and the evolution to thermodynamic equilibrium. In addition, pre-empting thermodynamics via intelligent processing (kinetics) may be an important approach to the design of new materials. Therefore, understanding the kinetic details of behavior in systems containing IGFs will be useful beyond the obvious benefits.

There have been a large number of studies of liquids in confined pores where ordering at the interface is observed[91-95]. Such studies are usually related to inert gas adsorption or non-reactive water confinement and there are fewer studies involving confinement of reactive species. Studies of chemically reactive IGFs in alumina crystals and silicon nitride crystals have shown ordering of the IGF ions at the IGF/crystal interfaces induced by and dependent upon the crystal surface structure [69, 70, 73, 75, 96-99]. Such work shows the importance of the details of the atomistic crystal surface structure on interface structure.

Diffusion of ions in glasses has been well studied and experimental data on the diffusion of network modifiers, such as Ca or Na, exist[100-109]. There are also similarly oriented computational studies of diffusion in bulk glasses[62, 81, 110, 111]. There are many experimental and computation studies of the diffusion and migration behavior of the species in confined liquids[112-114]. Such results showed that diffusion is lessened due to structural effects[113, 115]. Some of them show that the diffusion is sensitive to the stress or pressure changes[115]. Diffusion behavior is found to be anisotropic and structure sensitive when the species are confined between two solid surfaces[115, 116]. There have not been studies of diffusion of network modifier ions in the oxide IGFs between ceramic crystals. Based on studies of the behavior of molecules in confined structures, it might be anticipated that diffusion of network modifiers in IGFs may be different from that in bulk glasses. While diffusion heterogeneity might be expected for ions within the IGF, the details of such behavior are not known, especially with respect to comparison to the bulk glass behavior. As such, the work performed here is designed to provide atomistic level information regarding the kinetic behavior of Ca ions in silicate

IGFs that are present in alumina ceramics. Such behavior is evaluated at the IGF/crystal interfaces of differently oriented alumina crystals, as well as within the more glassy portion of the IGF.

IV.2 Computational Procedure

In the current study of Ca diffusion in IGFs between alumina crystals, four CAS IGF compositions between basal and prism oriented alumina crystals previously used to study the structure of the IGF[96, 117] were used here. As described elsewhere[96], the IGF between the alumina crystals was created by the melt-quench process as described in the former section. This number of IGF ions was designed to generate an IGF of ~4nm and was not intended to determine the thermodynamic equilibrium thickness and composition. Rather, these simulations were done assuming different compositions and reasonable thickness for the IGF.

In the current simulations, these final structures[96] were used to continue the simulations to study calcium diffusion in IGFs. In addition, Ca diffusion in the bulk CAS glasses with the same compositions as those used in the IGFs was studied as a baseline to determine the difference between Ca diffusion in bulk glasses and that in thin IGFs between crystals. Ca diffusion was simulated at several high temperatures for both the bulk glasses alone and the IGF/crystal systems. NVT ensemble and 3-dimensional periodic boundary conditions were applied. The atoms in a thin volume (~6Å in Z) farthest from the IGF in each crystal are kept frozen (do not respond to the interatomic forces) at all temperatures in the IGF/crystal simulations. Freezing these ions enabled use of 3-dimensional PBC without the crystals seeing each other in the Z dimension across the Z direction periodic boundary.

Two approaches were used in these simulations of the IGF/crystal systems. In one, all atoms in the crystals were frozen so that high temperatures could be used and crystal surface melting would be avoided. However, because of the effects of the frozen crystal surface on nearby Ca diffusion, additional runs were performed at lower temperatures of 2700K and 3000K where the atoms in the crystal surfaces were allowed to move in response to the interatomic forces, providing for more realistic simulations. The crystal surfaces did not melt at these two lower temperatures. The starting structures were heated from 300K to a specific temperature with velocity rescaling for the first 10 ps of the 100ps runs. A time step of 0.5 fs was used in the simulation and the configurations were saved every 0.25 ps, for a total of 400 configurations.

Self-diffusion data of calcium were collected over the final 90 ps. The mean square displacement, $\overline{r_\tau^2}$, given as $<(r(\tau)-r(t_0))^2>$, was averaged over 160 initial configurations, t_0, each separated by 0.25 ps, and $\tau = t_0 + \Delta t$. Δt was taken for all subsequent configurations up to a total of 50 ps from each t_0. This was done for each atom type, although the temperatures that were used were low for any significant (diffusive) displacement of Si, Al or O ions (except at 5500K for Al and O)), allowing only Ca diffusion that is somewhat different from diffusion in the liquid state of the oxide. The diffusion coefficient, D, was then calculated from the slope of $\overline{r_\tau^2}$ as a function of elapsed time using

$$D = \frac{1}{2\alpha}\left(\frac{d}{d\tau}\overline{r_\tau^2}\right) \tag{IV.1}$$

where α represents the dimensionality of the diffusion.

Diffusion constants were calculated for Ca ions in each of the bulk glasses and the IGF/crystal systems. In the latter, diffusion constants were calculated for ions within particular volumes associated with (a) the IGF/basal plane interface, (b) the IGF/prism plane interface, and (c) the interior of the glassy IGF. The $\overline{r_\tau^2}$ of each ion of a particular type was summed together only while the ion was within the volume of interest. The basal and prism interface volume extend ~ 0.5 nm from the crystal surface into the IGF so that only the ordered structure of the IGF contacting each crystal is included. Since the three volumes of the IGF that we define here have a boundary with the rest of the IGF, Ca ions close to a boundary may frequently fluctuate across it. The short time behavior of such atoms that only vibrate across the boundary is excluded in order to get the longer time self-diffusion data of the Ca ions that stayed within the selected volume. However, a Ca atom that diffuses across a boundary and stays for some time is included in $\overline{r_\tau^2}$.

The activation energy of self-diffusion, Q, was calculated using regression analysis of D as a function of reciprocal temperature from an Arrhenius plot,

$$D = D_0 \exp\left(\frac{-Q}{RT}\right) \tag{IV.2}$$

where D_0 is the pre-exponential factor and R is the gas constant.

IV.3 Results and Discussions

IV3.1. Bulk Glass Diffusion

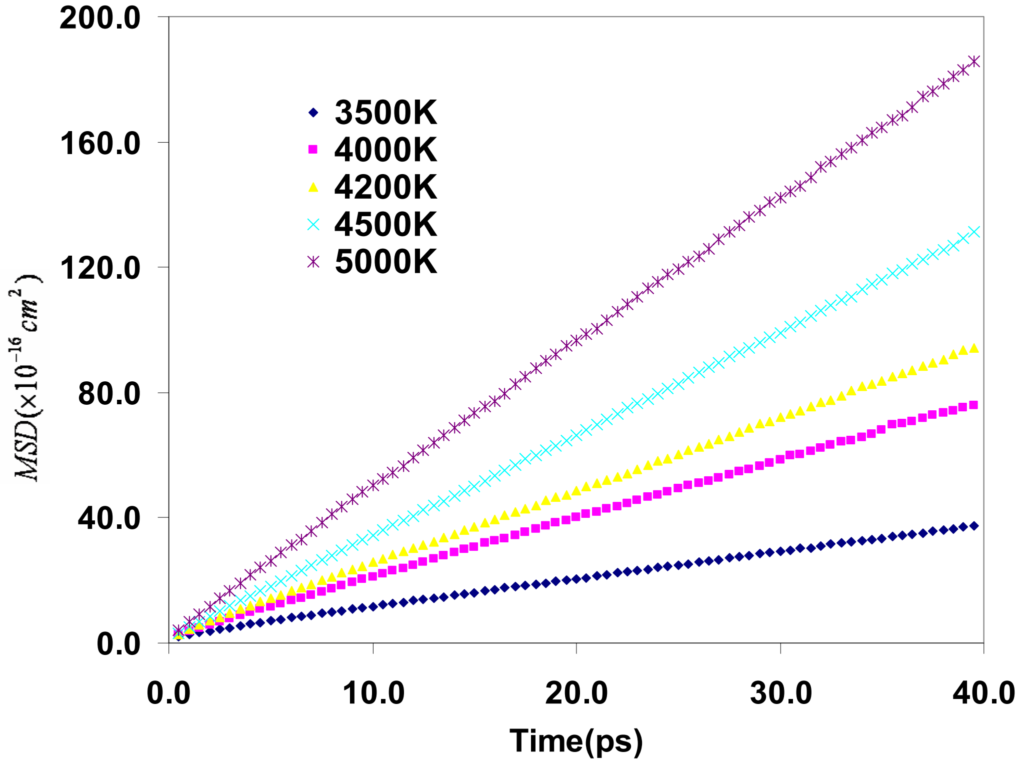

Fig. IV-1. Mean square displacement (MSD) of Ca in bulk calcium alumino-silicate 112 glass.

The mean square displacement (MSD) curves of Ca in the bulk 112 CAS glass at several temperatures are shown in figure IV-1. The diffusion coefficient at each temperature was calculated from the slope of the curve at that temperature. The Ca self-diffusion activation energy, Q, in bulk 112 glass was obtained from using equation (IV.2). The other three bulk glasses have similar diffusion curves and are not shown here for simplicity. The calcium diffusion coefficients and activation energies of four bulk glasses are shown in Table IV-1.

Table IV-1. Calcium self-diffusion coefficients

	Self-diffusion coefficient ($\times 10^{-10}$ m^2/s)			
	313	**112**	**14535**	**216**
Bulk Glass				
3500K	16.7	14.8	12.4	11.6
4000K	33.2	31.2	25.7	25.0
4200K	39.2	38.7	34.8	32.0
4500K	53.8	54.3	48.3	43.3
5000K	77.2	77.0	70.0	69.3
ΔQ(kJ/mol)	149	170	171	173
Interior of IGF				
3500K	20.2	16.4	10.8	9.12
4000K	35.8	30.8	24.8	18.0
4500K	58.7	53.5	39.7	30.8
5000K	80.5	84.2	61.7	51.8
ΔQ(kJ/mol)	136	159	167	167
Basal Interface with frozen crystal surface				
3500K	1.11	1.83	1.06	1.07
4000K	2.78	4.70	2.28	2.23
4500K	4.63	7.2	5.68	4.22
5000K	7.50	14.5	12.1	12.3
5500K	14.5	22.7	18.5	19.2
ΔQ(kJ/mol)	198	189	237	237
Prism interface with frozen crystal surface				
3500K	2.38	0.044	1.21	0.735
4000K	4.13	0.442	3.33	1.72
4500K	5.93	2.18	5.25	4.22
5000K	17.5	4.78	11.9	8.17
5500K	23.8	8.73	17.3	13.4
ΔQ(kJ/mol)	161	431	213	240
Basal interface with free crystal surface				
2700K	0.637	1.54	0.328	0.520
3000K	2.13	2.47	0.775	0.625
ΔQ(kJ/mol)	---	---	---	---
Prism interface with free crystal surface				
2700K	0.388	0.217	0.120	0.375
3000K	0.710	0.282	0.218	0.393
ΔQ(kJ/mol)	---	---	---	---

IV.3.2. Ca Diffusion at the Interfaces and in the Interior of the IGF Glasses

IV.3.2.1 Ca diffusion with frozen crystals

The diffusion curves of the 313 system are shown in figure IV-2, where (a), (b) and (c) presents Ca diffusion in the volume at the IGF/basal interface, the interior of IGF, and at the IGF/prism interface, respectively.

The interior of IGF remains amorphous, similar to the bulk glass, while the other two interfaces have some ordered structures induced by the crystals (see figure III-2 and figure III-2). Diffusion coefficients of the four IGF systems at four different high temperatures are listed in Table IV-1. The diffusion coefficient of Ca in the interior IGF of 313 and 112 IGF system is a little higher than that in the corresponding bulk glass, but in 14535 and 216 IGF system it is slightly lower. The activation energy for Ca diffusion in the interior IGF is slightly lower for all IGF systems compared to that in bulk glasses, although the trends are similar in each.

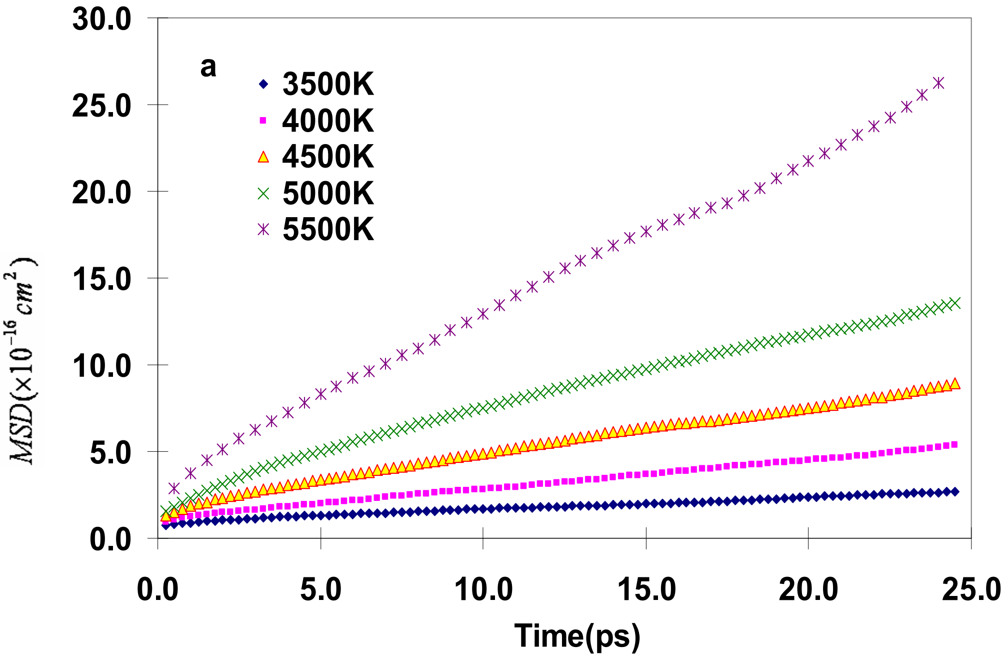

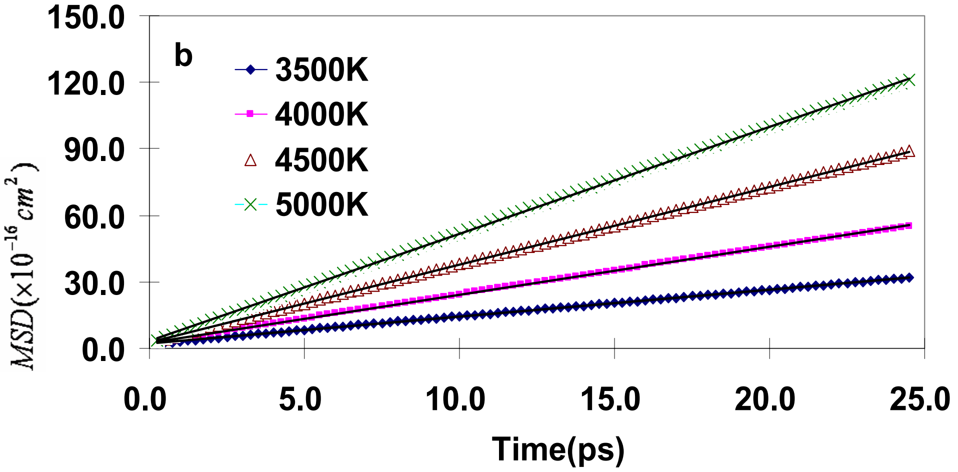

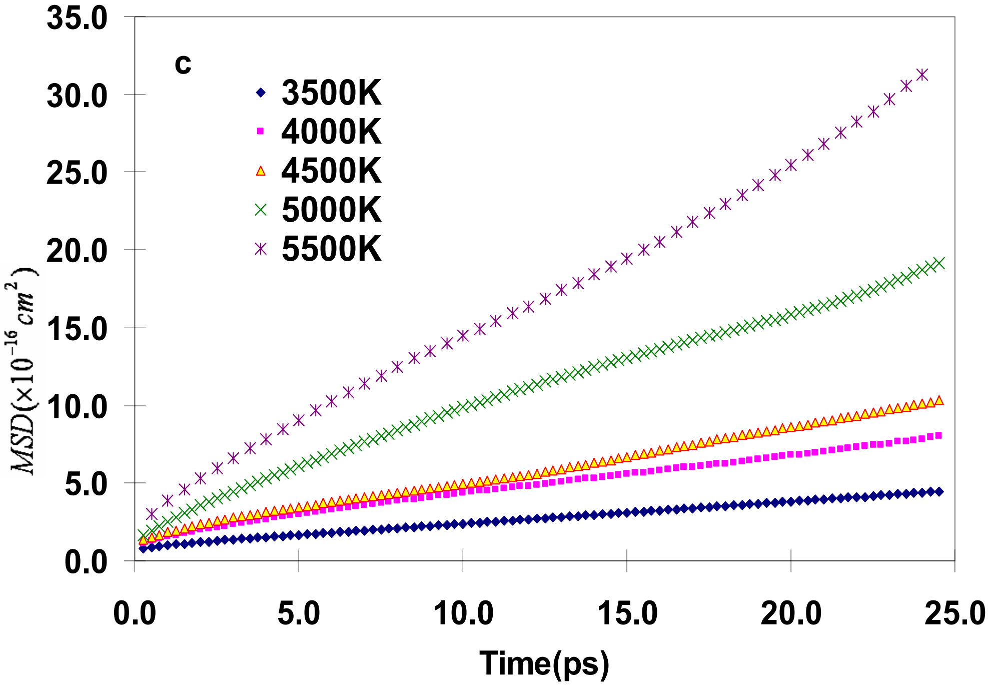

Fig. IV-2. Ca diffusion for the 313 intergranular film (IGF) system at different temperatures: (a) Ca at the basal interface, (b) Ca in the interior of the IGF, (c) Ca near the prism interface.

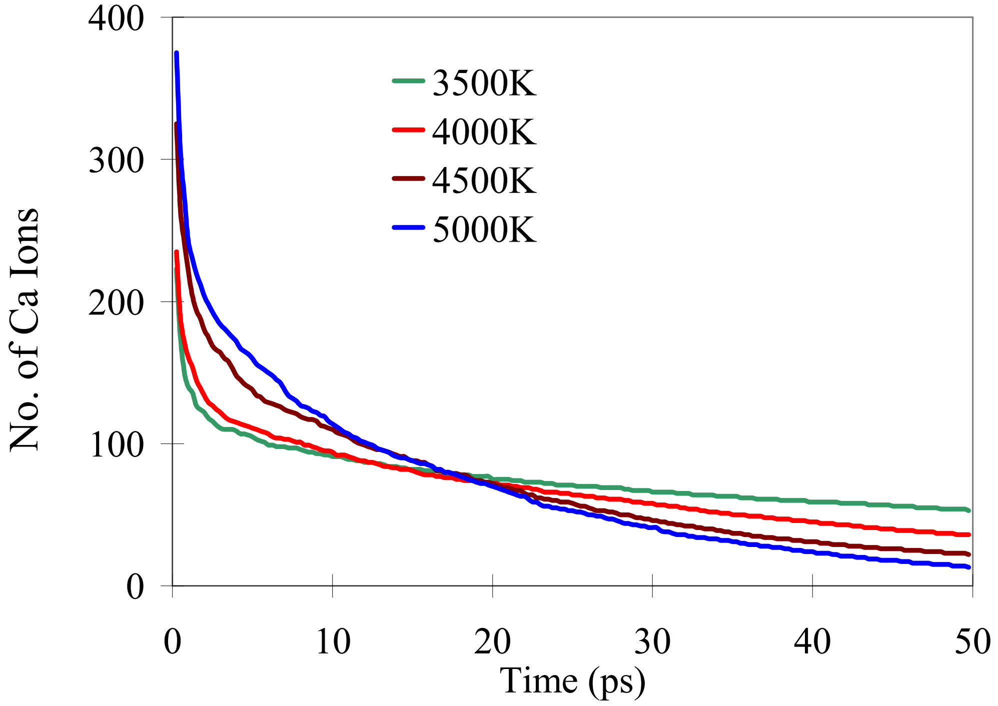

Fig. IV-3 The number of Ca ions in the volume near the 112 basal interface as a function of time from each initial t_0.

Ca diffusion in the two thin interface regions adjacent to the frozen crystal surfaces is lower than that in the bulk CAS glasses and in the interior of the IGFs and the activation energies are higher. Ca moves slowest in these interfaces and those Ca closest to the alumina crystal surface stay in the interface for a long time. Figure IV-3 shows the number of Ca atoms within the volume near the basal interface as a function of time from each initial time t_0. Ca ions at the boundary of the interface region with the interior of the IGF that frequently vibrate in and out of the region are multiply counted in figure IV-3, but not in the MSD data, and contribute to the large number of Ca at the shortest time in the figure. The number of Ca ions fluctuating across the boundary increases with increasing temperature, as seen in figure IV-3. Increasing temperature also make the number of atoms that remain within the interface volume for long periods of time to decrease more than that at lower temperatures. This is caused by the increased diffusion of the Ca ions out of the interface volume at higher temperature. Conversely, that also means that more Ca ions in the IGF interior can diffuse into the interface region at the higher temperature. However, since these ions enter the interface region after some time spent in the interior, their time within the interface region is lessened, thus contributing to the higher number of Ca at times less than ~19ps at higher temperature.

Figure IV-4 gives the MSD vs time of the basal interface of 313 IGF system for several temperatures. Though in the current study, the basal and prism interface volumes have a small z dimension value (~0.5nm) compared to the interior IGF region and bulk glass, the movement of Ca is not limited to 2-D in such thin layers. For consistency, the dimensional term (α) in equation 6 used to calculate all diffusion coefficients was 3.

Ca diffusion data for the interface regions are also in Table IV-1. As mentioned above, the activation energies for Ca diffusion in the interface regions are higher than that the interior of the IGF. The activation energies are fairly similar at the basal and prism interface regions for the 216 and 14535 systems, but show quite different behavior for the 112 and 313 systems. In the high Al IGF (112 system), there is a very significant increase in the activation energy for Ca diffusion at the prism side. This increase coincides with the significant adsorption of Al from the IGF onto the prism surface, indicating onset of growth of the prism plane along its surface normal[96].

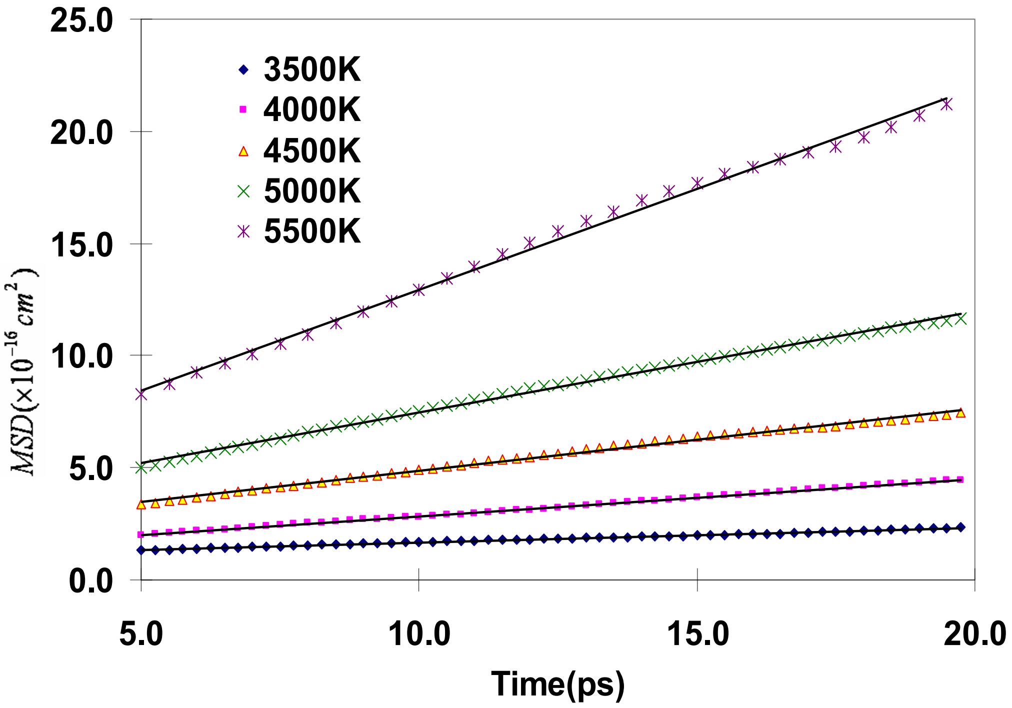

Fig. IV-4. The mean square displacement (MSD)versus time in the 313 intergranular film system for Ca ions in the volume adjacent to the basal interface.

In addition, the diffusion coefficients in the two ordered interface regions are much less than that in the interior of the IGF, although this could be influenced by the frozen nature of the crystal surfaces.

IV.3.2.2 Ca diffusion near the basal and prism interfaces with free crystal surfaces

Of course, the use of frozen atoms in the crystals could affect the diffusion of Ca ions near the interfaces. To evaluate this effect, without allowing for dissolution of the crystals, two additional sets of simulation were performed at temperatures (2700K, 3000K) where Ca diffusion could still occur, but where the crystal surfaces are stable in contact with these IGFs and crystal atoms mainly vibrate in their lattice positions.

In the interior of the IGF, Ca diffuses similar to that in the interior of the frozen crystal case, showing that the status of the crystal (frozen or mobile atoms) did not significantly affect diffusion in the interior of the IGF. Figure IV-5 shows Ca diffusion at the basal and prism sides for 2 systems at 2700K and 3000K. Similar to the frozen crystal cases, Ca diffusion decreases significantly in the two thin interface regions in comparison to that in the interior of the IGF, again with MSD near the basal interface being greater than that near the prism interface for all compositions.

There is a slight increase in the MSD of Ca at the interfaces of the mobile crystal surfaces in comparison at the frozen crystal cases, even though the temperatures are lower than the frozen crystal cases. The vibrational amplitude of the crystal atoms in the surface allows for an enhancement of Ca diffusion near the interface, although the overall trends are not altered with respect to the frozen crystal cases and the diffusion of Ca is still much lower at the interfaces than that in the interior of IGF.

In addition to Ca diffusion in 3 dimensions, we also calculated Ca MSD at the interface in the XY plane (parallel to interface) and in the Z plane (perpendicular to interface). As expected, since z is only 0.5 nm for the calculation of Ca diffusion in the interface regions, diffusion in this direction is highly limited before the ion is out of the interface volume. The Ca diffusion in the XY plane in the interface regions made up most of the diffusion behavior. Even if Ca diffusion was calculated in equation 6 using an $\alpha=2$ versus the 3 dimensional value of 3, the diffusion coefficients of Ca in the interface regions would only be 1.5 times higher than the data shown in Table IV-1, which is still much lower that diffusion in the IGF interior.

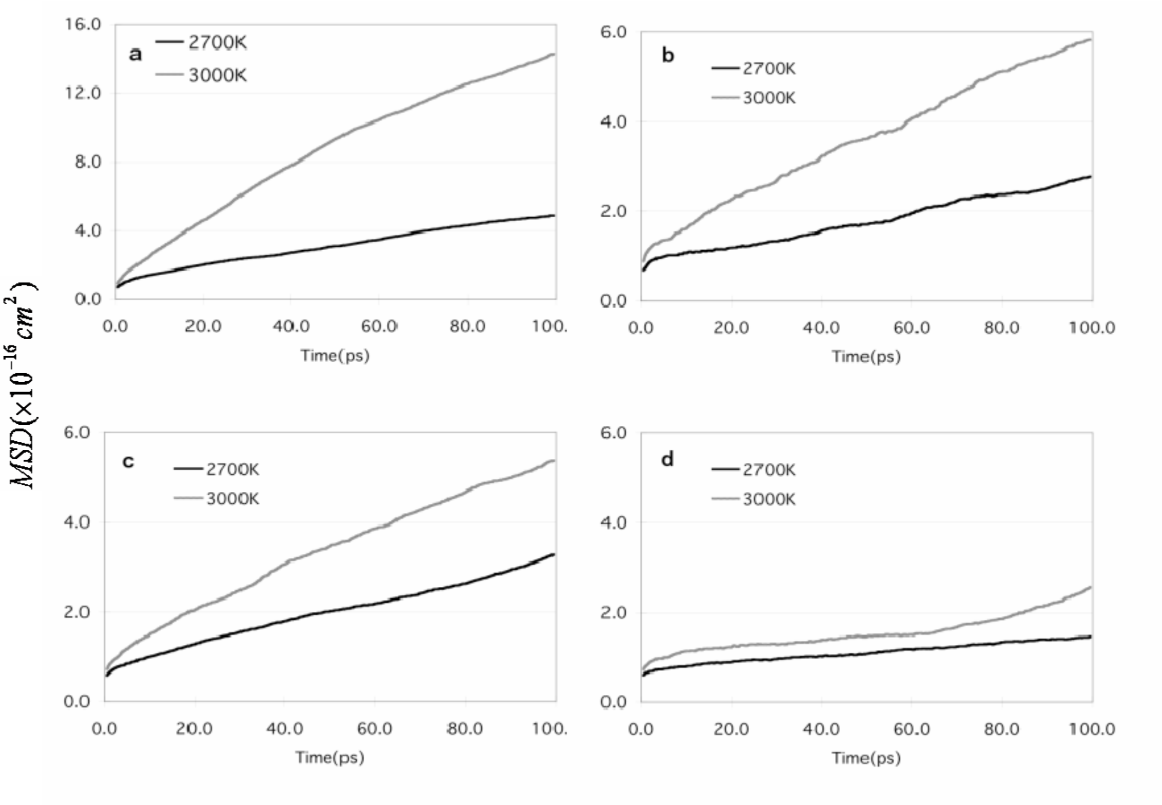

Fig. IV-5. Ca MSD at the basal side(a, b) and prism side (c, d) with free crystal surface for the 313 (a, c) and 14535 (b, d) systems. Note the difference in the y-axis units in (a) in comparison to others

IV.3.3 Discussion

The calculated activation energies of Ca diffusion in three of the bulk glasses is ~170 kJ/mole, which is consistent with experimental and other simulation results[103, 118-121]. *Of course, the experimental data are collected at lower temperatures and much longer times than that done in MD simulations.* In a previous study of Ca diffusion in glass at the anorthite composition, the authors comment on the range of activation energies being in the 170-190 kJ/mole range [119]. Data from molten *calcium silicate glasses (36.6% CaO, 1500°C-1650°C)* put the value near 100kJ/mole [122]. Since our calculations are done at temperatures where the network species are not diffusing, data from molten silicates should be lower. Other experimental studies of Ca in the multicomponent oxides albite and jadeite put the activation energies for Ca diffusion between 150 and 160 kJ/mole [120] *in temperature ranges from 800°C to 1050°C for long times.* The 313 glass has a lower activation energy than the other glasses, which would be anticipated because of the much higher Ca concentration in this glass. This trend is carried through to the activation energies for Ca diffusion in the interior of the IGFs. The pre-exponential is nearly the same for all compositions, except for Ca diffusion near the basal surface of the 112 system, where it is lower than the others. The 313 glass has a much higher ratio of Ca to all cations, which affects the glass structure, creating more non-bridging oxygens (NBOs) than the other glasses. The effect of the ratios of modifier ions to network formers, especially +3 ions in the network (like Al) has been discussed with respect to ion diffusion[62, 81, 121]and is expected to be relevant here.

The structure of the interior of the IGF between (0001) basal and $(11\bar{2}0)$ prism alumina grains is similar to that of the bulk glass, although there are clearly differences. This is seen in figure IV-6 for the radial distribution functions (RDFs) for the 112 and 313 glasses. These two systems show the least (a) and the most (b) differences between the IGF interior and the bulk glass structures of the four systems. The main differences in each comparison are due to the shoulder in the first peak caused by the Al-O bonds in both systems and the longer distance Ca-O and O-O interaction distances in (b). Unlike the regions close to the crystal surface, the interiors of the IGFs show no ordered distributions of species.

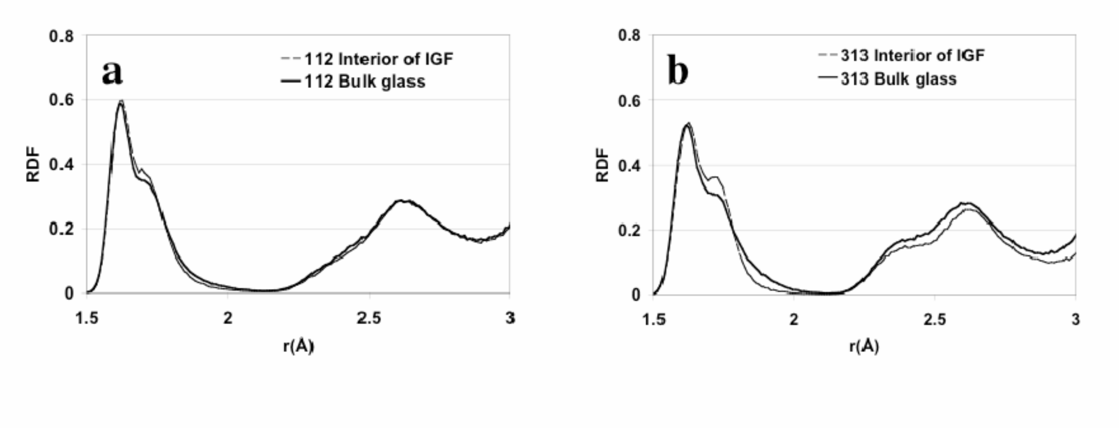

Fig. IV-6. Radial distribution functions (RDFs) of the interior of the intergranular film (IGF) (exclude the interfaces) and the bulk glass for the (a) 112 and (b) 313 compositions. (a) shows the smallest structure differences and (b) shows the largest difference of the four compositions studied.

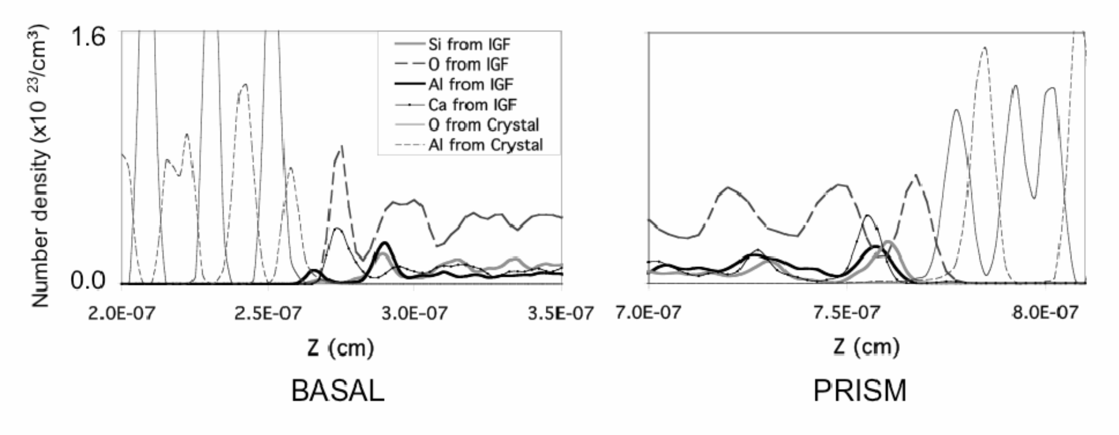

Fig. IV-7. Density profile of individual species at the interfaces of 313 system showing ordering near the interfaces caused by the presence of the crystals. Crystal on the left in the BASAL image and on the right PRISM image. Labels given in the inset on BASAL image.

The ordered structures at the basal and prism interface side greatly decrease the Ca diffusion coefficients and increase the activation energies of diffusion in comparison to values in the bulk glass and IGF interior. These can be explained by the structural differences at the two ordered interfaces. At the basal side, ordered “cage structures” are found between the IGF and the (0001) basal alumina crystal as shown in figure III-2. These “cages” readily accommodate the Ca atoms, which has been previously discussed[70, 75, 96]. The density profile of the 313 IGF at the basal side is shown in the plot on the left side of figure IV-7 (taken from last section), with the Al-terminated crystal on the left and the IGF on the right. The presence of Ca ions in the IGF restricts adsorption of Al from the IGF onto this crystal surface, thus preventing growth of the crystal along the surface normal[96]. This is seen by the very small amount of Al atoms adsorbed as the next layer onto this crystal termination (figure IV-7). Increasing concentrations of Al in the IGF (at the concentrations used here) did not alter this Al peak at the basal interface[96]. At the prism interface in figure IV-7, O adsorb, forming the second O layer, consistent with growth of the $(11\bar{2}0)$ plane along its surface normal[96], followed by cation adsorption (see figure IV-7, right side, where the crystal is on the right in the prism graph and the IGF is on the left). At both the basal and prism interfaces, the high Ca concentration in the 313 system causes a large Ca peak at each interface.

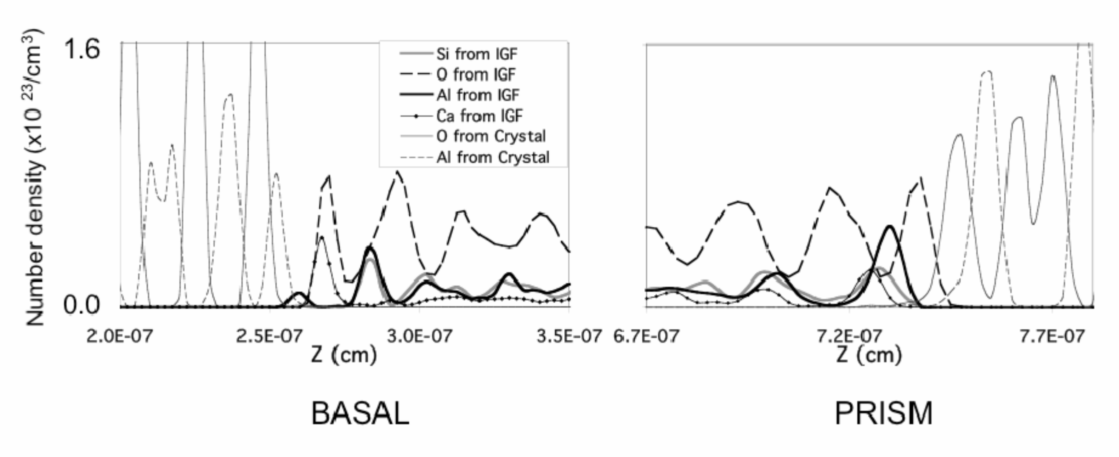

Fig. IV-8. Density profile of individual species at the interfaces of the 112 system showing no change in the first Al peak adsorbed onto the basal side in comparison to the 313 system in Fig. IV-7, but a significant increase in that on the prism side. Labels given in inset on BASAL image.

Increasing the Al concentration in the IGF (112 system) causes significant Al adsorption at the prism surface, with no change in adsorption behavior at the basal side (figure IV-8) [96]. With higher Al (and O) adsorption onto the prism side, there is an extension of the crystal structure along the surface normal. The adsorption of the first O peak from the IGF onto the prism surface, creating the appropriate two O layers in this crystal orientation (one from the crystal termination, the other from the adsorbed O), followed by the increased Al adsorption peak, followed by another O layer which shows potential splitting into the two O layers of the crystal, indicates growth of the prism plane[96]. The activation energy for Ca diffusion near the prism interface increases dramatically in comparison to all other regions because of these Ca ions caught within these growing crystal layers at the prism interface.

The higher Ca diffusion coefficient of the interior IGF than the two ordered parts in the IGF adjacent to the crystal surfaces showed that the interior IGF can be a good transportation channel for Ca ions. The ordered interface can act as a limited sink for Ca ions and will be easily saturated. *Ca diffusion and equilibrium will be affected if the IGF is so thin that the ordered regions adjacent to the crystal surfaces overlap.*

IV.4 Conclusions

Ca diffusion within calcium alumino-silicate intergranular films connecting two dissimilar alumina crystal surfaces was studied using molecular dynamics simulations. Two alumina crystals with the (0001) and $(11\bar{2}0)$ planes in contact with the same IGF were used. Ca diffusion in the IGFs was evaluated in three regions: diffusion within volumes adjacent to each of the interfaces with the crystal surfaces and diffusion within the interior of the IGF. Ca diffusion was also determined in bulk glasses of the same compositions as those used in the IGFs in order to determine the effect of confinement in a thin film between crystals on diffusion.

Results showed that the activation energy for Ca diffusion within the bulk glasses was in the range of the experimental data and all but the highest calcia glasses showed similar activation energies. The activation energy for Ca diffusion in the interior of the IGFs was similar to, but slightly lower than, that in the bulk glasses.

Most importantly, diffusion near the interfaces was considerably decreased in all cases and the activation energies were increased in comparison to both the bulk glasses and the IGF interiors. The diffusion constants are much lower and the activation energy much higher for Ca near the prism surface of the IGF containing the highest concentration of Al (the 112 anorthite composition) than all other regions. Growth of the crystal caused by adsorption of Al and O from the IGF onto the prism surface of the crystal in the 112 IGF apparently affected Ca diffusion significantly. Such growth was not observed in the other compositions[96].

Results show that Ca diffusion in the interior of the IGF is similar to that in the bulk glass and should be the transport path of Ca ions during sintering. If the IGF thickness decreases too much, so that the interior volume disappears as the ordered regions adjacent to the crystal surfaces overlap, then Ca diffusion into the IGF would be severely restricted, affecting equilibrium.

V. Molecular Dynamics Simulations of the Effect of the Composition of Calcium Alumino-Silicate Intergranular Films on Alumina Grain Growth

V.1 Introduction

Alumina ceramic is an important industrial material in many applications for its high hardness, corrosion resistance and low thermal expansion coefficient. The green compacts and the sintering procedures have great effects on the structure and mechanical properties of the final products. More further, in order to improve other mechanical properties such as low fracture toughness and poor thermal shock resistance, one or several doping materials are added to get the desired results.

Amorphous intergranular films present between liquid-sintered alumina grains and non-pure alumina sintering processes introduce Ca, Si and other impurities[54, 89, 123]. Many experiments show that there are significant differences in the final structure and mechanical properties between the pure (greater than 99.99%) and the doped alumina ceramics[29]. For pure Al_2O_3 sintered in clean conditions, normal and continuous grain growth is found, following normal-grain-growth-kinetics. The final sintered structure is homogeneous and only equiaxed grains are found experimentally[124]. However, when commercial alumina is used or some sintering aids (like Si, Ca, Mg and other cations) are added into the pure alumina before the sintering process, grain growth behavior changes and the microstructure of the grains and grain boundaries vary from the pure conditions. Not only is the grain growth dependent on the purity of the alumina and the sintering conditions, but densification is also affected. Experimental results show that lattice diffusion dominates the densification under clean conditions while lattice and grain-boundary diffusion both contribute to the densification under normal sintering conditions[16].

Some experiments show that abnormal grain growth (AGG) is not found at the initial stage of the sintering while the grain size is quite small, but grain size in itself is not the reason for AGG[29]. Even in the sintering of pure alumina, AGG was observed after very long sintering time because the contaminant cannot be avoided completely. AGG is not an intrinsic property of alumina but an extrinsic property that is controlled by the impurities or contaminants[125]. However, impurity species in alumina have a different effect on AGG. It is well accepted that the presence of the Ca and Si at the grain boundary triggers AGG, while Mg inhibits AGG in alumina sintering[40, 41, 53, 65, 126]. Plate-like crystals form large, flat basal surfaces with thin intergranular films when AGG happens[127]. Because of the possible uneven distribution of a small amount of liquid between grain boundaries and triple points, Kolar suggested that the coexistence of both wet and dry boundaries may bring about AGG[128]. After investigating four commercial alumina powders, Cho et al. proposed that chemical inhomogeneity is the reason for AGG because they found that in such alumina a relatively small portion of coarse particles in all powders contain significantly high concentration of impurities[42]. On the other hand, by comparing the alumina crystal shape with AGG experimentally, the basal planes were found to be very smooth and flat while the prism planes were rough[32]. The energy barrier for the attachment to the rough surface is negligible compared to that on the smooth flat surface in the coarsening process controlled by interface diffusion. So only very large grains would gain enough driving force for the nucleation on the flat surface, and then coarsening could happen. Because the coarsening caused by 2-D nucleation will show a discontinuous grain growth behavior in different orientation planes, Lee suggested that the nucleation process at different planes is the reason for the AGG[32]. In Kwon's experiments, the appearance of liquid phase (IGF) was thought to increase the boundary mobility and AGG is explained as a result of the enhanced growth on the non-basal plane due to the re-entrant edges formed at the grain boundaries[129].

Experiments also show that significant segregation of Ca and other cations at the alumina grain boundaries happens while such impurities are still below the solid solution limits in the grains[40]. The segregation of calcium is anisotropic for different orientations of alumina. Bae and Baek showed that low concentrations of either calcia or silica in the IGF or smaller combinations of both together cause AGG in alumina[16]. It is very hard to study of the atomic structure of the IGF in the polycrystalline ceramics experimentally because of the extremely thin and amorphous structures of these films, although there has been recent success in studies of IGFs in Si_3N_4 [37, 130, 131]. It is proposed that an IGF should have a stable equilibrium thickness at the order of several nanometers[132], although the structure of such a thin glass between crystals should be different than the bulk glass analog because of the influence of contact with the crystal surfaces.

Considering bulk glass structure, Al ions in silicate glasses occupy tetrahedral sites, as opposed to the octahedral sites in α-Al_2O_3. In order for this to occur, a charge compensating cation is usually associated with the AlO_4^- site. Tetrahedral Al is also observed in siliceous zeolites. With a sufficient concentration of Ca in the IGF to charge compensate 2 Al for each Ca, the Al ions can remain tetrahedrally coordinated (to maintain the silicate glass network structure). Excess CaO ($R=[Ca]/[Al] >0.5$) in a silicate glass would cause formation of so-called non-bridging oxygen (NBO), which are singly coordinated to a strong network former (such as Si) and less strongly bonded to the network modifier (Ca). (A brief discussion of the role of Al and modifier ions in silicate glasses using alkali alumino-silicates is available in [62] and references therein.) As related to the IGF in contact with a basal oriented alumina surface, any Ca in excess of the charge equivalence point (R_e=[Ca]/[Al] =0.5), would mean either formation of NBO in the IGF or segregation of the Ca to the basal crystal surface to charge compensate undercoordinated O present at the surface[70]. The combination of NBO in the IGF glass and undercoordinated O in the crystal lattice surface is energetically less favorable than no NBOs in the glass and no undercoordinated O in the surface. The latter situation was the case in our earlier study of IGF compositions [70, 96], where Ca ions preferentially segregated to the alumina basal crystal surface. However, with increasing amounts of alumina in excess of the CaO equivalence($R<R_e$), behavior might change.

Our previous simulations of amorphous silicate IGFs in contact with alumina crystals and silicon nitride crystals clearly showed ordered structures at the interfaces and density oscillations into the IGF induced by the crystals[70, 73, 75, 96, 97, 117]. Recent High Resolution TEM (HRTEM) studies observe such density oscillations[131]. These density oscillations decay within a nanometer of the interface, attaining a glassy structure in the interior of the thicker films. Most importantly, the previous simulations of IGFs between the differently oriented crystals showed anisotropic growth[96, 97]. ‘Growth’ in our discussion means adsorption of species from the IGF onto the crystal surface consistent with the crystal orientation and composition such that the crystal lattice extends along the surface normal of the particular plane in contact with the IGF. In the nitride case, growth along the basal surface normal was more rapid than that along the prism surface normal. In the alumina case, the simulations showed preferential growth along the $[11\bar{2}0]$ direction on the $(11\bar{2}0)$ oriented crystal and no such growth in the [0001] direction on the basal crystal. Both results are consistent with anisotropic grain growth in the respective systems seen experimentally. Concentrating on the alumina system, the presence of Ca ions in the IGF affected adsorption of Al ions from the IGF onto the crystal lattice sites on the (0001) surface, creating the anisotropy in growth behavior. However, experimental data clearly show that normal grain growth occurs in the alumina system, so composition of the IGF must play an important role. In this section, higher concentrations of Al in the IGF ($R<0.5$) than those previously considered are used to evaluate growth behavior.

V.2 Computer Procedures

Five calcium-alumino-silicate IGF compositions were chosen for the current work. They are identified by the their species ratio ($CaO:Al_2O_3:SiO_2$) and are given in Table V-1, along with system sizes. The glassy IGFs were made between two dissimilar α-alumina orientations, the (0001) and ($11\bar{2}0$), creating a ((0001) oriented crystal)/(IGF)/(($11\bar{2}0$) oriented crystal) system. A schematic drawing of the system is shown in figure III-1. The simulation procedure is the same as that previously published[96], where it is discussed in detail in section III. The only difference is that different IGF compositions are studied here.

Table V-1. Composition and system sizes.

Sample No.	Mole ratio CaO : Al_2O_3 : SiO_2	Specific Number of Atoms				TOTAL
		Ca	Al	Si	O	
334	3:3:4	720	1440	960	4800	7920
123	1:2:3	400	1600	1200	5200	8400
221	2:2:1	1000	2000	500	5000	8500
121	1:2:1	550	2200	550	4950	8250
141	1:4:1	340	2720	340	5100	8500

Table V-2. Melt /quench process for making glassy IGF between crystals.

Quench temperature	Conditions	Duration
10000K	NVE, crystal frozen	10 ps
8000K	x, y constant*, P_z=5 GPa	20 ps
6000K	As above	40 ps
4000K	As above	40 ps
3000K	x, y constant, P_z=3 GPa, crystal de-frozen	50 ps
2000K	NPT, p=0.1 MPa	100 ps
1000K	As above	100 ps
300K	As above	20 ps
* x, y dimensions change with thermal expansion coefficient as T changes.		

The glassy IGFs are made between the crystals by randomly inserting the atoms of the IGF composition in the volume between the crystals, followed by a melt/quench procedure shown in Table V-2, similar to it in section III. Both NVE and NPT simulations are used and a timestep of $1x10^{-15}s$ is used throughout the simulations. In order to minimize interface mixing and roughening, the crystal atoms do not respond to the interatomic forces at the high melt temperatures. While dissolution and reprecipitation of the crystals would be more realistic, the computational time would be prohibitive. In addition, the roughened interface would be considerably less amenable to subsequent analysis and the time required to attain a re-smoothed surface might again be computationally prohibitive. At these higher temperatures, the crystal atoms nonetheless do relax en-masse to the external pressure applied in the direction perpendicular to the IGF/crystal interfaces. This procedure allows attainment of the appropriate thickness for the constant number of atoms in the IGF based on the resultant IGF structure. At lower temperatures, all atoms respond to the interatomic forces except those in the frozen layers farthest from the crystal/IGF interfaces, which still moved en-masse to the external pressure. The x, y, and z dimensions are approximately 5.2nm, 5nm, 10nm, respectively, with x and y dimensions changing with the thermal expansion coefficient of the crystal to minimize elastic effects. The IGF is ~4nm in all simulations. Again, details have been presented elsewhere [96]. In addition, the results from those previous simulations are included here to show the effect of composition of the IGF on growth on the different crystallographic orientations.

V.3 Results and Discussion

V.3.1 Snapshots

Similar to previous simulations, the interior portions of the IGF were amorphous[96]. For brevity, they are not shown or discussed in this section. The thin slabs of ordered structures at the (0001) basal and $(11\bar{2}0)$ prism interfaces of two representative systems are shown in figure V-1. The original crystal and the IGF atoms are separated by a solid straight line in the snapshots, with the crystal atoms below the line. The snapshots of these systems show the evolution of the interface structures for two different IGF compositions. At the basal side, the ordered "cage" structures previously reported are clear and almost fully occupied by Ca ions in the 221 system because of the high Ca concentration in this system. The 2 Ca ions in a single cage in the 221 basal image are offset by the third dimension into the plane of the image. Ca ions preferentially segregate to the 'cage' sites in calcium silicate IGFs [70], where they charge compensate the tetrahedrally coordinated terminal Al on the crystal surface (similar to a zeolitic Al) and the undercoordinated O in the crystal surface. This 'cage' structure has been discussed previously [70, 75].

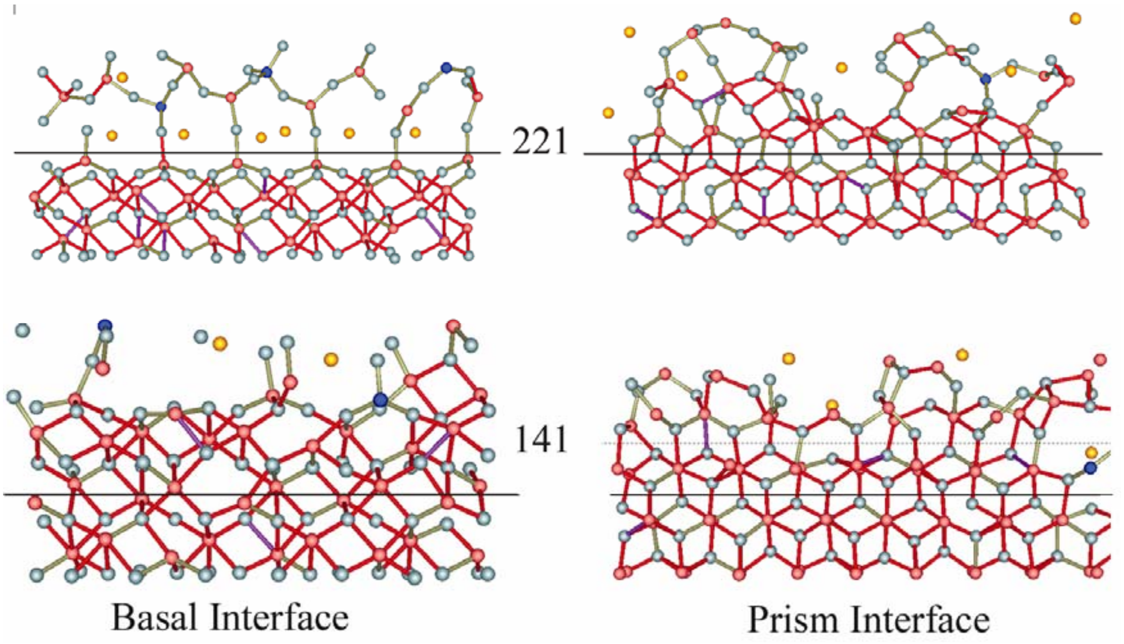

Fig. V-1. Snapshots of thin cross-sections of atoms into the plane of the page near the Basal and Prism interfaces of 2 compositions in the simulations. Atoms from the crystal are below the dark solid horizontal line in each image; atoms originally from the IGF are above the dark horizontal line. Atoms between the dashed line and the solid line in 141 Prism image indicates the degree of ordering of the atoms from the IGF that adsorbed onto the crystal surface, forming an extension of the prism oriented crystal. Al=red, O=grey, Si=blue, Ca=yellow. Ca-O bonds are not drawn.

At the prism side, growth of the crystal is observed in both examples, with multiple crystalline layers forming on the prism surface of the 141 system. The atoms above the solid line are from the IGF and those between the solid line and the dashed line clearly show the growth of the crystal layer in the $[11\bar{2}0]$ direction at this composition. Even the atoms above the dashed line show the beginnings of order similar to the crystal.

V.3.2 Density Profile Analysis

The density profiles of atoms near the basal and prism interfaces for all of the systems studied in this paper are shown in figure V-2. The concentration of Al in the IGF is increasing in the order of 334, 123, 221, 121 and 141. The density profile of atoms in the basal oriented crystal shows the single O peak and the double Al peaks while that of atoms in the prism oriented crystal shows the double O peaks and single Al peak, consistent with each crystalline orientation. The lowest surface energy configurations of these crystals is the single Al termination plane for the basal surface and the single O termination plane for the prism surface. Therefore, continuation of each crystal along the specific surface normal of each orientation requires a second Al peak to occur on the basal side, followed by an O peak and a second O peak to occur on the prism side, followed by an Al peak.

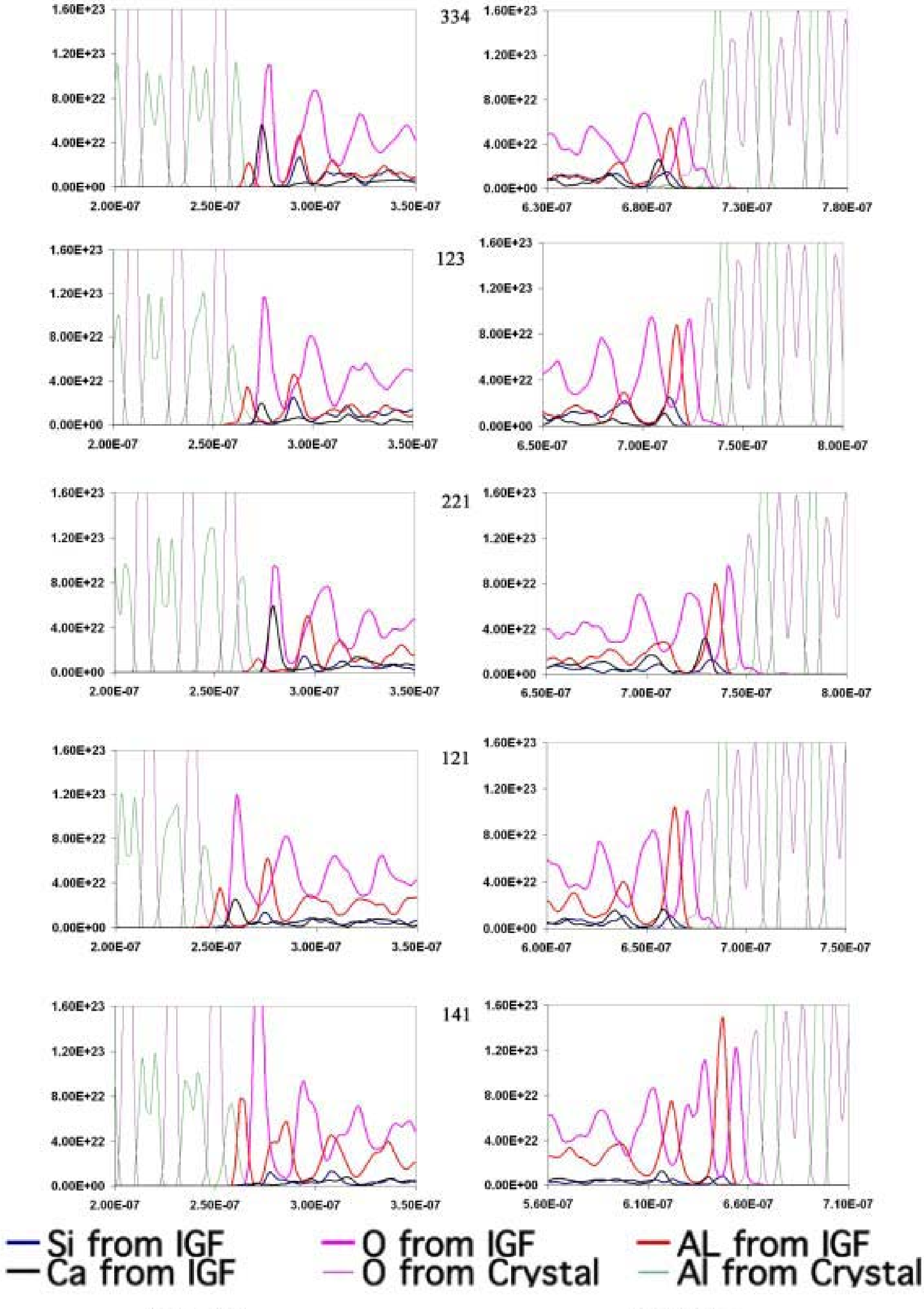

Fig. V-2. Density profiles of individual species at the Basal and Prism sides of the IGF for the 5 compositions as a function of distance perpendicular to the IGF-crystal interface. Thicker lines are for ions in the IGF. Line color associated with atom type is shown at the bottom of the figure.

Previous simulations showed that Ca ions preferentially adsorbed onto the basal surface in calcium silicate IGF compositions[70], inhibiting Al adsorption in calcium alumino-silicate IGF compositions[73, 96]. This is again the case for most of the compositions studied here, as shown on the left side of figure V-2. At the basal side, for all but the 141 composition, the first adsorbed Al peak from the IGF is much smaller than the terminal Al crystal peak on this side, and the first adsorbed Ca peak is present at the same position as the first O peak (indicative of the cage structure shown in figure V-1).

At the equivalence point (R_e=0.5) in the 334 and 221 systems, the first adsorbed Ca peak is larger than that in the other compositions and the first adsorbed Al peak adjacent to the basal surface is smaller than that in the other compositions which have excess Al ($R<R_e$) in the IGF. In the 334 and 221 systems, one might anticipate that the Ca and Al would remain equally associated within the IGF (as would be the case in a silicate glass). However, the presence of the crystal surfaces modifies this behavior and, as seen in all of the compositions, a very strong second adsorbed Al peak forms on the basal side (which is at the 'top' of the cage structure [73]). The Al in this second peak are predominantly 4 coordinated, as shown in the 334 system in figure V-3, thus requiring charge compensation by the Ca. So the first adsorbed Ca layer charge compensates the tetrahedral Al in the terminal plane of the original crystal and the undercoordinated O in the crystal surface [70, 75, 117], as well as the Al in the second adsorbed peak.

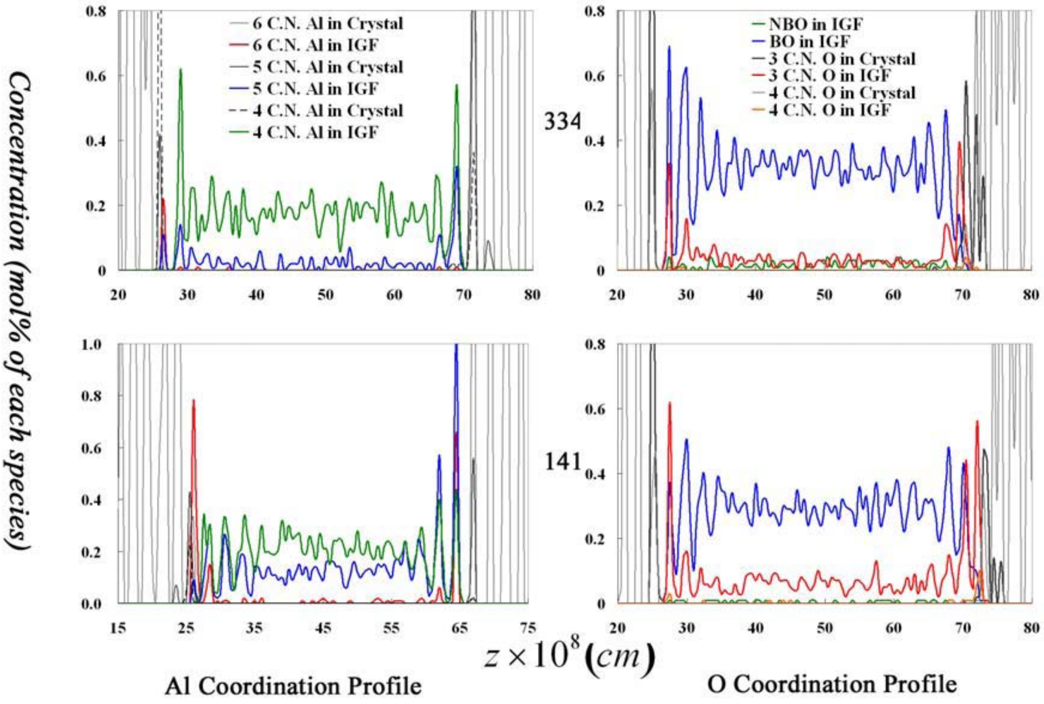

Fig. V-3. Coordination of Al and O species in the IGF and crystal surfaces for 2 compositions. Note the different scale of the concentrations in the Al profile in the 141 system. Al and O are predominantly 4- and 2-coordinated, respectively, in the IGF, as expected for the glass, with increasing coordination at the interfaces, consistent with the higher coordination of each in the crystal.

The results also indicate that the Ca ions are inhibiting Al adsorption onto the basal surface. With less Ca in the IGF, the first adsorbed Ca peak is decreased and the first adsorbed Al peak is increased (123, 121, and 141 compositions).

Figure V-2 also clearly shows that behavior is quite different in the 141 system. Here, the peak of first Al adsorbed from the IGF onto the basal oriented crystal has a density nearly that of the terminal Al layer in the crystal, and the first adsorbed Ca peak is missing. At this composition, with $R \ll R_e$, the Ca ions remain in the IGF to charge compensate the Al, with excess Al moving to both interfaces. In addition, in the 141 composition, the next adsorbed Al peak on the basal side has a shoulder and the beginning of a splitting of the peak, consistent with the double Al peak of the crystal with this orientation. The implication is that the 141 composition enables growth of the basal crystal along its surface normal in the [0001] direction because R is so low. In the current version of the simulation protocol, it would be expected that eventually enough Al would be removed from the glassy IGF to lower R to the point where behavior is similar to the other compositions and adsorption (growth) slows. Of course, in a real system, a supply of ions from a source, such as dissolving alumina grains or a triple point, could offset this depletion process.

On the prism side, O from the IGF appropriately adsorbs initially, followed by a strong Al peak that grows to nearly equal that in the crystal. In the 141 composition, the strong first O and first Al peaks are followed by the next adsorbed O peak, which shows a splitting consistent with continuation of the crystal structure with this orientation. Ca has little effect on adsorption and growth on the prism side.

Therefore, the simulations show that Ca ions inhibit growth on the basal surface for most compositions, but has little or no effect on the prism surface. This effect will be discussed more fully below.

V.3.3 Coordination Number Analysis

The coordination number (CN) of Al and O are distinctly different in α-Al_2O_3 versus the aluminosilicate glass (the Si are 4 coordinated). The CN of Al and O in α-Al_2O_3 crystal is 6 and 4 respectively. In alkali and alkaline earth aluminosilicate glasses, Al is tetrahedrally coordinated and, depending on the alkali or alkaline earth to Al ratio, O is a mix of 2 coordinated (bridging oxygen), 1 coordinated (non-bridging oxygen), or 3 coordinated. The coordination of Al and O as a function of distance perpendicular to the IGF/crystal interfaces is shown in figure V-3 for 2 systems (334 and 141). The main features are that the Al and O in the IGF are predominantly 4- and 2-coordinated, as expected in the glass, with higher coordination for each at the interfaces, which is consistent with the higher coordination of each in the crystal. Also, with significantly excess Al in the IGF (the 141 system), the coordination of Al and O both increase in the glassy interior of the IGF. The correlation between coordination number of Al and O in alkali alumino-silicate glasses as a function of modifier content has been previously discussed [62, 133, 134], with coordinations similar to that shown here. The increased coordination of Al and O in the glassy part of the IGF indicates a strain instability in the glass in comparison to 4 coordinated Al charge compensated by Ca and normal 2-coordinated O that would be consistent with the network structure of a silicate glass. The implication is that the Al (and O) should segregate to the interfaces to reduce the strain sites in the IGF when the R value is low. Another implication is that with sufficiently low Si content, the silicate glass structure might not dominate the IGF and a crystalline aluminate might form.

V.3.4 The relationship between the crystal growth and the Al content in IGF

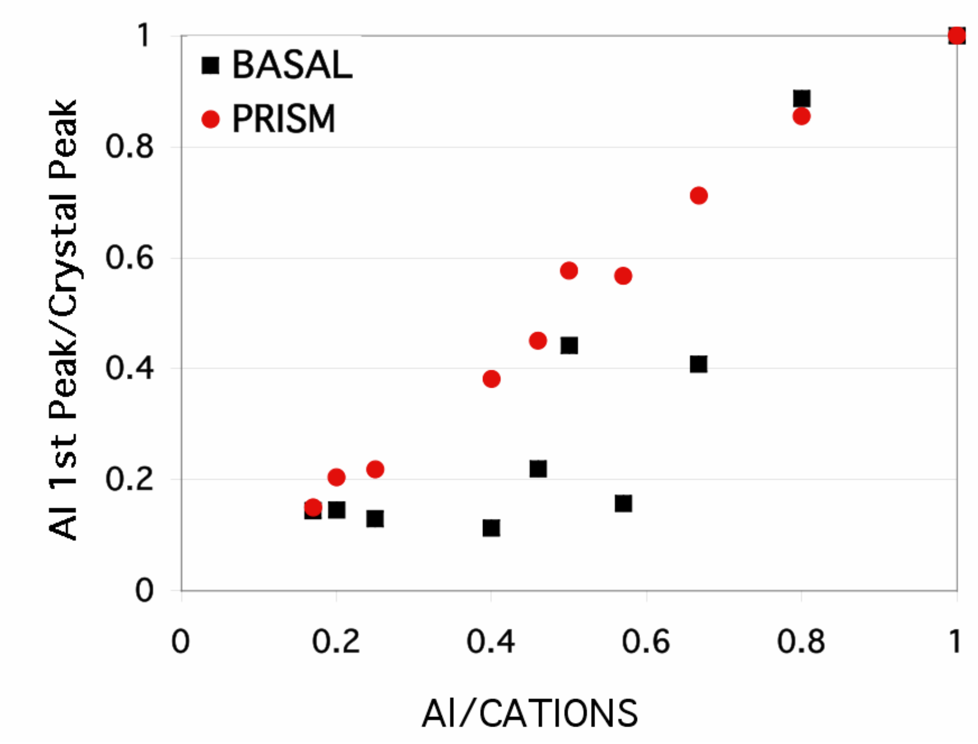

Fig. V-4. Normalized area under the first adsorbed Al peak from the IGF onto the different crystal surfaces as a function of the ratio of Al/all cations for the compositions presented here and the 4 compositions previously studied (see ref 24). Note the significantly faster growth along the prism surface normal than the basal surface normal for most compositions, except at the lowest and highest Al ratio.

Figure V-4 shows the integrated intensity of the first adsorbed Al peak on each interface normalized by the integrated intensity of the Al peak in the appropriately oriented crystal as a function of the ratio of Al ions to the sum of all cations. Included in the figure are the data from the IGF systems previously reported [96]. The normalized integrated intensity of the first adsorbed Al peak onto the crystal surface is used as an indicator of growth of the crystal. As mentioned above, ‘growth’ here means adsorption of species from the IGF onto the crystal surface consistent with the crystal orientation and composition such that the crystal lattice extends along the surface normal of the particular plane in contact with the IGF. The results clearly show more rapid growth along the $[11\bar{2}0]$ direction on the prism-oriented crystal than along the [0001] direction of the basal-oriented crystal, except at the highest Al concentration in the IGF. This difference in growth behavior is consistent with anisotropic grain growth observed experimentally in this system. In anisotropic grain growth in the alumina system, growth along the prism surface normal is much faster than that along the basal surface normal. Clearly, over most of the compositions used here, growth along the prism surface normal is 2-4 times faster than that on the basal surface.

At sufficiently high concentrations of Al in the IGF, near 0.8, growth along the basal surface normal is equivalent to that on the prism surface, indicating isotropic grain growth. That is, when the composition within the IGF has a sufficiently large concentration of Al present, Al and O ions adsorb onto both crystal surfaces epitaxially and extend the crystal dimension out in the direction of each surface normal. At this 141 composition, there is clearly a large excess of Al in comparison to Ca, allowing for more Al to adsorb onto the crystal sites before the Ca/2Al ratio gets too high and inhibits continued growth. Therefore, with a sufficient supply of Al in the IGF, isotropic growth would be expected as Al adsorbs equally onto both basal and prism oriented crystal surfaces.

The data point at 0.5 Al/all cations (from the 123 system) and the two data points on either side (the 334 and 221) were reproduced in additional simulations with only minor variance, indicating something significant occurring at this specific composition. The 123 data point on the basal side is approximately the same as the value in the 121 system (seen at 0.66 Al/all cations). While the concentration of Si increases from the 121 to the 123, the R value remains the same. Considering the effect of the Ca/Al ratio (R) on the normalized adsorbed Al peak intensities provides clarification.

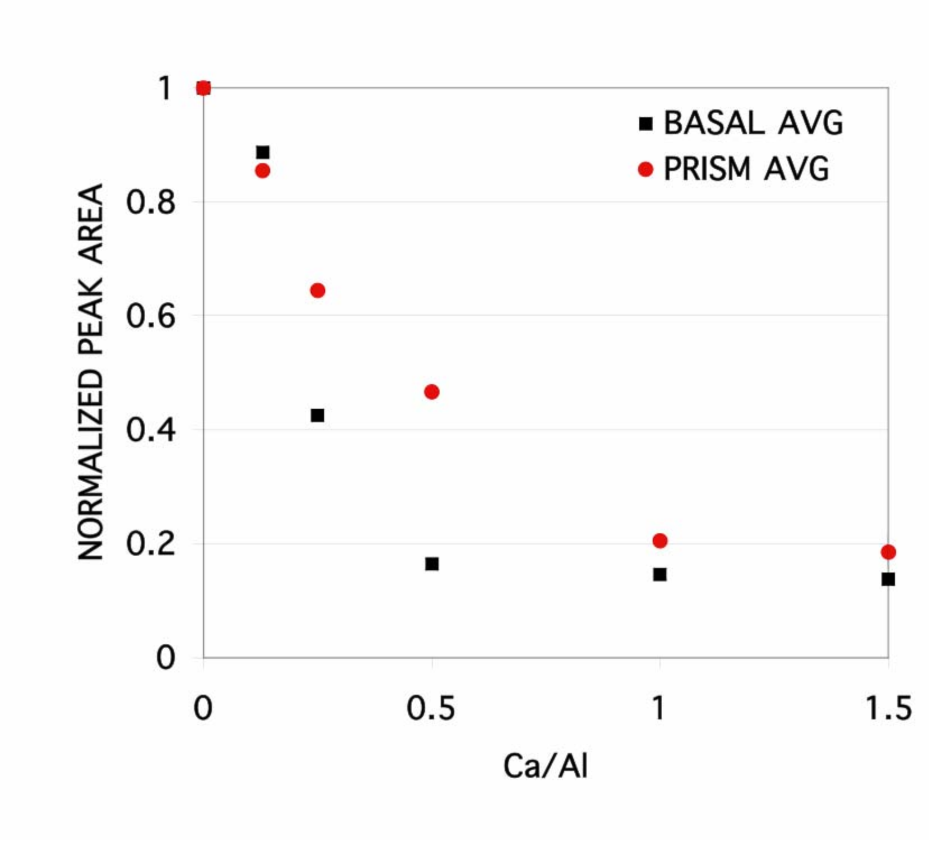

Fig. V-5. Average normalized area under the first adsorbed Al peak from the IGF onto the different crystal surfaces as a function of the Ca/Al ratio (R) for the compositions presented here and the 4 compositions previously studied (see ref 24). The equivalence point, R_e, is at 0.5. Below R_e, excess Al in the IGF allows for more rapid adsorption of Al onto the basal surface than that above the equivalence point.

Figure V-5 shows the plot of the adsorbed Al peak intensities, normalized by the crystal peak intensities, averaged over equivalent R values in the IGFs, as a function of the Ca/Al ratio, R. Results clearly show that with $R >> 0.5$, little Al adsorbs onto the surfaces, although slightly more Al adsorbs onto the prism surface. At $R\sim0.5$, Al adsorption onto the prism surface increases significantly, with little change on the basal surface, indicating anisotropic grain growth. With $R<R_e$, adsorption onto the basal surface increases until it attains the same relative peak intensity as the prism surface at the lowest R value used here. At this lowest R value composition, isotropic growth is expected. The results imply grain growth would be most anisotropic near the equivalence point $R=0.5$ and the most isotropic at very high and very low R values.

While crystal growth is complicated and depends on a variety of complex behavior, including dissolution of small grains or high energy surfaces, lattice versus grain boundary transport, reprecipitation, local stresses and strains, etc., the results shown here indicate the important role of the composition of the IGF on local behavior on prism and basal surfaces under the exact same conditions. Most importantly, the results show anisotropy in growth consistent with experimental observations, where growth along the basal surface normal is much slower than that on the prism surface normal, creating platelet alumina structure.

V.4 Conclusions

Molecular dynamic simulations show the effect of the composition of the intergranular film (IGF) between dissimilarly oriented α-Al_2O_3 crystals on growth in the direction of each surface normal. The IGF in contact with the alumina (0001) basal plane on one side and the $(11\bar{2}0)$ prism plane on the other showed preferential growth in the $[11\bar{2}0]$ direction at all but the highest and lowest Ca/Al ratios in the IGF. Anisotropic grain growth in alumina is observed experimentally as excessive growth along the prism surface normal in comparison to the basal surface normal, creating platelet morphology. These simulations are consistent with such results and indicate the mechanism by which growth on the basal plane is inhibited, affecting growth. The role of Ca in the IGF is important and affects growth on the basal plane by poisoning surface sites based on the attraction of the Ca to charge compensate O on and adjacent to the basal surface. At Ca/Al ratios >> 0.5, which is the charge equivalence ratio, Al adsorption onto both surfaces is similar, but low, indicating slow isotropic growth. At Ca/Al ratios << 0.5, Al adsorption is also similar on both surfaces, but fast, again indicating isotropic growth. In between these extreme Ca/Al ratios in the IGF, growth along the surface normal of the basal plane is inhibited in comparison to that on the prism plane, indicating anisotropic grain growth.

VI. Molecular Dynamic Simulations of Dissolutions of (0001) Basal and $(11\bar{2}0)$ Prism Oriented α-Alumina Grains in Different Silicates

VI.1 Introduction

Liquid phase sintering (LPS) has been an important process for making dense ceramic materials. In many ceramics, either impurities are sufficiently abundant to segregate to the crystal surfaces and form a film that melts at high temperature or specific sintering aids are added to the composition. In either case, a liquid phase is present that often exists between the two-crystal junctions, forming an intergranular film (IGF) [32, 135-137]. In the case of alumina, a thin amorphous calcium alumino-silicate film of the anorthite composition is often observed. During LPS, the composition of the IGF must change as crystals dissolve into the liquid silicate phase and species are transported into or out of the IGF that is in contact with triple point pockets. It would also be expected that certain surface orientations are more stable than others (based on lower surface energies) and at these elevated temperatures would be less prone to dissolution.

The dissolution of solid oxide crystals, such as refractory alumina, in silicate melts has been studied for many years. Extensive studies can be found on the dissolution of either the single-crystal sapphire or dense polycrystalline alumina ceramics in different silicate melts[138-143]. The experimental data showed that the dissolution behavior of the alumina crystals can either be homogeneous (direct) or heterogeneous (indirect) based on the experimental conditions[142-144]. In homogeneous dissolution, the alumina dissolves directly into the liquid without any intermediates. Heterogeneity occurs when one or more chemical reactions occur at the crystal/melt interfaces and interface structures form between them. Due to the interface structures, the dissolution process has separated phases: the crystal ions would first diffuse into the interface structures then continue to move into the melt. Indirect dissolution behavior affects both the dissolution rate and the morphology of the crystals.

In general, the mass transport rate was found to determine the direct dissolution rate since other steps involved in this procedure, such as surface reactions, are faster than that of the ions diffusing from the crystal surface into the melt[138, 142, 145, 146]. The magnitude of the solvent (Al_2O_3) concentration gradient very close to the crystal surface and the thickness of the diffusion layer are important to the rate. When the melt is Al_2O_3 saturated, dissolution may stop[144]. However, the chemical reactions always occur at the alumina crystal surface and solid structures form at the interface[142, 144]. Also, other species, such as CaO or MgO, are included in the melt composition in many cases, which make behavior more complicated. The interface structures, like calcium aluminate spinals $CaO\text{-}2Al_2O_3$ (CA_2) and $CaO\text{-}6Al_2O_3$ (CA_6), are often observed in experiments. Also, the studies discover that the interface structures are not continuous, so the dissolution is not completely indirect[144]. Recently, Shaowei examined the dissolution of tabular alumina in silicate melts and observed that the interface layer, CA_6, did not cover the crystal surface fully and while the alumina dissolved indirectly through the interface structures, the slag still contacted the alumina directly. After long time dissolution, the tabular alumina was penetrated by the melt[144]. Guha observed that the interface structure is dependent on the temperature when the polycrystalline Al_2O_3 was dissolved into CAS slag between 1400°C and 1550°C[147]. With increasing dissolution time and temperature, interface structure would change from CA_2 to CA_6, through some intermediate states[144, 147]. The incompatibility between these states and Al_2O_3 will also allow the melts to penetrate the grain boundaries of Al_2O_3.

Previous work in our lab showed the adsorption of particular species from molten silicate IGFs onto alumina surfaces[70]. This preferential adsorption altered the growth of dissimilarly oriented alumina crystals[96, 148]. Preferential growth consistent with anisotropic grain growth in alumina occurred at specific IGF compositions, while isotropic growth occurred at other IGF compositions[148]. In the current study, the opposite behavior, the dissolution of the basal (0001) and prism $(11\bar{2}0)$ surfaces of alumina in contact with siliceous melts, was examined by molecular dynamics (MD) computer simulation. The surface energy of the single Al termination plane of the (0001) surface is near $2.0 J/m^2$ while the single O termination plane of the $(11\bar{2}0)$ surface is near $2.4 J/m^2$[68, 72, 149]. We would therefore anticipate the basal plane being more stable at elevated temperature than the prism plane, even in contact with the silica/silicate melts studied here. These melts include silica, alumino-silicate, calcium silicate, and calcium alumino-silicate. In experiments, other unavoidable trace species may have some unknown effects on the dissolution behavior while in the MD simulation it is easy to determine the specific effect of each species. The MD method can show the atomistic level analysis of the interface structure at dissolution without other extraneous factors.

VI.2 Computation Procedure

In this initial simulation of the dissolution of alumina into the melts, two simple melts, aluminosilicate (25 mole% Al_2O_3) and calcium silicate (40 mole% CaO) are used to examine the effect of the Al and Ca on the dissolution of crystals. Before the dissolution simulation, the interface between the Al_2O_3 crystal and melt was formed by the melt-quench procedures as applied in previous studies. The dissolution of crystal will start at the interfaces between the melts and the crystal surfaces. Another side of the melts is a free surface. Periodic boundary conditions (PBC) exist in X and Y dimensions, but not in the z direction, which means that there is a free surface above the melt. The dissolution simulations were carried out at two high temperatures, 3500K and 4000K independently. The dissolution time for each temperature is 50ps. The analyses were taken out for the structure after 50ps in elevated temperatures. To eliminate the thermal expansion effect of the whole system at high temperature compared to the room temperature, the structures were immediately quenched to room temperature and run for 40ps, of which the final 20ps are used for the analysis of the density profiles of ions to determine dissolution of the crystals into the various melts.

VI.3 Results & Discussion

Generally, the dissolution of alumina crystal into the silicate melts starts at the interface between the crystal surface and the melts at elevated temperatures. The ordered crystal structure at the surface will lose as the crystal atoms react with and diffuse into the melts. In current studies, the dissolution behaviors of alumina crystal were characterized by the transitional diffusion and distribution of Al atoms at the interface regions during the simulation time. The atoms density profiles of all the species were calculated for the analysis of the dissolution. The effects of the temperature, crystal orientation and the composition of the silicate melt in the crystal dissolution were discussed separately, although they are related each other.

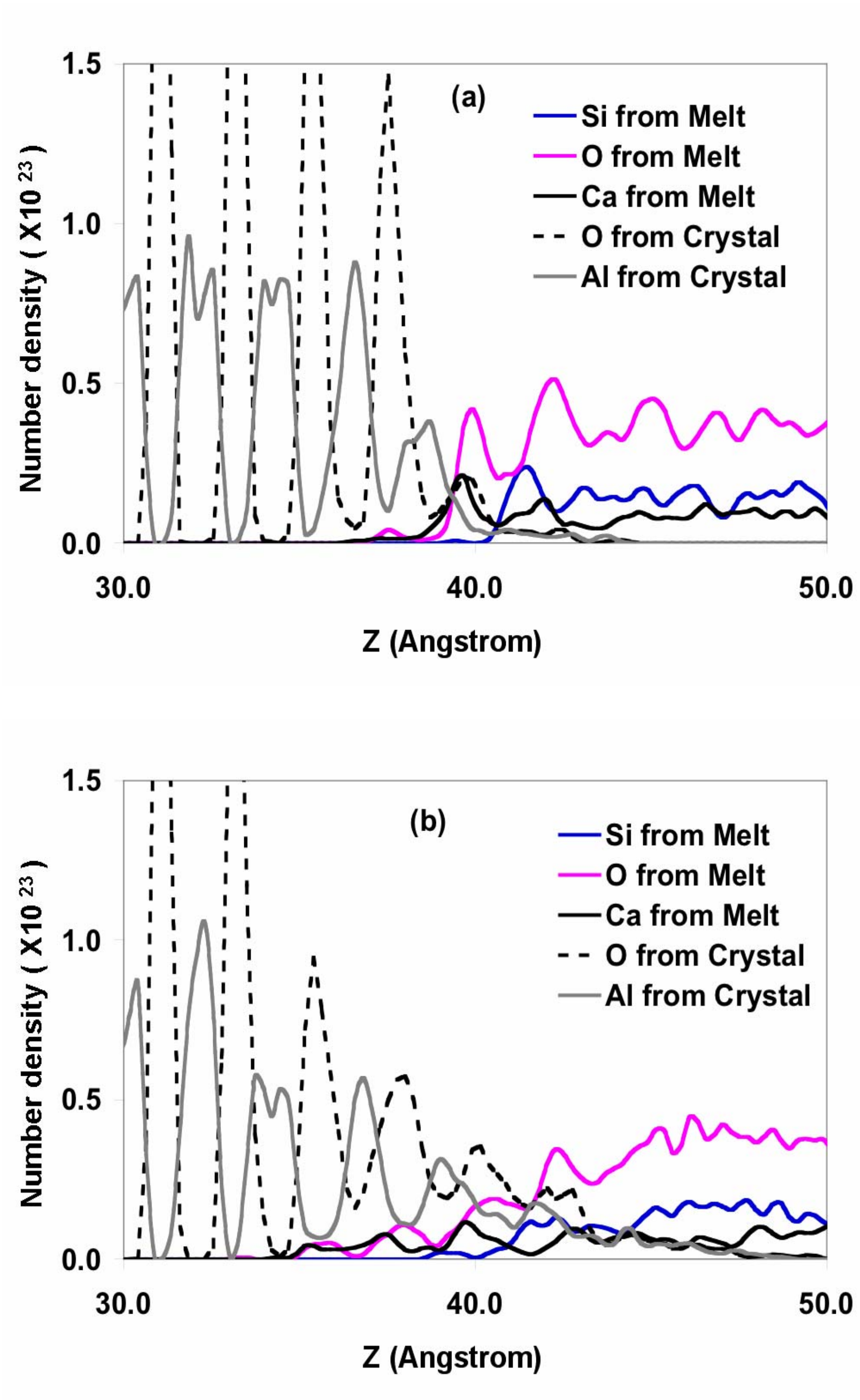

Fig. VI-1 Basal Alumina crystal dissolution in CaO.SiO_2 melt at 3500K (a) and 4000K (b).

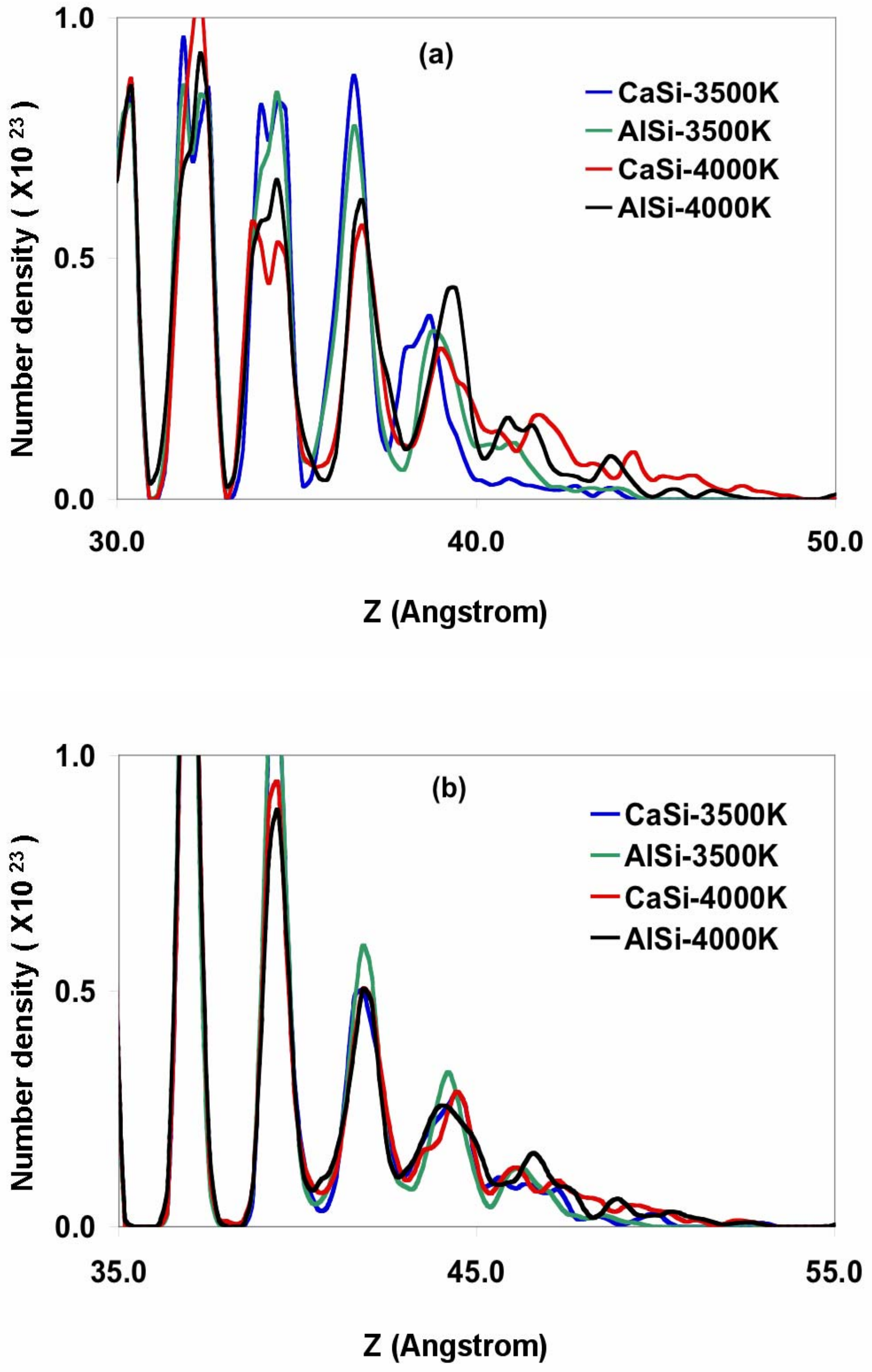

Fig. VI-2 The density profile of crystal Al atoms in both melts at the interface region for both the temperatures simulated: (a) basal alumina crystal, (b) prism alumina crystal.

VI.3.1 The Dissolution Temperature

The temperature certainly has a significant effect on the dissolution of the crystals. The mobility of the atoms, both of the crystal and melt, the interface reaction rate and the diffusion of the atoms were increased as the temperature arising. Figure VI-1 shows the density profile of the basal alumina crystals dissolution in $CaO.SiO_2$ silicate melt at 3500K (a) and 4000K (b) as an example. All species involved in the dissolution were presented in this figure and the *z* direction was perpendicular to the interface plane. Though other species other than Al would show some features of the dissolution, the Al atom redistribution in the system by dissolving from the crystal and diffusing into the melt, represents the important significance of the crystal dissolution after certain time, as shown in figure VI-2 at the simulated high temperatures in different melts. In the simulations, the last alumina peak of the basal and prism alumina crystal stops at 38.5 and 42.3 angstroms respectively before dissolution.

At the elevated temperatures used in the simulations, the crystals, basal or prism, were unstable in the selected melts as shown in the figure VI-1 and figure VI-2. The crystal atoms left their ordered sites and move into the melts. Meanwhile, the melts atoms attacked the crystal structure by diffusing into the vacancies in the crystal or exchanging with the crystal atoms. Both activities could generate some intermediate phases and change the ordered phase near the crystal surface into amorphous phase, similar as the melts, though the composition was different with the dissolving species from the crystal. More Al and O atoms moved out of the crystal as the dissolution temperature was raised from 3500K to 4000K as show in figure VI-1 and figure VI-2. At 4000K, the species in the melts (Si, Ca and O), especially for the Ca, moved much deeper in the crystal, suggested more vacancies and exchanges in the crystal than they did at 3500K. Such phenomena can be seen in other simulated system (except there is no Ca in the $Al_2O_3.SiO_2$ melt). In figure VI-2, the basal crystal Al peaks stops at 48.5 angstroms (Figure VI-2a) and the prism crystal Al peak stops at 52.3 angstrom (Figure VI-2b) in both the $CaO.SiO_2$ and $Al_2O_3.SiO_2$ melts at 4000K. The diffusion distance (r) of the crystal Al is 10 angstroms at 4000K regardless the orientation of the crystal and the composition of the melt. But r is different at 3500K for each melt/crystal orientation combination. The dissolution behavior differences at the two different temperatures show that at high enough temperatures (4000K), the high mobility of the atoms can suppress the effects of melt composition and the crystal orientation, and cause a homogeneous alumina crystal dissolution at such temperature.

VI.3.2 The Dissolution in $Al_2O_3.SiO_2$ Melt

At certain temperature, the existence of the solubility limit of Al in the melt will govern how many Al crystal atoms can be dissolved. To study the effect of the presence of Al in the melt on the crystal dissolution, the concentration of the Al in the $Al_2O_3.SiO_2$ melt used in the simulation is below the Al satisfaction value in the melt according to the Al_2O_3-SiO_2 phase diagram. Beside the high temperature 4000K at which other effects were in the dissolution, the intermediate temperature 3500K was applied in the simulation also to examine other factors which may alter the dissolution behavior of the alumina crystals.

As the crystal Al diffuse into the melt, the Al originated in the melt may also diffuse back into the crystals as an exchange. As seen in figure VI-1, the atoms between the melt and crystal exchanged more frequently at 4000K (though no Al in the melt) but it decayed quickly as the temperature was lowered down to 3500K. Also as a result of the mobility decrease of the atoms at 3500K, the amount of the dissolved crystal atoms (the area of the crystal Al peaks in the melt) and the diffusion depth both decreased as shown in figure VI-2.

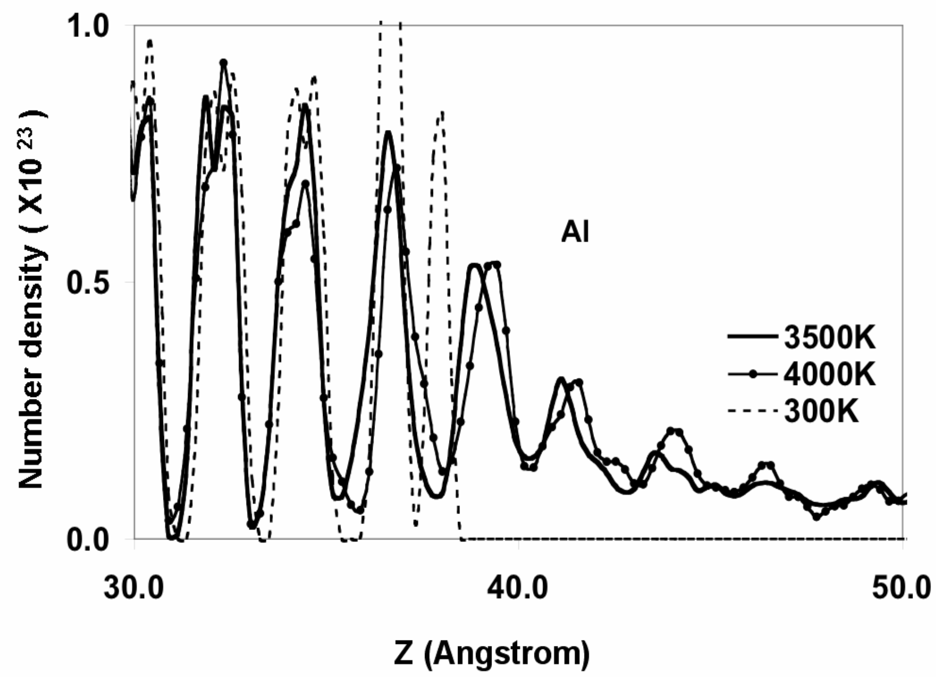

Fig. VI-3 The Al (both in the crystal and melt) density profile of the basal alumina crystal dissolution

Figure VI-3 and figure VI-4 show both the Al atoms (from the crystal and melt) presented in dissolution region for basal and prism alumina crystal respectively. For the comparison, the crystal Al peaks at 300K was shown also to illustrate the stops positions for both crystals in the density profiles. As the basal alumina crystal dissolves into the $Al_2O_3.SiO_2$ melt, it was interesting that the Al peaks in figure VI-3 looks similar at

3500K and 4500K though less dissolution at former temperature was observed. Moreover, the Al peaks' height around 39.0 angstroms are very close at both temperatures, and so does for the peak around 41.4 angstroms. The results indicated that the dissolution mechanism was almost the same in $Al_2O_3.SiO_2$ in such a temperature range. Besides, it also suggested that the diffusion of Al atoms into Al_2O_3 melt may limit the basal alumina crystal dissolution rate as the total Al distribution in the region governs the transitional diffusion due to the concentration difference.

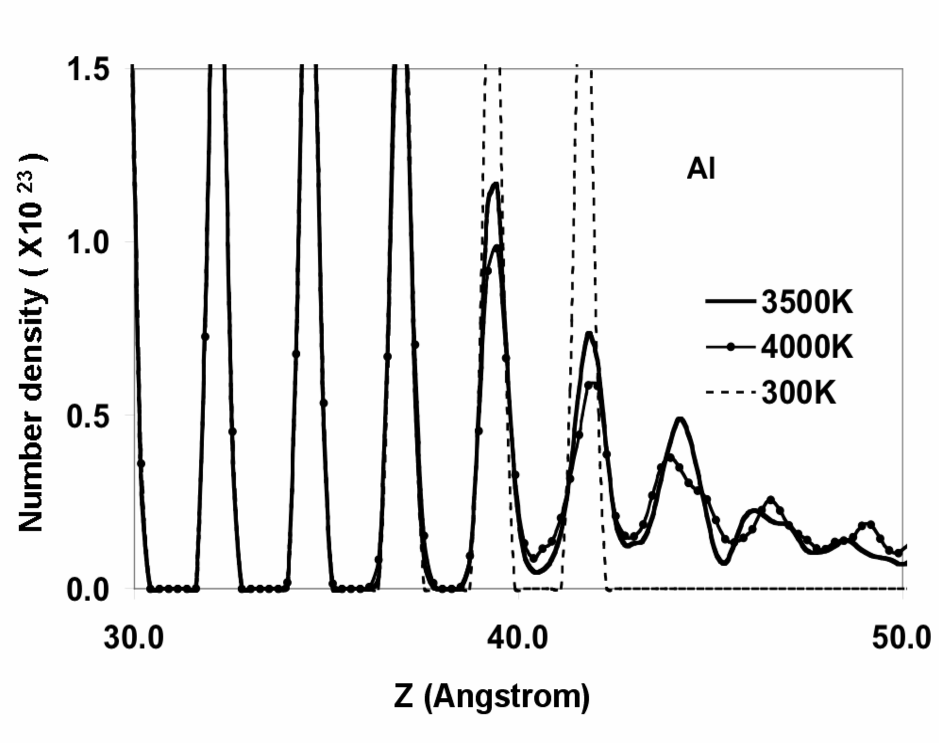

Fig. VI-4 The Al (both in the crystal and melt) density profile of the prism alumina crystal dissolution

Unlike the consistency of the basal crystal dissolution from high to low temperature, there are three exceptional Al peaks changes as the temperature lowered down from 4000K to 3500K, two peaks (at 39.4 and 41.8 angstrom) in the crystal region have the position exactly the same as the prism crystal does, together with other one Al peak in the melt at 44.2 angstroms have larger height compared to the average density value in the melt. As shown in figure VI-2, the significant decrease of the prism crystal dissolution was the reason for the two higher Al peaks in figure VI-4 at 3500K. Figure VI-5 shows the Al distribution from the $Al_2O_3.SiO_2$ melt only. The extra-high Al peak at 39.4 angstrom at 4000K compared to it at 3500K suggested that Al atoms in the melt filled back into the crystal regions due to the significant dissolving of crystal into the melt at that temperature. Though such exchange effect was very limited at 3500K, the total Al density at 39.4 angstroms is higher at 3500K. It means that the dissolution of prism crystal at 3500K is almost prohibited.

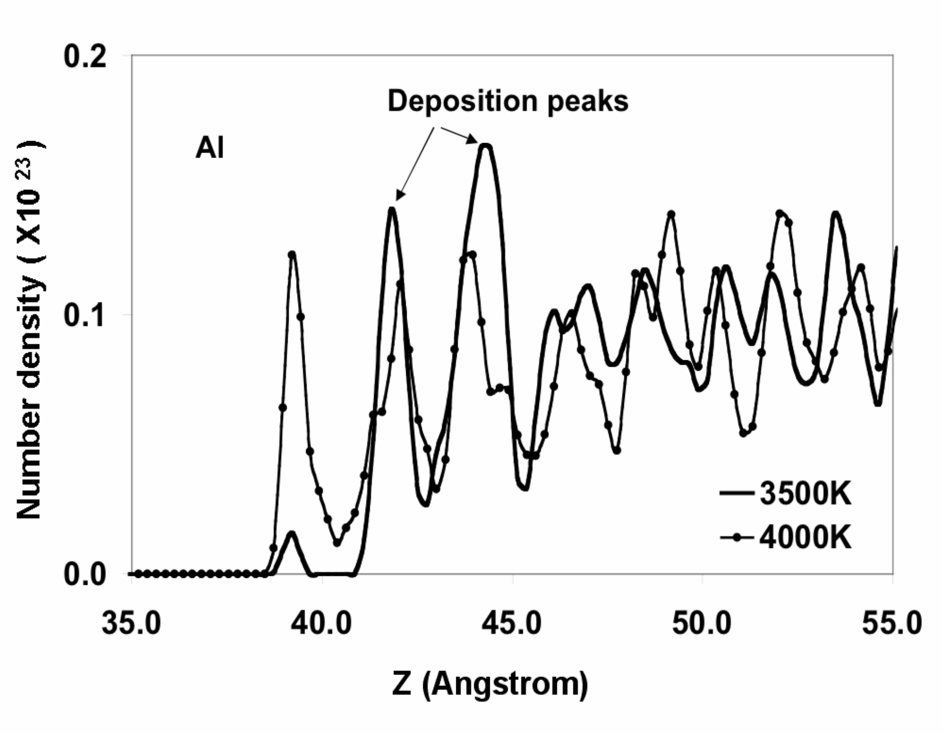

Fig. VI-5 The density profile of Al from $Al_2O_3.SiO_2$ melt in the basal alumina crystal dissolution

Moreover, there are two special high Al peaks at 41.8 and 44.2 angstrom in the figure VI-5, which are consistent to the other two peaks position in figure VI-4. The position and the over average height of the two peaks show that the Al in the melt started to deposit back to the prism alumina crystal surface and it could also contribute to the prohibition of the prism crystal dissolution in $Al_2O_3.SiO_2$ melt at 3500K.

VI.3.3 The Dissolution in $CaO.SiO_2$ Melt

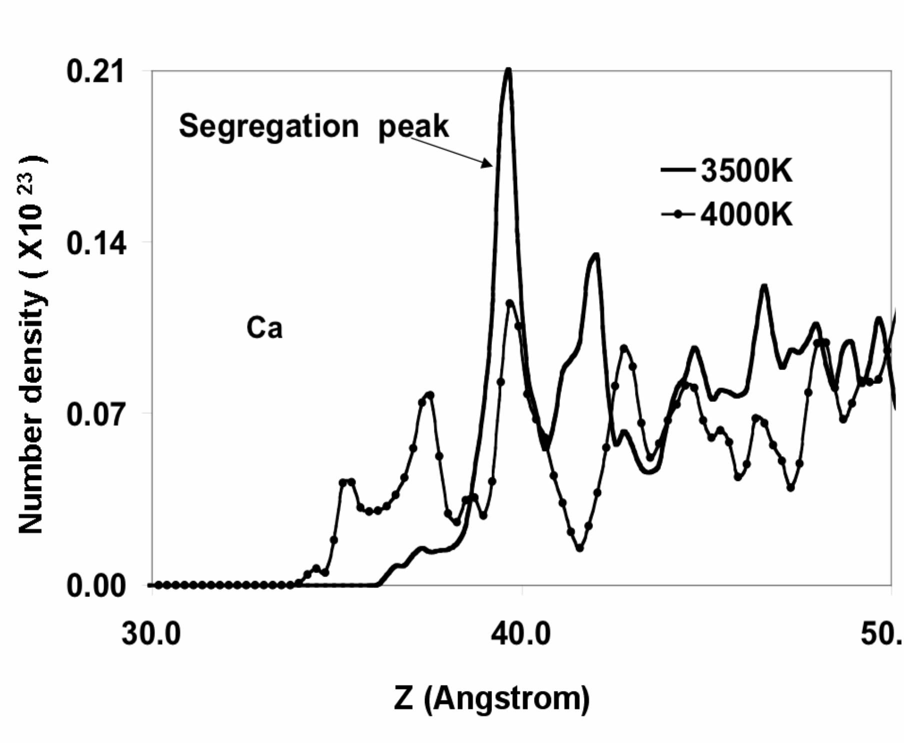

Fig. VI-6 The density profile of Ca at the interface region of the basal alumina crystal dissolution in CaO.SiO2 melt

The scenario were quite different for the alumina crystal, basal or prism, dissolved in the $CaO.SiO_2$ melt as it did in $Al_2O_3.SiO_2$. For the prism alumina crystal, the crystal Al distribution at 3500K was similar to it at 4000K except the crystal Al diffusion depth in the melt as shown in figure VI-2(b). However, the unique crystal Al distribution of basal crystal dissolving in CaO.SiO$_2$ at 3500K can be observed in figure VI-2(a): The Al peaks in the crystal regions were highest in all dissolution conditions; especially the peak around 38.5 angstroms (which is right at the crystal/melt contacting place) moves much back to the crystal and decays very fast into the melt compared to its counterparts in other dissolution conditions. The data show that basal alumina crystal has very limited dissolution in CaO.SiO$_2$ melt at 3500K but not for the prism crystal, of which no special effect was observed.

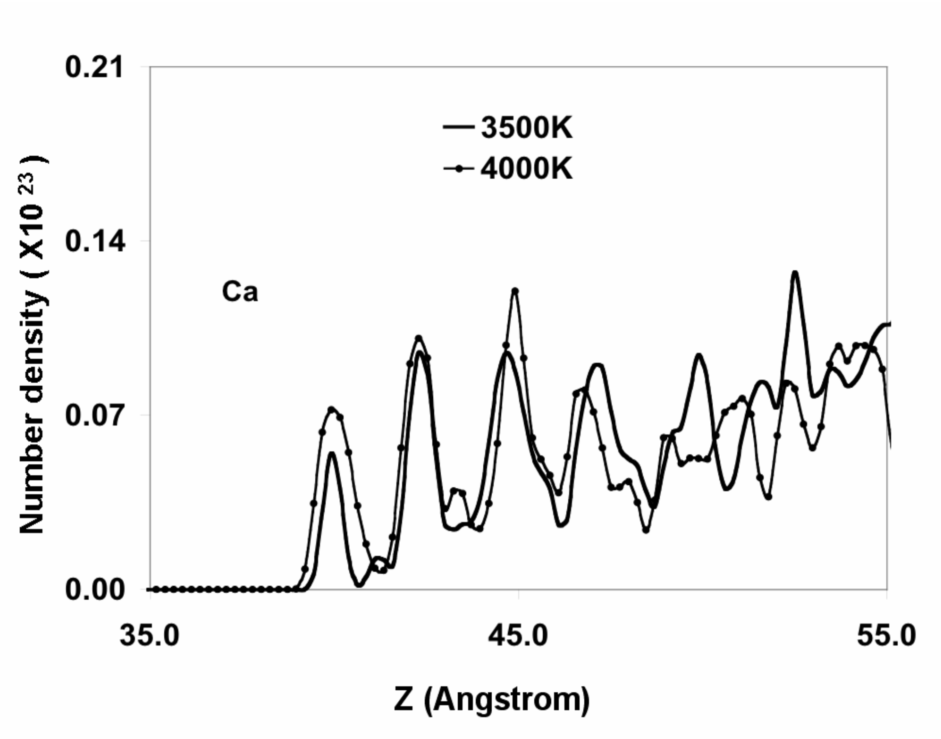

Fig. VI-7 The density profile of Ca at the interface region of the prism alumina crystal dissolution in CaO.SiO$_2$ melt

Figure VI-6 and figure VI-7 shows the Ca distribution for both basal and prism alumina crystal dissolving in CaO.SiO$_2$ melt at two temperatures respectively. The Ca distribution difference between the basal and prism crystal at the same temperature reflects the effect of the alumina crystallography on the induced ordering in melts at the interface. However, the temperature dependence of Ca behavior in the dissolution of basal and prism alumina crystal in CaO.SiO$_2$ is quite distinguished. Of the basal alumina crystal, Ca replacements of the Al in the crystal region were prevented as shown in figure VI-6, in which the Ca peak substantially retreated back into the melt as the temperature was lowered down from 4000K to 3500K. Moreover, there is an extra high segregated Ca peak at the basal crystal/melt contacting place that effectively separated the crystal and melt at 3500K. Of the prism alumina crystal, the similarity of the Ca distribution was observed at both temperatures in figure VI-7. Combined the phenomena of the Ca and Al distribution in the dissolution of basal and prism alumina crystal in CaO.SiO$_2$, it can be concluded that the dissolution of basal alumina crystal were prohibited at 3500K as a result of the segregation of the Ca at the basal crystal/melt.

VI.4 Conclusions

The dissolutions of the alumina crystal in the Al$_2$O$_3$.SiO$_2$ and CaO.SiO$_2$ were studied by MD simulations at two different temperatures, 3500K and 4000K. The alumina crystals were found to dissolve homogeneously at 4000K, regardless the melt composition and the crystal orientation used in current simulations, the diffusion depth of the crystal Al into the melt was around 10 angstroms. However, either the species presented in the melt or the crystal orientation played an important role at the 3500K, where some intermediate structures between crystal and the melt were formed to take effect on the dissolution due to the decrease of the viscosity and the atoms mobility of the melt. The dissolution of the prism alumina in $Al_2O_3.SiO_2$ and the basal alumina in $CaO.SiO_2$ melt was prohibited. The explanation of the former was the deposition of the Al in $Al_2O_3.SiO_2$ melt back to the prism crystal surface, while the segregation of the Ca to the basal crystal surface to prevent Al dissolve into the melt was the reason for the later phenomena at 3500K.

VII. Molecular Dynamic Simulations of the Fracture in the of SiO_2 IGF Between Basal Planes of Silicon Nitride Grains

VII.1 Introduction

There have been lots of interests and studies in the structure of IGFs in Si3N4 ceramics[131] [150, 151] [37]. IGFs not only play an important role in densification during ceramic sintering process, they also have a decisive effect in the fracture mechanism of Si_3N_4 ceramics. In fact, the grain boundaries of Si_3N_4 and the IGFs between them have been the key issues in the research. In the Si_3N_4 ceramics, the intergraular amorphous phase only takes a very small amount of the total ceramics. In most silicon nitride ceramics, the equivalent thickness of IGFs is from only one to several nanometers[152], the thickness is mostly dependent on the chemical composition rather than the amount of the glass phase or impurities in the Si_3N_4 ceramics. The fracture enhancement phenomena in the silicon nitride ceramics with IGFs were studied extensively. Generally speaking, the self-enhancement of Si_3N_4 ceramics can be explained by the extrinsic, microstructural contributions. These include crack deflection, crack bridging and frictional effects behind the crack tip, but is always associated with crack propagation paths in which the crack deflects along grain boundaries rather than propagating straight across grains in a transgranular manner[153].

The nature of the IGFs between Si_3N_4 grains were proved to be amorphous as shown in many experiments and simulations[99, 154-160], though with some modification from the bulk amorphous materials with same compositions because of the contacting with Si_3N_4 crystals in a very small regions. Ordered structures were found right at the contacting regions and they decay into the interior of IGFs. Experiments showed that some impurities, especially for rare earth ions, like Y, segregated to the contacting region from the IGFs. Thus for the intergranular fracture in the Si_3N_4 with IGFs, both the structures properties of the interior of IGFs and the ordered contacting interface should have important effect as voids creation and crack propagation may happen in either one or both of them.

The fractures in glassy phase were studied in micro level in bulk materials by experiments and computer simulations[161-163] [164]. The nucleation, growth and coalescence of small voids at nanometer scale were discovered in the slow glass fracture experiments under atmospheric pressure, consisting of nitrogen and water vapor below the glass transition temperature. The fracture surface was examined by atomic force microscopy (AFM). Moreover, two roughness regimes were observed on glass fracture experiments. The small regime ranging from 1 nm to 10 nm or 30 nm (depending on crack propagation velocity) was interpreted as the growth of isolated cavities at low strength while the regime with larger scale (up to 100 nm) was because of the coalescence of the voids as the stress increased[162]. Similar results were provided by Krishna on the overview of the molecular dynamic simulation data on the glass fractures[165]. The early fracture stage can be characterized by the voids formation and growth. As the strain increased, the coalescence of the voids would lead to the failure of the glass materials. Furthermore, the critical void size was determined for the voids coalescence and the rapid crack growth. However, the strain-rate applied on the glass in the simulation has a slight effect on the critical void size. In the study, the critical void size was determined to be around 4.0 angstroms as low strain-rate (0.005/ps and 0.01/ps) and around 4.5 angstrom at higher strain-rate (0.05/ps and 0.1/ps) [165].

There are great differences of the fracture in the glass and in the crystalline materials. Generally the crystalline materials have higher failure stress and lower failure strain than them in the glassy phase. One general reason for the higher stress is that the crystalline phase always has higher bond density than the glassy phase which increases the strength of the crystal materials. Thomas compared the fracture behaviors of silica glass and cristobalite by MD simulations[166]. It was observed that the high strain dependence in the glass is due to the free volume structures in the glass. The voids coalescence due to the strain flow from high density region to low density region in the glass, which leads to the failure of the glass, was very rare in the crystal because of the ordered structure and homogeneous density distribution in crystal.

The effect of the changing the chemistry of the IGFs in the fracture of Si_3N_4 ceramics are not as the same as it in bulk glassy phase. Not only the network structures on the atomic level are changed in the amorphous phase, but also the bonding conditions at the crystal surfaces due to the segregation of specific species[37]. The importance of the structures was widely accepted in the fracture studies in Si_3N_4 ceramics. The complete crack circulating around the elongated grains was observed when the part of the oxygen in the IGF was substituted by fluorine[153]. The propagation of cracks in the IGF was explained by the strong Si/Al-O bonding across the glass/grain interface with an expitaxial SiAlON layer. The bonding details were also studied and shown by the density functional theory (DFT) and molecular dynamic simulations extensively[98, 130, 167]. The structure modification and density modulation of glassy phase between Si_3N_4 grains with or without the dopant species were also observed and discussed in such simulations.

Improvement of the inspection techniques, such as scanning electron microscope (SEM) and transmission electron microscope (TEM), makes the detections of the interfacial structures at smaller size possible. For example, the segregation of rare earth atoms to the specific position at surface of prism plane was discovered by TEM recently[130]. The significant fracture mode changes in the Si_3N_4 ceramics with such rare earth atoms, such as yttrium was observed experimentally[22]. Ellen reported the improved fracture toughness in Si_3N_4 ceramics by changing the Al and Y ration in the sintering aids[168]. It was also pointed out that the interfacial bond strength was related to the bonding conditions between Al/O and O/N at the interfaces. The yttrium was found to have a negative effect on the interface bonds strength as it segregate to the prism grain surface. With high Y/Al ratio, crack could propagate in the interior of the IGFs or through the phase separation region as the interfacial debonding happened, while at low Y/Al ratio, the crack was found to grow only in the IGFs.

VII.2 Computational Procedure

The IGF system was created by put the glassy phase between two basal Si_3N_4 crystal grains in the *z* dimension, followed by the melt-quench procedures[99]. The 3-dimesional periodic boundary conditions were applied here to extend the system into infinite space. The glassy phase was chosen to be pure SiO_2 to avoid the complicated coupling effect of the impurities like Ca and Y, which will alter the fracture mechanism in Si_3N_4 ceramic. Each basal Si_3N_4 crystal grain contains 7056 atoms and two different thicknesses (around 1 nm and 2 nm) SiO_2 IGFs were created with 1764 and 3756 glass atoms respectively. To inspect the confining effect in such a small region of the IGF, the bulk SiO_2 glass fracture was also simulated for the comparison.

Constant strain rate was applied in the fracture simulation in both the IGF systems and the bulk glass. The strain rate was chosen to be 4×10^{-3}/ps as the normal value in the MD simulation of fractures[165]. To avoid the fast and extremely high local stress build up in the simulations, the simulation temperature was selected as 1000K, at which the system has a quick relaxation under strain while the IGFs and the bulk glass will not act much differently from the room temperature, in the aspect of the fracture behavior.

VII.3 Results and Discussion

VII.3.1. The Structures of the IGF

The interfaces were formed as the SiO_2 glass and the Si_3N_4 crystals contacting each other with high external pressure at high temperatures in MD simulation. Figure VII-1 is an illustration of the IGF structures for 1 nm IGF. The Si, N and O atoms are represented by different size and darkness balls in the figure. As normal the actual ion sizes were not applied in the figure in order to show the bonding condition and the structures clearly. The whole range of IGF in z dimension together with a very small amount of crystal atoms (represented by the upper and lower bound N atoms) were shown in the figure. Only the Si-O/N bonds in the IGF or between original glass atoms and crystal atoms were plotted. The details of the bonding conditions and the interface structures were discussed extensively in previous studies[160]. The ordered structure right at the interface region was the characteristic of such IGF systems. It decays into the IGF, but the interior of the IGF retains amorphous phase. In the extreme thin 1 nm IGF, some ordered modulation can even go through the whole IGF region as shown in figure VII-1, as observed in the density profiles in earlier study[160]. The similarity of the interior IGF to the bulk SiO_2 phase was seen in thicker IGF[98].

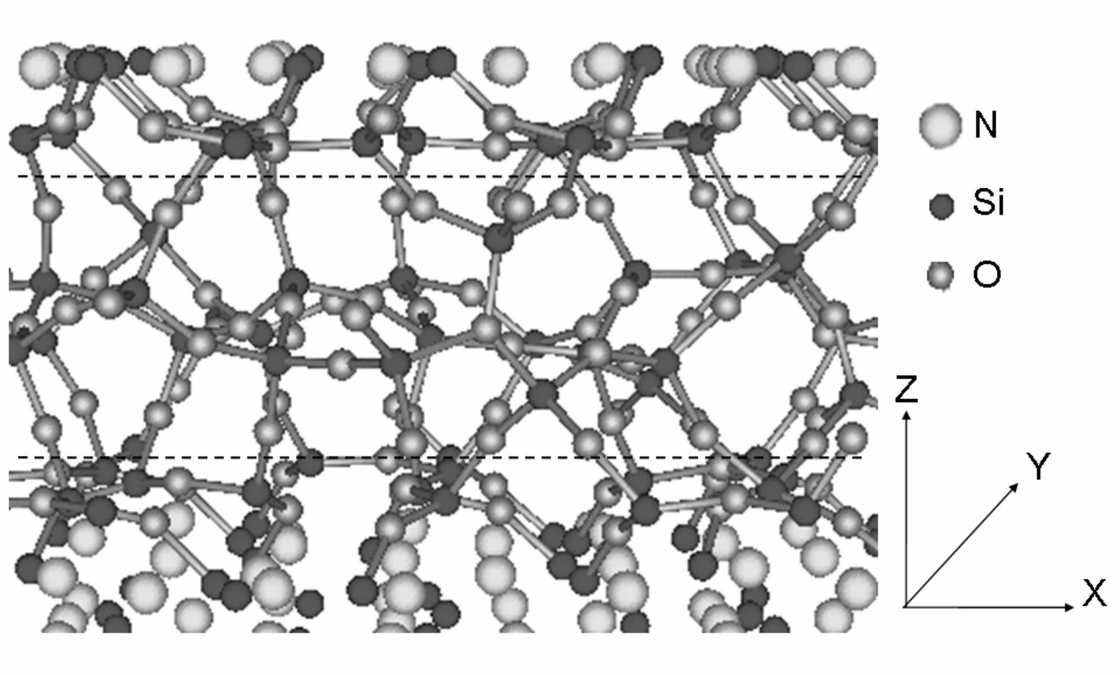

Fig VII-1. The snapshot of the 1 nm IGF between the basal Si_3N_4 grains.

VII.3.2. The Stress/Strain Relationship in the IGFs and Bulk Glass.

The tensile stress was applied on the two Si_3N_4 IGF systems and bulk glass at the *z* dimension under the same constant strain rate until the complete failure of the materials. The stress/strain relationship was show in figure VII-2 for IGF systems and in figure VII-3 for bulk glass respectively. In current study, the failure of the system was defined as the point at which the system passes through the maximum stress applied on it before the fast and catastrophic crack growth. In figure VII-3, the failure strain of the bulk glass is around 15% and the failure stress is 18GPa, which are consistent to the experimental and simulation results[165].

As observed in the figure VII-2 and figure VII-3, the failure strain in the bulk glass is much larger that it in the IGF. The reason is that the strain shown in figure VII-2 is the total strain of the IGF system which including the Si_3N_4 crystals and the IGF. Since the strength of the crystal is much higher than the IGF (amorphous phase), the stress was relaxed mostly in the IGF region, which takes most of the strain of the system. The effective failure strain in the IGF region is comparable to it in bulk glass, the value sits between 12% and 15%, which is slightly dependent on the thickness of the IGF.

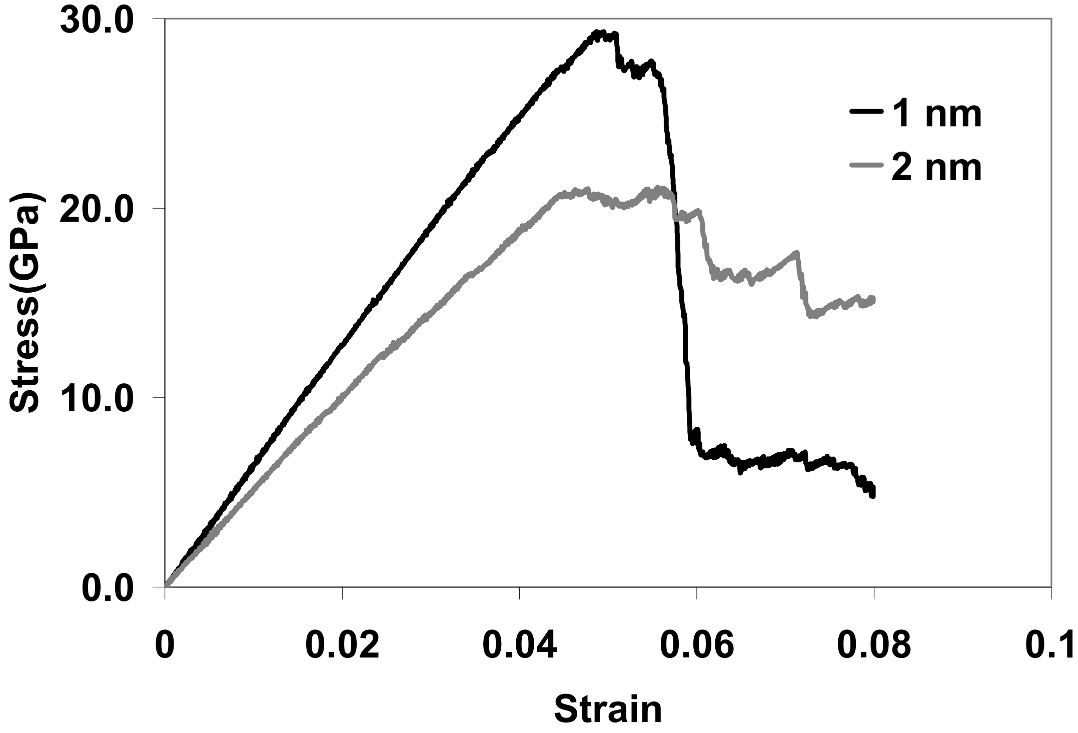

Fig VII-2. The stress/strain relationship of the simulated Si_3N_4 ceramic systems

The straight lines in the two figures at low strains represent the elastic properties of the three systems before the failure as it can be expected for such materials. The failure stress of IGF system is about 28 Gpa for 618 and 20 Gpa for 610, both are higher than it of the bulk glass. But the glass can sustain larger strain, plastic and elastic, without the happening of the catastrophic cracks as it did in the IGF system. The results suggested that the IGF may survive under larger stress but will break apart faster than the glass if the critical stress was applied.

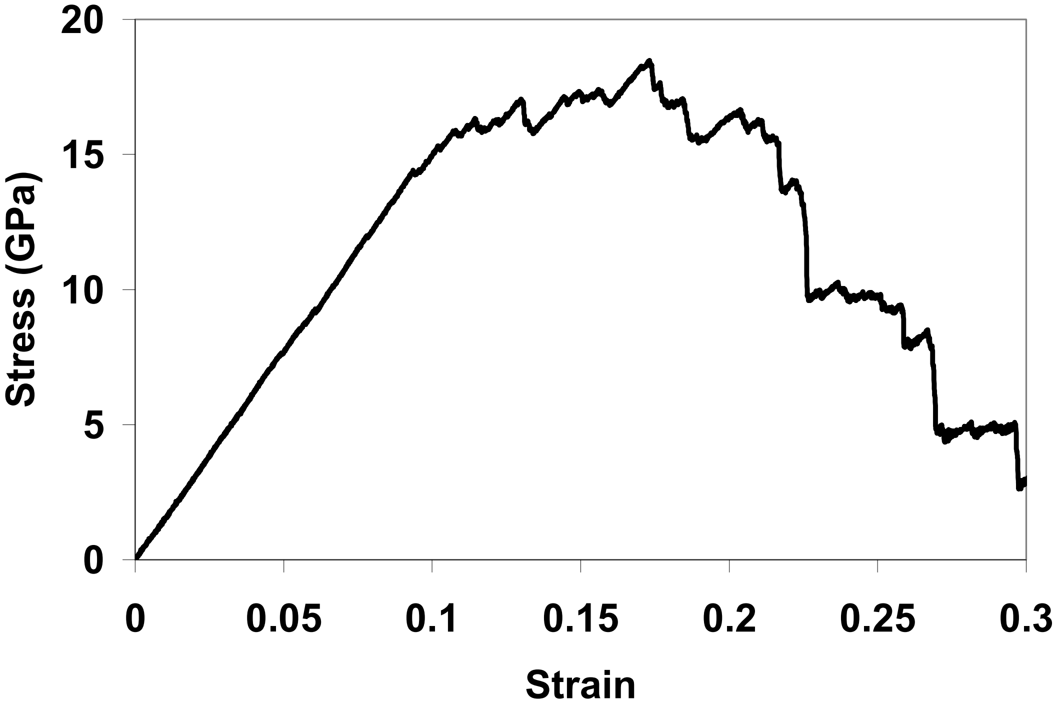

Fig VII-3. The stress-strain relationship of the bulk SiO_2 glass

VII.3.3. The Voids and Cracks in the IGFs

Figure VII-4 gives the example of how did the voids and crack form under the external tensile stress for the 1 nm IGF silicon nitride system. For the clarity, only the Si-O bonds were shown in the figure, which was represented by the short line. The red color lines mean that the Si-O bonds are over-strained but are still connected. The silicon nitride crystals, the upper and lower bounds of the IGF, are not shown in the figure. The voids and cracks are found interior of the IGF for both the 1 nm and 2 nm IGF system. It indicated that the bonds between the IGF and crystal are relative strong and they will survive through the failure of the system.

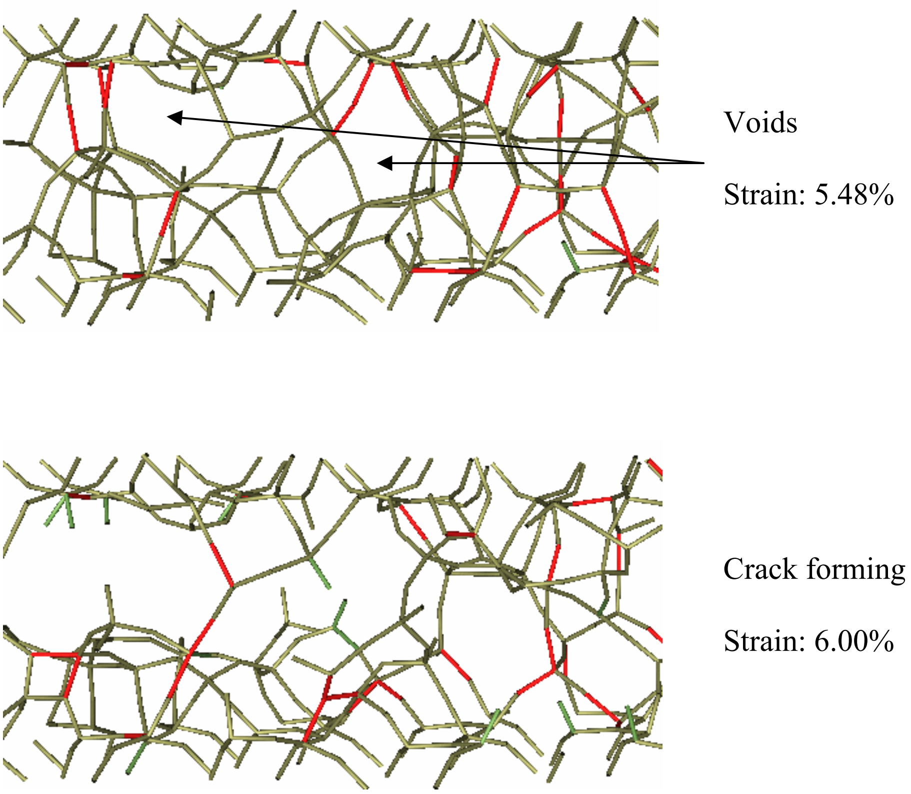

Fig. VII-4 The snapshots of the voids forming and development in the 1 nm IGF in silicon nitride system.

VII.3.4. The SiO_4-tetrahedra Rings in the IGF and Bulk Glass

In the MD simulation of silica glass, Van Brutzel found that SiO_4-tetrahedra rings were formed by the connected neighbor SiO_4 tetrahedrals[169]. The size of the rings are ranging from 3-member to 9-member (or shorted as 9-mem, so as for other rings), of which the number represents how many Si atoms are in the single ring. Under the tensile stress, the Si-O bonds are subjected to the extension strain and they will break if the strain is high enough. In addition, new Si-O bonds would form during the stress relaxation while old Si-O bonds broke. Both activities will cause the changes of the silicon tetrahedral rings. Thus the evolution of the SiO_4-tetrahedra rings distribution in the glass and IGF was important to understand the fracture behavior of the glass and IGF in the simulation.

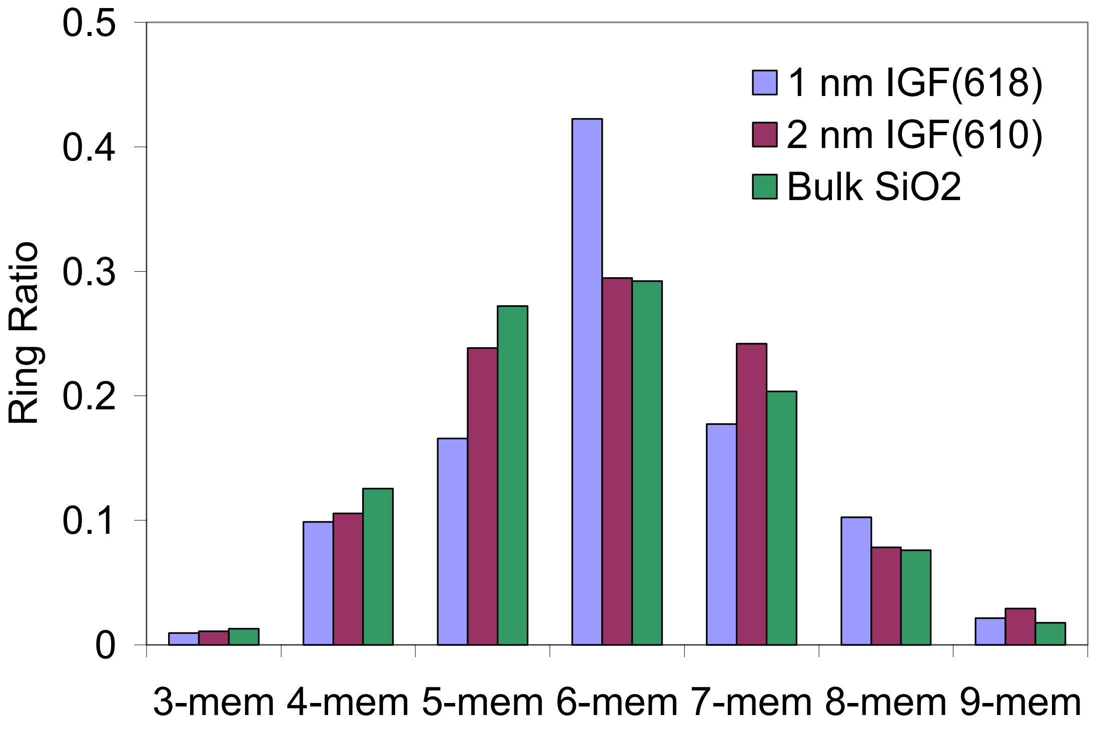

Fig. VII-5 The histogram of the ring distribution in the IGFs and bulk glass of the starting configuration before the stain.

In the calculation of the rings of the IGF, the rings formed between the first deposited Si on the Si_3N_4 surface and the crystal were excluded because they were very stable due to the crystal induced ordering during the strain, as shown in figure VII-4. The N atoms, which diffuse deep into the interior of the IGF from the Si_3N_4 crystal were treated as O, in the calculation of the silicon tetrahedral rings. It means that some bridging oxygen (BO) in the rings may be replaced by N though the amount of N in the IGF is very small. Figure VII-5 shows the rings distribution in the IGFs and bulk glass of the starting configuration before the stress was applied. It clearly shows that either the low member (3-mem and 4-mem) or high member (9-mem) rings take a very small percent in the total rings in all systems. It suggested that there are very few strained (low member rings) and void space (large member rings) regions in the systems at the beginning. The significant high percent of the 6-mem rings in 1 nm IGF, at the compensation of reduced 5- and 7-mem rings, are due to the profound ordering through the thin IGF as observed in the snapshot. However, the starting ring distribution of the 2 nm IGF and bulk glass is very similar though there are some small vibrations for some specific rings.

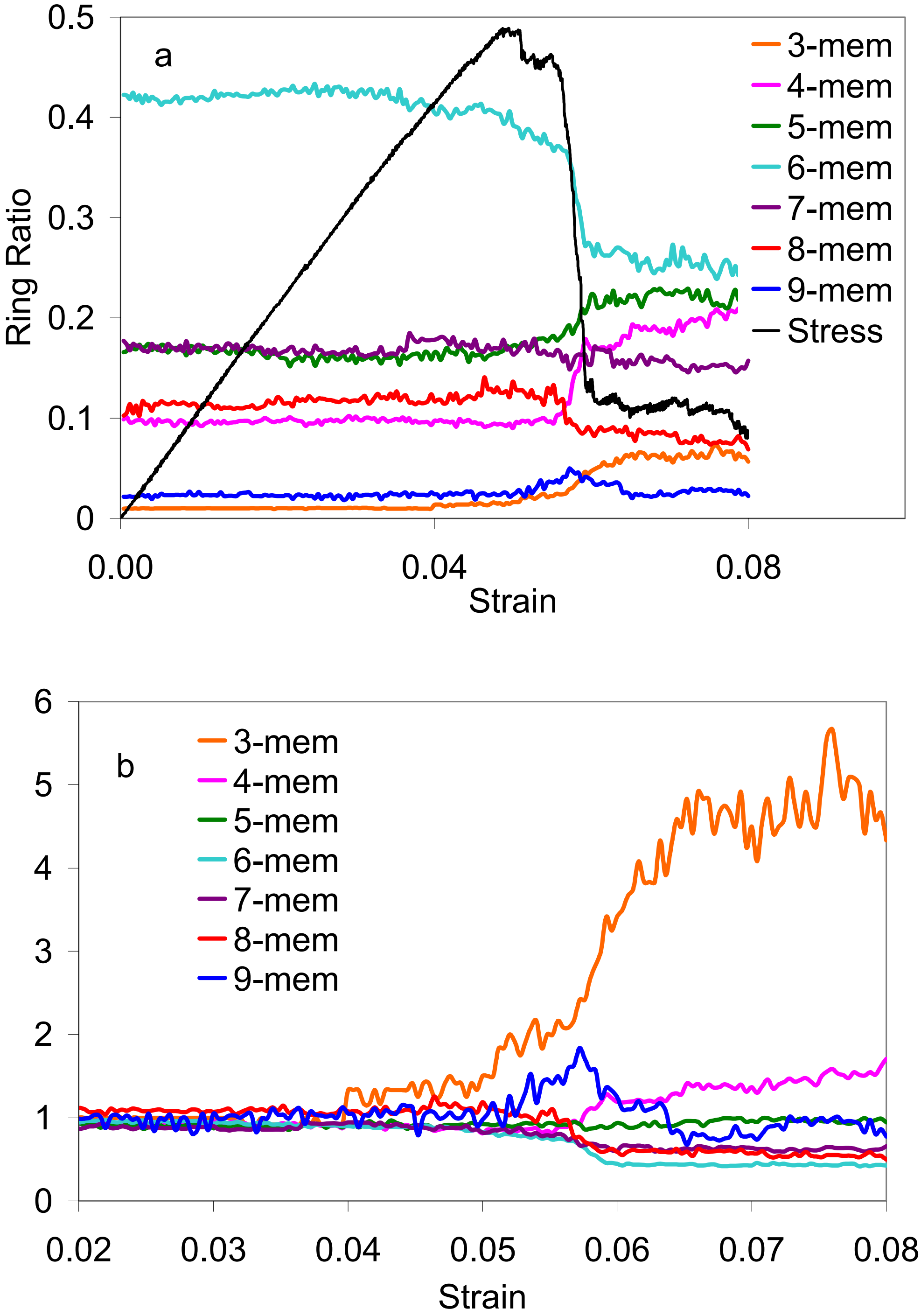

Fig. VII-6. The rings distribution evolution of the 1 nm Si_3N_4 IGF system during the strain: (a) the rings ratio, which was calculated as the ratio of the certain kind of ring to all the rings (the stress curve was scaled to plot out in the figure); (b) relative ring ratio, the vertical axis is the ratio of the current ring percentage to the original ring percentage (of the starting configuration).

Figure VII-6 shows the evolution of the SiO_4 tetrahedra rings, both the absolute (a) and the relative (b) percentage to the initial rings distribution, under the tensile stress. The stress/strain curve was rescaled in the figure to illustrate how the rings changed with the applied stress. Such rings evolution of the 2 nm IGF (a) and bulk glass (b) was also shown in the figure VII-7 for the comparison, though only the absolute ratio was presented. First of all, all the rings ratios were subjected to relatively large change around the failure point in all the system simulated, as can be expected because the substantial structure changes due to the happening of the fracture. But the details of the changes, especially for some kinds of rings which may explain the fracture behavior difference among the systems, were quite different.

The increase of the 3-mem rings ratio after failure was seen in all the three systems and how much the relative ratio increased was related to the specific system. A lot of 3-mem rings were generated in the 1 nm IGF silicon nitride system (about 5 times to the initial value), less ratio increase in the 2 nm IGF and the least in bulk glass. It was believed that the increase of 3-mem rings was related to the new surface created by the fracture in the system. The reason for the variable increased ratio of 3-men rings may exit in the system size difference. It is reasonable to make an assumption that the fracture surface was close in each system at some certain fracture stage (though the strain varies). Since the bulk volume difference (in the IGF system, only the volume of IGF itself was used to compare to the bulk glass), the portion the surface atoms in such volume is on the decreasing order as it in the 1 nm, 2 nm IGF and the bulk glass. And as a result, the ratio change of the 3-mem rings is in a decreasing order. Such a scenario may apply to other rings when the system size is involved.

Before the fracture, the voids forming, growth and the coalescence were accompanied by the old small rings breaking and the new large rings forming. As the simulations shown, the rings were relatively stable as the elastic stage. The generation and the growth of voids were really quick when the system approaches the failure point. However, such phenomena are not the same in the all systems simulated here. In this study, the large rings, 9-mem rings were created with the decrease of the 8-mem rings before the failure in the system with 1 nm IGF, as the large ratio changes of 8 & 9-mem rings shown in figure VII-6. Moreover, a substantial amount of broken 6-mem rings was also observed when the system passed through the failure point. In the 2 nm IGF and the bulk glass, the large rings, 8-mem rings and 9-mem rings before the fracture point did not have much changes in the simulation. Also, the 6-mem rings behaved quietly different compared it in the 1 nm IGF, they either were relatively stable (in 2 nm IGF) or changes slight slowly (in bulk glass).

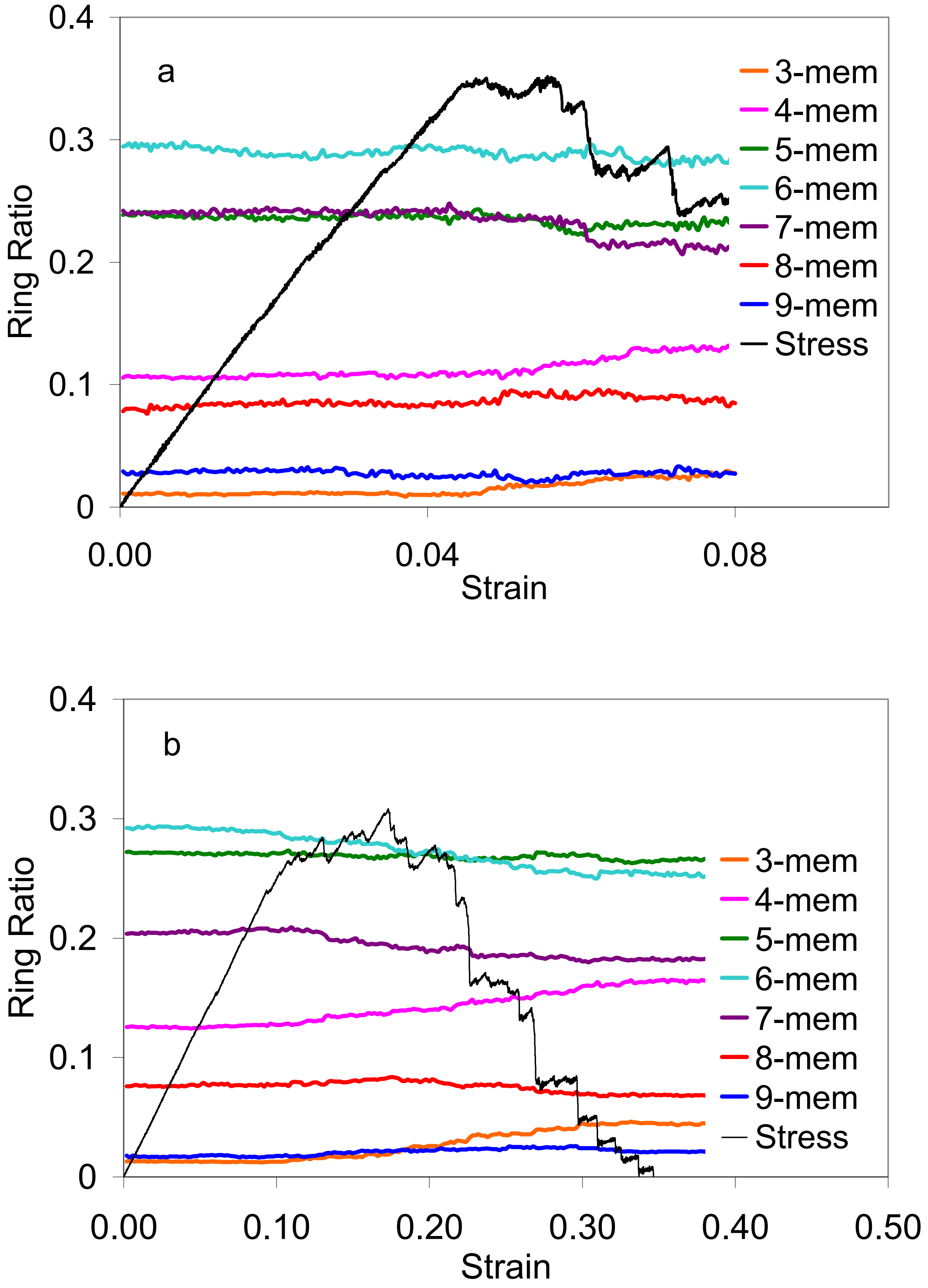

Fig. VII-7. The rings ratio evolution of the 2 nm Si_3N_4 IGF system (a) and bulk glass (b) under the stress (the corresponding stress curve was scaled to plot out in the figures respectively for each system).

The ratios change of others rings were relatively small, either decreasing or increasing around the fracture, in the 2 nm IGF and bulk glass, but not in the 1 nm IGF. The data clearly showed that the 2 nm IGF is close to the bulk glass in the fracture behavior while the 1 nm IGF is not. The large portions of the 6-mem rings and the ordering induced by the silicon nitride crystals existed in the 1 nm IGF should be the reason. There is a large shift in the relaxation mechanism from bulk glass to 1 nm IGF though the details of it need further studies. Some possible explanations are given below based on the current simulation data. In the bulk glass (and the 2 nm IGF, the large portion of the interior IGF are thought to have similar properties as the bulk glass), many kinds of silicon tetrahedral rings can participate to release the external stress because of the large volume and relative ‘soft’ network. The rings grow up with the increase of the strain and when they are close enough, they can coalescence each other to form the crack. In such a manner, not the single very large voids was needed (like the 9-mem ring) to start the fracture, at relatively low stress but a little higher strain. However, in the 1 nm IGF, the structures were confined and the ordering makes the strain not easily to be distributed equally in the system like the bulk glass. Some large rings will gain more stress and it will extends by breaking up the neighbor bonds, to form the larger one. That’s the reason why the increase of the 9-mem rings was observed. Upon the system failure, the voids will grow into microcrack with less chance to coalescent with other rings and the crack breaks through other rings directly at higher stress but less strain.

VII.4 Conclusions

The fracture behavior of the SiO2 IGF between the silicon nitride crystals was simulated under the constant strain rate, as well as of the bulk SiO_2 glass. The stress/strain relationship of each simulated system was presented. For the SiO_2 IGF between the silicon nitride crystals, the voids and cracked were found in the interior of the IGF. The failure stress is higher in the IGF than it in the bulk glass. It was also pointed out that the thickness of the IGF affects the strength of the IGF system. The ordering effect in the thin IGF was the reason for the higher failure stress. The evolution of the silicon tetrahedral rings was calculated. The large difference in the rings development under the strain among all the system simulated here was observed. Some possible explanations about the voids forming and coalescence were proposed based on the rings calculation.

VIII Summary of Conclusions

The ordering at the IGF/crystal interfaces induced by the crystals and extending ~1-1.5nm into the glassy IGFs was observed in the simulation of the structure of crystal/IGF/crystal systems using the α-alumina (0001) basal plane and $(11\bar{2}0)$ prism plane in contact with several different CAS glassy IGFs. The specific species were found to segregate preferentially to the interface regions. The presence of Ca and Si in the IGF inhibits epitaxial adsorption of Al onto the (0001) surface, thus inhibiting growth of the basal plane along the surface normal. Preferential adsorption of O and Al atoms from the IGF onto the prism plane occurs in the simulations, with more Al adsorption occurring with increased Al concentration in the IGF. The results indicated that the preferential growth is consistent with the experimental data of anisotropic growth of alumina crystals containing calcium CAS IGFs.

Ca diffusion within CAS IGFs connecting two dissimilar alumina crystal surfaces was studied using molecular dynamics simulations. Results showed that the activation energy for Ca diffusion within the bulk glasses was in the range of the experimental data and all but the highest calcia glasses showed similar activation energies. The activation energy for Ca diffusion in the interior of the IGFs was similar to, but slightly lower than, that in the bulk glasses. Diffusion near the interfaces was considerably decreased in all cases and the activation energies were increased. The diffusion constants are much lower and the activation energy much higher for Ca near the prism surface of the IGF containing the highest concentration of Al than all other regions. Ca diffusion in the interior of the IGF is similar to that in the bulk glass and should be the transport path of Ca ions during sintering.

In the study of the effects of the CAS composition on the growth of the alumina crystals, preferential growth in the $[11\bar{2}0]$ direction at all but the highest and lowest Ca/Al ratios in the IGF was proved again as seen in the experiments. These simulations indicate the mechanism by which growth on the basal plane is inhibited, affecting growth. The role of Ca in the IGF is important and affects growth.

The alumina crystals were found to dissolve homogeneously at 4000K, regardless the melt composition and the crystal orientation used in current simulations. However, either the species presented in the melt or the crystal orientation played an important role at the 3500K. The dissolution of the prism alumina in $Al_2O_3.SiO_2$ and the basal alumina in $CaO.SiO_2$ melt was prohibited. The explanation of the former was the deposition of the Al in $Al_2O_3.SiO_2$ melt back to the prism crystal surface, while the segregation of the Ca to the basal crystal surface to prevent Al dissolve into the melt was the reason for the later phenomena at 3500K.

The fracture behavior of the SiO2 IGF between the silicon nitride crystals was simulated under the constant strain rate, as well as of the bulk SiO_2 glass. For the SiO_2 IGF between the silicon nitride crystals, the voids and cracked were found in the interior of the IGF. The failure stress is higher in the IGF than it in the bulk glass. It was also pointed out that the thickness of the IGF affects the strength of the IGF system. The ordering effect in the thin IGF was the reason for the higher failure stress.

References:

1. Frenkel, D. and B. Smit, *Understanding Molecular Simulation: from Algorithms to Applications*. 2002, New York: Academic Press.
2. Rapaport, D.C., *The art of molecular dynamic simulations*. 2nd ed. 2004: Cambridge University Press. 564.
3. Allen, M.P. and D.J. Tildesley, *Computer Simulation of Liquids*. 1st Edition ed. 1987, New York: Oxford University Press. 384.
4. Alder, B.J. and T.E. Wainwright, *Phase transition for a hard sphere system.* J. Chem. Phys., 1957. **27**: p. 1208-1209.
5. Alder, B.J. and T.E. Wainwright, *Studies in Molecular Dynamics I. General method.* J. Chem. Phys., 1959. **31**: p. 459-466.
6. Rahman, A., *Correlations in the Motion of Atoms in Liquid Argon.* Phys. Rev., 1964. **136**(2A): p. 405-409.
7. Rahman, A., F.H. Stillinger, and H.L. Lemberg, *Study of a central force model for liquid water by molecular dynamics.* J. Chem. Phys., 1975. **63**: p. 5223-5230.
8. Verlet, L., *Computer "Experiments" on Classical Fluids. I. Theromdynamical Properties of Lennard-Jones Molecules.* Phys. Rev., 1967. **159**(1): p. 98-159.
9. Car, R. and M. Parrinello, *Unified Approach for Molecular Dynamics and Density-Functional Theory.* Phys. Rev. Lett., 1985. **55**: p. 2471-2474.
10. Rappe, A.K. and W.A. Goddard, *Charge Equilibration for Molecular Dynamics Simulations.* J. Phys. Chem., 1991. **95**: p. 3358-3363.
11. Robinson, G.W., et al., *Water in Biology, Chemistry, and Physics*. 1996, Singapore: World Scientific.
12. Subramaniam, A., C.T. koch, and R.M. Cannon, *Intergranular glassy films: an overview.* Mater. Sci. Eng. A, 2006. **422**: p. 3-18.
13. Clarke, D.R., *Grain boundaries in polycrystalline ceramics.* Ann. Rev. Mater. Sci., 1987. **17**: p. 57-74.
14. Dorre, E. and H. Hubner, *Alumina: Processing, Properties, and Applications*. 1984, Berlin: Springer.
15. Bennison, S.J. and M.P. Harmer, *A History of the Role of MgO in the Sintering of a-Al2O3*, in *Sintering of Advanced Ceramics*, C.A. Handwerker, J.E. Blendell, and W.A. Kaysser, Editors. 1990, American Ceramic Society: Westerville, OH. p. 13-49.
16. Bae, S.I. and S. Baik, *Determination of Critical Concentrations of Silica and/or Calcia for Abnormal Grain Growth in Alumina.* J. Am. Ceram. Soc., 1993. **76**(4): p. 1065-1067.
17. Joonchul Jung, S.B., *Abnormal Grain Growth of Alumina: CaO Effect.* J. Am. Ceram. Soc., 2003. **86**(4): p. 644-649.
18. Bruley, J., et al., *Chemistry of Grain Boundaries in Calcia Doped Silicon Nitride Studied by Spatially Resolved Electron Energy-Loss Spectroscopy.* Analy. Chemica Acta, 1994. **297**: p. 97-108.
19. Gu, H., et al., *Dopant Distribution in Grain-Boundary Films in Calcia-Doped Silicon Nitride Ceramics.* J. Am. Ceram. Soc., 1998. **81**(12): p. 3125-3135.

20. Pezzotti, G. and G.S. Painter, *Mechanisms of dopant induced changes in intergranular SiO2 viscosity in polycrystalline silicon nitride.* J. Am. Ceram. Soc., 2002. **85**(1): p. 91-96.
21. Tajima, Y., *Development of high-performance silicon nitride ceramics and their applications.* Mater. Res. Soc. Symp. proc., 1993. **287**: p. 189-96.
22. Kleebe, H.J., G. Pezzotti, and G. Ziegler, *Microstructure and fracture toughness of Si3N4 ceramics: combined roles of grain morphology and secondary phase chemistry.* J. Am. Ceram. Soc., 1999. **82**(7): p. 1857-1867.
23. Evans, A.G., *Perspective on the development of high-toughness ceramics.* J. Am. Ceram. Soc., 1990. **73**(2): p. 187-206.
24. Echeberria, J., F. Castro, and F.L. Riley, *Grain Growth in Liquid-Sintered Alumina.* Mat. Sci. Forum, 1993. **113 / 115**: p. 579-584.
25. Pezzotti, G., H.J. Kleebe, and T. Nishida, *Growth isotherms of liquid-phase sintered silicon nitride.* J. Am. Ceram. Soc., Jpn., 1997. **105**(8): p. 638-40.
26. Falk, L.K.L., *Microstructural Development During Liquid Phase Sintering of Silicon Carbide Ceramics.* J. Eur. Ceram. Soc., 1997. **17**: p. 983.
27. Kwon, O.H. and G.L. Messing, *A theoretical analysis of solution-precipitation controlled densification during liquid-phase sintering.* Acta Metall., 1991. **39**(9): p. 2059-68.
28. Bae, S.I. and S. Baik, *Abnormal Grain Growth of Alumina.* J. Am. Ceram. Soc., 1997. **80**: p. 1149-56.
29. Bae, S.I., *Sintering and Grain Growth of Ultrapure Alumina.* J. of Mat. Sci., 1993. **28**: p. 4197-4204.
30. Song, H. and R. Coble, *Morphology of Platelike Abnormal Grains in Liquid-Phase-Sintered Alumina.* J. Am. Ceram. Soc., 1990. **73**: p. 2086-90.
31. Brydson, R., S.C. Chen, and X. Pan, *Microstructure and chemistry of intergranular glassy films in liquid-phase-sintered alumina.* J. Am. Ceram. Soc., 1998. **81**(2): p. 369-79.
32. Lee, S.-H., *Effect of Anorthite Liquid on the Abnormal Grain Growth of Alumina.* J. Euro. Ceram. Soc., 2002. **22**: p. 317-321.
33. Clarke, D.R., *On the Equilibrium Thickness of Intergranular Glass Phases In Ceramic Materials.* J. Am. Ceram. Soc., 1987. **70**(1): p. 15-22.
34. Clarke, D.R. and G. Thomas, *On the Determination of Thin Intergranular Films by Electron Microscopy.* Ultramicroscopy, 1979. **4**: p. 33-44.
35. Pezzotti, G., *Mechanical spectroscopy methods for the quantitative analysis of intergranular glass viscosity in polycrystalline ceramics.* J of Non-Cryst. Sol., 2003. **321**: p. 37-51.
36. Cinibulk, M.K., H.-J. Kleebe, and M. Rühle, *Quantitative Comparison of TEM Techniques for Determining Amorphous Intergranular Film Thickness.* J. Am. Ceram. Soc., 1993. **76**(2): p. 426-32.
37. Ziegler, A., et al., *Atomic resolution transmission electron microscopy of the intergranular structure of a Y2O3-containing silicon nitride ceramic.* J. Am. Ceram. Soc., 2003. **86**(10): p. 1777-1785.
38. Handwerker, C.A., et al., *Dihedral Angles in Magnesia and Alumina: Distributions from Surface Thermal Grooves.* J. Am. Ceram. Soc., 1990. **73**(5): p. 1371-77.

39. Brydson, R., et al., *Influence of CaO-SiO2 ratio on the chemistry of intergranular films in liquid-phase sintered alumina and implications for rate of erosive wear.* J. Mater. Res., 2001. **16**: p. 652-665.
40. Baik, S. and C.L. White, *Anisotropic Calcium Segregation to the Surface of Al2O3.* J. Am. Ceram. Soc., 1987. **70**(9): p. 682-88.
41. Kaplan, W.D., H. Mullejans, and M. Ruhle, *Ca Segregation to Basal Surface in a-Alumina.* J. Am. Ceram. Soc., 1995. **78**(10): p. 2841-2844.
42. Cho, S.-J., et al., *Chemical inhomogeneity in commercial alumina powder and its effect on abnormal grain growth during sintering.* J. Euro. Ceram. Soc., 2003. **23**: p. 2281-2288.
43. Cook, R.F., *Calcium Segregation to Grain Boundaries in Alumina.* J. Am. Ceram. Soc., 1988. **71**(1): p. 50-58.
44. Hansen, S.C. and D.S. Phillips, *Grain boundary microstructure in a liquid-phase sintered alumina (a-Al2O3).* Phil. Mag. A., 1983. **47**: p. 209-34.
45. Kim, D.-Y., et al., *Stability and Surface Energies of Wetted Grain Boundaries in Aluminum Oxide.* J. Am. Ceram. Soc., 1994. **77**: p. 444-453.
46. Kim, S.S., J.H. Moon, and S. Baik, *Interfacial Segregation of Mg and Ca and Its Effect on Microstructural Evolution During Sintering of Alumina.* Sol. St. Phenom., 1992. **25** / **26**: p. 269.
47. Song, S. and R.L. Coble, *Origin and Growth Kinetics of Platelike Abnormal Grains in Liquid-Phase-Sintered Alumina.* J. Am. Ceram. Soc., 1990. **73**(7): p. 2077-85.
48. Swiatnicki, W., S. Lartigue-Korinek, and J.Y. Laval, *Grain boundary structure and intergranular segregation in Al2O3.* Acta Met., 1995. **43**: p. 795-805.
49. Bae, S.I. and S. Baik, *Sintering and grain growth of ultrapure alumina.* J. Mat. Sci., 1993. **28**: p. 4197-4204.
50. Bae, S.I., *Critical Concentration of MgO for the Prevention of Abnormal Grain Growth in Alumina.* J. Am. Ceram. Soc., 1994. **77**: p. 2499-2504.
51. Zhao, H., X.Z. Hu, and M.B. Bush, *Grain growth phenomena on the interface region of a-alumina bilayer composites.* J. Am. Ceram. Soc., 2001. **84**(8): p. 1865-72.
52. Altay, A. and M.A. Gulgun, *Microstructural evolution of calcium doped alpha-alumina.* J. Am. Ceram. Soc., 2003. **86**(4): p. 623-629.
53. Bae, S.I. and S. Baik, *Critical Concentration of MgO for the Prevention of Abnormal Grain Growth in Alumina.* J. Am. Ceram. Soc., 1994. **77**(10): p. 2499-2504.
54. Powell-Dogan, C.A. and A.H. Heuer, *Microstructure of 96% Alumina Ceramics: I, Characterization of the As-Sintered Materials.* J. Am. Ceram. Soc., 1990. **73**(12): p. 3670-76.
55. Powell-Dogan, C.A. and A.H. Heuer, *Microstructure of 96% Alumina Ceramics: III, Crystallization of High-Calcia Boundary Glasses.* J. Am. Ceram. Soc., 1990. **73**(12): p. 3684-91.
56. Ching, W.Y., *The electronic structure and bonding of all crystalline phases in the SiO2-Y2O3-Si3N4 phase equilibrium diagram.* J. Amer. Ceram. Soc., 2004. **87**(11): p. 1995-2012.

57. Rulis, P., et al., *Electronic structure and bonding of intergranular glassy films (IGF) in polycrystalline Si3N4: Ab-initio studies and classical MD simulations.* Phys.Rev. B, 2005. **71**: p. 235317-1-10.
58. Panagiotopoulos, A.Z., *Monte Carlo methods for phase equilibria of fluids.* J. Phys.: Condens. Matter., 2000. **12**(3): p. R25-R52.
59. Feuston, B.P. and S.H. Garofalini, *Empirical Three-Body Potential for Vitreous Silica.* J. Chem. Phys., 1988. **89**(9): p. 5818-5824.
60. Garofalini, S.H., *Molecular Dynamics Computer Simulations of Silica Surface Structure and Adsorption of Water Molecules.* J. Non-Cryst. Solids, 1990. **120**: p. 1-12.
61. Melman, H. and S.H. Garofalini, *Microstructural Evaluation of Simulated Sodium Silicate Glasses.* J. Non-Cryst. Solids, 1991. **134**: p. 107-115.
62. Zirl, D.M. and S.H. Garofalini, *Structure of Sodium-Aluminosilicate Glasses.* J. Am. Ceram. Soc., 1990. **73**(10): p. 2848-2856.
63. Garofalini, S.H. and G. Martin, *Molecular Simulations of the Polymerization of Silicic Acid Molecules and Network Formation.* J. Phys. Chem., 1994. **98**: p. 1311-1316.
64. Martin, G. and S.H. Garofalini, *Sol-Gel Polymerization: Analysis of Molecular Mechanisms and the Effect of Hydrogen.* J. Non-Cryst. Sol., 1994. **171**: p. 68-79.
65. Baik, S. and J.H. Moon, *Effects of Magnesium Oxide on Grain-Boundary Segregation of Calcium During Sintering of Alumina.* J. Am. Ceram. Soc., 1991. **74**(4): p. 819.
66. McCune, R.C. and R.C. Ku, *Calcium Segregation to MgO and a-alumina surfaces*, in *Advanced Ceramics*, W.C. Kingery, Editor. 1984, American Ceramic Society: Columbus, OH.
67. Shaw, T.M. and P.R. Duncombe, *Forces Between Aluminium Oxide Grains in a Silicate Melt and Their Effect on Grain Boundary Wetting.* J. Am. Ceram. Soc., 1991. **74**(10): p. 2495-2505.
68. Blonski, S. and S.H. Garofalini, *Molecular Dynamics Simulations of α-alumina and γ-alumina Surfaces.* Surf. Sci., 1993. **295**: p. 263-274.
69. Blonski, S. and S.H. Garofalini, *Molecular Dynamics Study of Silica-Alumina Interfaces.* J. Phys. Chem., 1996. **100**: p. 2201-2205.
70. Blonski, S. and S.H. Garofalini, *Atomistic Structure of Calcium Silicate Intergranular Films in Alumina Studied by Molecular Dynamics Simulations.* J. Am. Ceram. Soc., 1997. **80**(8): p. 1997-2004.
71. Mackrodt, W.C., et al., *The Morphology of α-Al_2O_3 and α-Fe_2O_3: The Importance of Surface Relaxation.* J. Crystal Growth, 1987. **80**: p. 441-446.
72. Batirev, I.G., A. Alavi, and M.W. Finnis, *Ab initio calculations of the Al2O3 (0001) surface.* Faraday Discuss., 2000. **114**: p. 33-43.
73. Litton, D.A. and S.H. Garofalini, *Atomistic Structure of Sodium and Calcium Silicate Intergranular Films in Alumina by Molecular Dynamics.* J. Mat. Res., 1999. **14**: p. 1418-1429.
74. Powell-Dogan, C.A. and A.H. Heuer, *Microstructure of 96% Alumina Ceramics: II, Crystallization of High-Magnesia Boundary Glasses.* J. Am. Ceram. Soc., 1990. **73**(12): p. 3677-83.

75. Litton, D.A. and S.H. Garofalini, *Molecular Dynamics Simulations of Calcium Alumino-Silicate Intergranular Films on (0001) Alumina Faces.* J. Am. Ceram. Soc., 2000. **83**(9): p. 2273-2281.
76. Abramo, M.C., C. Caccamo, and G. Pizzimenti, *Structural properties and medium-range order in calcium-metasilicate (CaSiO3) glass: a molecular dynamics study.* J. Chem. Phys., 1992. **96**: p. 9083-9091.
77. Cormack, A.N. and Y. Cao, *Molecular dynamics simulation of silicate glasses*, in *Modelling of minerals and silicated minerals*, B. Silvi and P. D'Arco, Editors. 1997, Kluwer Academic: Dordrecht, The Netherlands. p. 227-271.
78. Delaye, J.-M., V. Louis-Achille, and D. Ghaleb, *Modeling oxide glass with Born-Mayer-Huggins potentials: Effect of composition on structural changes.* J. Non-Cryst. Sol., 1997. **210**: p. 232-242.
79. Stein, D.J. and F.J. Spera, *Molecular dynamics simulations fo liquids and glasses in the system NaAlSiO4-SiO2: Physical properties and transport mechanisms.* Am. Mineral., 1996. **81**: p. 284-302.
80. Kubicki, J.D. and A.C. Lasaga, *Molecular Dynamics Simulations of* SiO_2 *Melt and Glass: Ionic and Covalent Models.* Am. Mineral., 1988. **73**: p. 941-955.
81. Cormack, A.N., *The effect of glass structure on transport properties from atomistic computer simulations.* J. Non-Cryst. Solids, 1998. **232-234**(11): p. 188-197.
82. Cormier, L., et al., *Competition for charge compensation in borosilicate glasses: wide-angle x-ray scattering and molecular dynamics calculations.* Phys. Rev. B, 2000. **61**: p. 14495-14499.
83. Stebbins, J.F. and Z. Xu, *NMR evidence for excess non-bridging oxygen in an aluminosilicate glass.* Nature, 1997. **390**: p. 60-62.
84. Handwerker, C.A., P.A. Morris, and R.L. Coble, *Effects of Chemical Inhomogeneities on Grain Growth and Microstructure in Al2O3.* J. Am. Ceram. Soc., 1989. **72**: p. 130-36.
85. Simpson, Y.K. and C.B. Carter, *Faceting Behavior of Alumina in the Presence of a Glass.* J. Am. Ceram. Soc., 1990. **73**: p. 2391-98.
86. Tanaka, I., et al., *High temperature fracture mechanism of low-Ca doped silicon nitride.* J. Am. Ceram. Soc., 1995. **78**(3): p. 673-679.
87. Becher, P. *The Role of Intergranular Phases and Films in Ceramic Systems*. in *Workshop on Interfaces in Silicon-Based Ceramics*. 1998. Berkeley, CA.
88. MacLaren, I., et al., *Abnormal grain growth in alumina: synergistic effects of yttria and silica.* J. Am. Ceram. Soc., 2003. **86**(4): p. 650-659.
89. Kaysser, W.A. and M. Sprissler, *Effect of a Lquid Phase on the Morphology of Grain Growth in Alumina.* J. Am. Ceram. Soc., 1987. **70**(5): p. 339-343.
90. Baer, D., et al., *Comparison of AES and XPS Analysis of Thin Passive Films.* J. Vac. Sci. Technol., 1982. **20**(4): p. 957-961.
91. Miyahara, M. and K.E. Gubbins, *Freexing/melting phenomena for Lennard-Jones methane in slit pores: A Monte Carlo study.* J. Chem. Phys., 1997. **106**: p. 2865-2880.
92. Gelb, L. and K.E. Gubbins, *Correlation functions of adsorbed fluids in porous glass: a computer simulation study.* Molec. Phys., 1999. **96**: p. 1795-1804.

93. Shevade, A.V., S. Jiang, and K.E. Gubbins, *Adsorption of water-methanol mixtures in carbon and aluminosilicate pores: a molecular dynamics study.* Molec. Phys., 1999. **97**: p. 1139-1148.
94. Radhakrishnan, R. and K.E. Gubbins, *Effect of the fluid-wall interaction on freezing of confined fluids:Toward the development of a global phase diagram.* J. Chem. Phys., 2000. **112**: p. 11048-11057.
95. Zhang, L., et al., *Nonequilibrium molecular dynamics simulations of confined fluids in contact with the bulk.* J. Chem. Phys., 2001. **114**: p. 6869-6877.
96. Zhang, S. and S.H. Garofalini, *Molecular dynamic computer simulations of the interface structure of calcium-alumino-silicate intergranular films between combined basal and prism planes of a-Al2O3.* J. Am. Ceram. Soc., 2005. **88**(1): p. 202-209.
97. Garofalini, S.H. and W. Luo, *Molecular dynamics simulations of calcium silicate intergranular films between silicon nitride crystals.* J. Am. Ceram. Soc., 2003. **86**(10): p. 1741-1752.
98. Su, X. and S.H. Garofalini, *Atomistic structure of calcium silicate intergranular films between prism and basal planes in silicon nitride: a molecular dynamics study.* J. Mat. Res., 2004. **19**: p. 752-758.
99. Su, X. and S.H. Garofalini, *Role of Nitrogen on the Atomistic Structure of the Intergranular Film in Silicon Nitride: A Molecular Dynamics Study.* J. Mat. Res., 2004. **19**: p. 3671-3678.
100. Bryce, J.G., F.J. Spera, and D.J. Stein, *Pressure dependence of self-diffusion in the NaAlO2-SiO2 system: Compositional effects and mechanisms.* Am. Mineral., 1999. **84**: p. 345-356.
101. Doremus, R., *Electrical Conductivity and Electrolysis of Alkali Ions in Silica Glass.* Phys. & Chem. of Glasses, 1969. **10**(1): p. 28-33.
102. Frischat, G., *Self-Diffusion Processes in Oxide Glasses.* Nuclear Techn., 1980. **51**: p. 130-135.
103. Liang, Y., et al., *Diffusion in silicate melt: I. Self diffusion in CaO-Al2O3-SiO2 at 1500oC and 1GPa.* Geochim. Cosmochim. Acta, 1996. **60**(22): p. 4353-4367.
104. Freer, R., *Diffusion in Silicate Minerals and Glasses: A Data Digest and Guide to the Literature.* Contrib Mineral Petrol, 1981. **76**: p. 440-454.
105. Frischat, G.H., *Ionic Diffusion in Oxide Glasses*, ed. Y. Adda, et al. Vol. 3/4. 1975, Germany: Trans Tech. Publ.
106. Frischat, G., *Anomalous Diffusion Behaviour of Sodium in SiO2 Glass. Part 2. Results and Interpretation.* Phys. & Chem. of Glasses, 1984. **25**(4): p. 110-111.
107. Greaves, G.N., et al., *A Structural Basis for Ionic Diffusion in Oxide Glasses.* Phil. Mag. A, 1991. **64**(5): p. 1059-1072.
108. Sen, S. and T. Mukerji, *A molecular dynamics simulation study of ionic diffusion and NMR spin–lattice relaxation in Li2Si4O9 glass.* J. Non-Cryst. Sol., 2001. **293-295**: p. 268-278.
109. Meyer, A., H. Schober, and D.B. Dingwell, *Structure, structural relaxationand ion diffusion in sodium disilicate melts.* Europhys. Lett., 2002. **59**: p. 708-713.
110. Soules, T.F., *Molecular dynamic calculations of glass structure and diffusion in glass.* J. Non Cryst. Sol., 1982. **49**: p. 29-52.

111. Li, W. and S.H. Garofalini, *Molecular dynamics simulation of lithium diffusion in Li2O-Al2O3-SiO2 glasses.* Sol St Ionics, 2004. **166**: p. 365-373.

112. Dufty, J.W., K.C. Mo, and K.E. Gubbins, *Models for self-diffusion in square well fluid.* J. Chem. Phys., 1991. **94**(4): p. 3132-3140.

113. Liu, Y.C., Q. Wang, and L.H. Lu, *Density inhomogeneity and diffusion behavior of fluids in micropores by molecular-dynamics simulation.* J. Chem. Phys., 2004. **120**(22): p. 10728-10735.

114. Bitsanis, I., et al., *Molecular dynamics of flow in micropores.* J. Chem. Phys., 1987. **87**(3): p. 1733-1750.

115. Somers, S.A. and H.T. Davis, *Microscopic dynamics of fluids confined between smooth and atomatically structured solid surfaces.* J. Chem. Phys., 1992. **96**(7): p. 5389-5407.

116. Su, Z., J.H. Cushman, and J.E. Curry, *Computer simulation of anisotropic diffusion in monolayer films in mica slit pores.* J. Chem. Phys., 2003. **118**(3): p. 1417-1422.

117. Garofalini, S.H. and S. Zhang, *Molecular dynamics computer simulations of calcium-alumino-silicate intergranular films between the basal and prism planes of a-Al2O3*, in *Mat. Res. Soc. Symp. Proc.* 2003, Matls. Res. Soc., Pittsburgh, PA.: Boston. p. 191-200.

118. Liang, Y., F.M. Richter, and E.B. Watson, *Diffusion in silicate melts: II. Multicomponet diffusion in CaO-Al2O3-SiO2 at 1500oC and 1 GPa.* Geochim. Cosmochim. Acta, 1996. **60**(24): p. 5021-5035.

119. Morgen, N.A. and F.J. Spera, *Glass transition, structure relaxation, and theories of viscosity: A molecular dynamics study of amorphous CaAl2Si2O8.* Geochim. Cosmochim. Acta, 2001. **65**(21): p. 4019-4041.

120. Roselieb, K. and A. Jambon, *Tracer diffusion of Mg, Ca, Sr, and Ba in Na-aluminosilicate melts.* Geochim. Cosmochim. Acta, 2002. **66**(1): p. 109-123.

121. Liang, Y. and A.M. Davis, *Energetics of multicomponent diffusion in molten CaO-Al2O3-SiO2.* Geochim. Cosmochim. Acta, 2002. **66**(4): p. 635-646.

122. Mazurin, O.V., M.V. Streltsina, and T.P. Shvaiko-Shvaikovskaya, *Handbook of Glass Data Part A; Silica glass and binary silicate glasses*. 1983, New York: Elsevier.

123. Powell-Dogan, C.A., A.H. Heur, and H.M. O'Bryan, *Devitrification of the Grain Boundary Glassy Phase in a High-Alumina Ceramic Substrate.* J. Am. Ceram. Soc., 1994. **77**: p. 2593.

124. Bae, J.-S. and S.-I. Pyun, *Electrochemical lithium intercalation reaction of anodic vanadium oxide film.* J. Alloys and Compnds, 1995. **217**: p. 52-58.

125. Jung, J. and S. Baik, *Abnormal grain growth of alumina: CaO effect.* J. Am. Ceram. Soc., 2003. **86**(4): p. 644-649.

126. Baik, S., *Segregation of Magnesium and Calcium to the (1010) Prismatic Surface of Magnesium-Implanted Sapphire.* J. Am. Ceram. Soc., 1988. **71**(5): p. 358-362.

127. Park, C.W., *Singular Grain Boundaries in Alumina and Their Roughening Transition.* J. Am. Ceram. Soc., 2003. **86**(4): p. 603-611.

128. Kolar, D., *Discontinuous Grain Growth in Multiphase Ceramics*, in *Sintering of Advanced Ceramics*, J.E.B. C. A. Handwerker, Editor. 1990, Am. Ceram. Soc.: Westerville, OH.

129. Kwon, O.-S., et al., *Microstructural evolution during sintering of TiO2-SiO2-doped alumina: mechanism of anisotropic abnormal grain growth.* Acta Mater., 2002. **50**: p. 4865-4872.
130. Shibata, N., et al., *Observation of rare-earth segregation in silicon nitride ceramics at subnanometer dimensions.* Nature, 2004. **428**: p. 730-733.
131. Doblinger, M., et al., *Structural and compositional comparison of Si3N4 ceramics with different fracture modes.* Acta Mater., in press.
132. Clarke, D., *On the Equilibrium Thickness of Intergranular Glass Phases in Ceramic Materials.* J. Am. Ceram. Soc., 1987. **70**(1): p. 15-22.
133. Huang, C. and A.N. Cormack, *The structure of sodium silicate glass.* J. Chem. Phys., 1990. **93**: p. 8180-8186.
134. Huang, C. and A.N. Cormack, *Structural Differences and Phase Separation in Alkali SIlicate Glasses.* J. Chem. Phys., 1991. **95**(5): p. 3634-3642.
135. Kaysser, W.A., et al., *Effect of a Liquid Phase on the Morphology of Grain Growth in Alumina.* J. Am. Ceram. Soc., 1987. **70**: p. 339-343.
136. Kim, M.J. and D.Y. Yoon, *Effect of magnesium oxide addition on surface roughening of alumina grain in anorthite liquid.* J. Am. Ceram. Soc., 2003. **86**(4): p. 630-633.
137. Xue, L.A. and I.W. Chen, *Low-Temperature Sintering of Alumina with Liquid-Forming Additives.* J. Am. Ceram. Soc., 1991. **74**: p. 2011.
138. Samaddar, B.N., W.D. Kingery, and A.R. Cooper, *Dissolution in Ceramic Systems: I, Molecular Diffusion, Natural Convection, and Forced Convection Studies of Sapphire Dissolution in Calcium Aluminum Silicate.* J. Am. Ceram. Soc., 1964. **47**(1): p. 37-43.
139. Samaddar, B.N., K.W. D., and A.R. Cooper, *Dissolution in Ceramic Systems: II, Dissolution of Alumina, Mullite, Anorthite, and Silica in a Calcium-Aluminum-Silicate Slag.* J. Am. Ceram. Soc., 1964. **47**(5): p. 249-254.
140. Oishi, Y., A.R. Cooper, and W.D. Kingery, *Dissolution in Ceramic Systems: III, Boundary Layer Concentration Gradients.* J. Am. Ceram. Soc., 1965. **48**(2): p. 88-95.
141. Bates, J.L., *Heterogeneous Dissolution of Refractory Oxide in Molten Calcium-Aluminum-Silicates.* J. Am. Ceram. Soc., 1987. **70**(3): p. C55-C57.
142. Sandhage, K.H. and G.J. Yurek, *Direct and indirect Dissolution of Sapphire in Calcia-Magnesia-Alumina-Silica Melts: Dissolution Kinetics.* J. Am. Ceram. Soc., 1990. **73**(12): p. 3633-40.
143. Sandhage, K.H. and G.J. Yurek, *Direct and indirect Dissolution of Sapphire in Calcia-Magnesia-Alumina-Silica Melts: Electron Microprobe Analysis of the Dissolution Process.* J. Am. Ceram. Soc., 1990. **73**(12): p. 3643-49.
144. Zhang, S., et al., *Alumina Dissolution into Silicate Slag.* J. Am. Ceram. Soc., 2000. **83**(4): p. 897-903.
145. Monaghan, B.J. and L. Chen, *Dissolution behavior of alumina micro-particles in CaO-SiO2-Al2O3 liquid oxide.* J of Non-Cryst. Sol., 2004. **347**: p. 254-261.
146. Choi, J.Y., H.G. Lee, and J.S. kim, *Dissolution Rate of Al2O3 into Molten CaO-SiO2-Al2O3 Slags.* ISIJ International, 2002. **42**(8): p. 852-860.
147. Guha, P., *Reaction Chemistry in Dissolution of Polycrystalline Alumina in Lime-Alumina-Silica Slag.* Trans. Br. Ceram. Soc., 1997. **96**(6): p. 231-36.

148. Zhang, S. and S.H. Garofalini, *Molecular dynamics simulations of the effect of the composition of calcium alumino-silicate intergranular films on alumina grain growth.* J. Phys. Chem. B, 2006. **110**: p. 2233-2240.
149. Batirev, I.G., et al., *First principles calculations of the ideal cleavage energy of bulk niobium(111)/alpha-alumina(0001)interfaces.* Phys. Rev. Lett., 1999. **82**: p. 1510-1513.
150. Becher, P.F., et al., *Influence of additives on anisotropic grain growth in silicon nitride ceramics.* Matl. Sci. Eng. A, 2006. **422**: p. 85-91.
151. Becher, P.F., et al., *The importance of amorphous intergranular films in self-reinforced Si3N4 ceramics.* Acta Mater., 2000. **48**: p. 4493-4499.
152. Kleebe, H.-J., M.J. Hoffmann, and M. Rühle, *Influence of Second Phase Chemistry on Grain Boundary Film Thickness in Silicon Nitride.* Z. Metallkd, 1992. **83**(8): p. 610-17.
153. Becher, P.F., et al., *The importance of amorphous intergranular films in self-reinforced beta-Si3N4 ceramics.* J. Am. Ceram. Soc., 2000. **48**: p. 4493-4499.
154. Cinibulk, M.K., H.-K. Kleebe, and M. Rühle, *Amorphous intergranular films in silicon nitride ceramics quenched from high temperatures.* J. Am. Ceram. Soc., 1993. **76**(11): p. 2801-2808.
155. Kleebe, H.-J., *Structure and Chemistry of Interfaces in Si3N4 Ceramics Studied by Transmission Electron Microscopy.* J. Ceram. Soc. Japan, 1997. **105**: p. 453-475.
156. Pezzotti, G., et al., *Chemistry and inherent viscosity of glasses segregated at grain boundaries of silicon nitride and silicon carbide ceramics.* Journal of Non-Crystalline Solids, 2000. **271**: p. 79-87.
157. Wang, C.M. and M. Mitomo, *Atomic structural environment of Y in the residual glass phase of silicon nitride and alpha-sialon.* Acta Mater., 2002. **50**: p. 3151-3158.
158. Umesaki, N., N. Hirosaki, and K. Hirao, *Structural characterization of amorphous silicon nitride by molecular dynamics simulation.* J. of Non-Cryst. Sol., 1992. **150**: p. 120-125.
159. Su, X. and S.H. Garofalini, *Effect of interphase mixing on interface structure at the calcium silicate intergranular film/silicon nitride crystal interfaces.* J. Chem. Phys., 2005. **97**: p. 113526-1-7.
160. Garofalini, S.H., *Molecular dynamics simulations of the atomistic structure of the intergranular film between silicon nitride grains: effect of composition, thickness, and surface vacancies.* Mater. Sci. Eng. A, 2006. **422**: p. 115-122.
161. Bouchaud, E., *Scalling properties of cracks.* J. Phys. Cond. Matter, 1997. **9**(21): p. 4319-4344.
162. Daguier, P., et al., *Pinning and Depinning of Crack fronts in Heterogeneous Materials.* Phy. Rev. Lett., 1997. **78**(6): p. 1062-1065.
163. Célarié, F., S. Prades, and D. Bonamy, *Glass Breaks like Metal, but at the Nanometer Scale.* Phy. Rev. Lett., 2003. **90**(7): p. 075504-1-4.
164. Campbell, T., R.K. Kalia, and A. Nakano, *Structural Correlations and Mechanical Behavior in Nanophase Silica Glasses.* Phy. Rev. Lett., 1999. **82**(16): p. 4018-4021.

165. Muralidharan, K., et al., *Molecular dynamics studies of brittle fracture in vitreous silica: Review and recent progress.* J. Non-Cryst. Sol., 2005. **351**: p. 1532-1542.
166. Swiler, T.P., J.H. Simmons, and A.C. Wright, *Molecular dynamics study of brittle fracture in silica glass and cristobalite.* J. Non-Cryst. Sol., 1995. **182**: p. 68-77.
167. Painter, G.S., et al., *First-principles study of rare-earth effects on grain growth and microstructure in beta-Si3N4 ceramics.* Phys. Rev. B, 2004. **70**: p. 144108-1-4.
168. Sun, E.Y., P.F. Becher, and K.P. Plucknett, *Microstructural design of silicon nitride with improved fracture toughness: II, Effects of yittria and alumina additives.* J. Am. Ceram. Soc., 1998. **81**(11): p. 2831-2840.
169. Rountree, C.L., et al., *Atomistic aspects of crack propagation in brittle materials: multimillion atom molecular dynamics simulations.* Ann. Rev. Mater. Res., 2002. **32**(377-400).

Vita

Shenghong Zhang

1992-1997	BS in Chemistry, Peking University (China)
1997-2000	MS in Material Engineering, Chinese Academy of Science
2001-2007	Ph.D in Material Science & Engineering, Rutgers, the state University of New Jersey
1998	"Computer Controlled Data System for XPS and SIMS", *Computers and Applied Chemistry* (Chinese)
2001	"Reliability of PbSnAg Solder Layer of Power Modules under Thermal Cycling in Electronic Package", *the Chinese Journal of Nonferrous Metals* (Chinese)
2005	"Molecular Dynamics Computer Simulations of the Interface Structure of Calcium Alumino-Silicate Intergranular Films between Combined Basal and Prism Planes of α-Al_2O_3", *Journal of America Ceramic Society, Vol 88*
2005	"Molecular dynamic Simulation of Calcium Diffusion in the Calcium Alumino-Silicate Intergranular Film Between Different Alumina Grains", *Journal of America Ceramic Society,Vol 88*
2006	"Molecular Dynamics Simulations of the Effect of the Composition of Calcium Alumino-Silicate Intergranular Films on Alumina Grain Growth", *Phys. Chem. B, Vol 110*
2006	"The effect of the composition of the intergranular film in alumina on preferential adsorption and growth", *J. Matls. Sci*. 41